CHARACTERIZATION OF SPARKJET FOR FLIGHT CONTROL

BY KELLIE ANDERSON

A dissertation proposal submitted to the

Graduate School—New Brunswick

Rutgers, The State University of New Jersey

in partial fulfillment of the requirements

for the degree of

Doctor of Philosophy

Graduate Program in Mechanical and Aerospace Engineering

Written under the direction of

Doyle D. Knight

and approved by

_____

_____

_____

_____

New Brunswick, New Jersey

MAY, 2012

ABSTRACT OF THE DISSERTATION

Characterization of SparkJet for Flight Control

by KELLIE ANDERSON

Dissertation Director: Doyle D. Knight

The need for flow control devices with rapid actuation has surged with recent interest in hypersonic flight. Plasma actuation offers actuation times orders of magnitude smaller than conventional mechanical and electro-mechanical actuators. A novel concept using a plasma to generate a high speed jet is evaluated. The jet (known as a "SparkJet") is generated by depositing energy in a cavity by a pulsed electrical discharge. The high pressure gas exits through an orifice in the cavity, creating a jet. This research is a study of the effectiveness of using this jet for flow control. This research focuses on characterizing the forces generated by the SparkJet. The jet is first characterized exiting to a quiescent environment. An analytical solution is obtained which relates the dimensionless impulse to the dimensionless energy deposition. The analytical result is verified with a computational solution. The two agree very well and both results indicate that the dimensionless impulse is insensitive to the dimensionless geometry parameters. A Monte-Carlo analysis verifies the insensitivity of the dimensionless impulse to dimensionless geometry parameters. The SparkJet issuing into a quiescent environment is compared to experimental results. The jet exiting into a turbulent Mach 3 cross flow boundary layer is then evaluated computationally. The dimensionless impulse is much higher than the quiescent flow case and dimensionless discharge times are also greater.

Nomenclature

A	=	area of cavity exit, linearized system of equations
a	=	speed of sound
B	=	magnetic field
c_p	=	specific heat at constant pressure
c_v	=	specific heat at constant volume
D	=	cavity diameter
d	=	cavity orifice diameter
e	=	total energy per unit mass
E	=	electric field
F	=	instantaneous force
h_t	=	height of cylindrical throat
I	=	impulse
J	=	current
k	=	thermal conductivity, turbulent kinetic energy per unit mass
L	=	height of cylindrical part of cavity
M	=	moment of inertia, Mach number
m	=	mass in cavity
$\dot{m}$	=	mass flow rate
p	=	pressure
Q	=	energy deposited to cavity
q	=	energy per unit mass
R	=	distance from body c.g. to plasma jet, gas constant of air
Re	=	Reynolds number
T	=	temperature
$\mathcal{T}$	=	torque
t	=	time
u	=	velocity

V = cavity volume

V_e = electrode volume

v = velocity

w = Cole's wake function

α = $\sqrt{\kappa\xi}$

β = angle of converging part of cavity

γ = specific heat ratio

δ = dimensionless cavity exit diameter

ϵ = dimensionless energy deposition, specific dissipation

ζ = characteristic time for actuating control surface

η = $\frac{p_t}{p_{to}}$, effectiveness parameter

Θ = $\frac{t_f}{10}\frac{a_{to}A}{V}$

θ = momentum thickness of boundary layer

ϑ = dimensionless impulse

ι = time constant in lumped capacitance method

κ = $\left(\frac{p_{to}}{p_\infty}\right)^{(\gamma-1)/\gamma}$

$\varkappa$ = electrical conductivity

λ = dimensionless height of cylindrical part of cavity

μ = $\sqrt{\left(\frac{p_t}{p_\infty}\right)^{(\gamma-1)/\gamma} - 1}$, dynamic viscosity

μ_T = eddy viscosity

ν = viscosity

ξ = $\left(\frac{p_t}{p_{to}}\right)^{(\gamma-1)/\gamma}$

ϖ = $\frac{V\zeta}{a_\infty A_e}$

Π = wake strength

ρ = density

σ = $\left(\frac{\gamma+1}{2}\right)^{\gamma/(\gamma-1)}$

τ = dimensionless time

ϕ = angle of rotation of body, solution vector for mass and momentum equations

φ = realization

ω = specific dissipation rate

subscripts

app = applied field

∞ = environmental properties

f = property at end of discharge

t = total property

th = property at cavity exit

i = internal property

ind = induced field

o = initial property

superscripts

$\rightarrow$ = vector

$\sim$ = Favre averaged property, Rhoe averaged property

$-$ = ensemble average

$''$ = deviation from Favre average

$+$ = turbulent nondimensionalization

Acknowledgements

I would like to express sincere thanks to my advisor, Professor Doyle Knight for his guidance, expertise and patience. Without his encouragement, graduate school would not be nearly as rewarding.

I would like to thank my thesis committe members, Professor Prosenjit Bagchi, Professor Jerry Shan and Professor Gregory Elliott for their helpful comments and suggestions. I would like to express gratitude to our collaborators at the University of Illinois, Professor Greg Elliott, Professor Craig Dutton, Professor Nick Glumac, Todd Reedy and Brad Sanders. I am also grateful to Steve Wilkinson for his discussions, suggestions and enthusiasm for this research.

I am indebted to Kevin Anderson, my husband; I am bewildered by his patience and unyielding support. And many thanks to my mother, father and brother, who have always supported my endeavors. And thanks to my colleagues and friends at Rutgers for their thoughtful discussions and support, Ye Cheng, Mona Golbabaei, Sara Salahi, and Aurora Costache.

This research is supported by AFOSR Grant FA9550-10-1-0111, managed by Dr. John Schmisseur.

Dedication

To Kevin Anderson, my favorite human.

Table of Contents

List of Tables

List of Figures

Chapter 1

Introduction

1.1 Motivation

One of the major challenges of hypersonic flight is aerodynamic control. Current hypersonic test vehicles (e.g., X-34[8], X-43A[9]) fly with movable aerodynamic surfaces. For DARPA's hypersonic test vehicle, the HTV-2, this led to flight control problems. The first flight test was successful for nine minutes, when the vehicle experienced "higher than predicted yaw" [10]. The yaw lead into a roll which the on-board control system was unable to correct and the vehicle consequentially self-destructed. The second flight test had a corrected center of mass and added augmentation to the vehicle flaps; nevertheless, the vehicle was lost after twelve minutes due to flight control problems [11].

Another major challenge of hypersonic flight is rapid maneuvering, a critical aerodynamic capability of transonic military aircraft for decades. In the cobra maneuver [12], for example, the aircraft pitches up to an angle of attack over 70^o, rapidly decelerating the aircraft, then pitches back down to a desired angle of attack. The maneuver is indispensable for air combat, as it is a means of rapid deceleration and also creates an opportunity for a pursued aircraft to become the pursuer. The move is not only difficult because it demands control of the aircraft at high angles of attack (post-stall) but it also must be executed in approximately 5 seconds [13]. To put this in a dimensionless perspective, if a 15 m vehicle is initially flying at 120 m/s, the entire maneuver is accomplished in the equivalent of 40 vehicle lengths of flight. For the remainder of this article, "rapid maneuvering" refers to this type of motion, i.e., large changes in angle of attack, roll or yaw in tens of vehicle lengths flight progression. Rapid maneuvering would be very useful in hypersonic flight for tactical missions.

One of the greatest obstacles to rapid maneuverability in hypersonic flight is control

response. Currently, hypersonic vehicles use conventional movable aerodynamic surfaces for flight control (X-34[8], X-43A[9]). A maneuver requiring a large change in vehicle orientation, such as the cobra, requires full control surface deflection. The fastest electromechanical actuators offer full deflection times on the order of tenths of a second [14]. For a 4 m vehicle flying at Mach 20 at an altitude of 30 km (such as the HTV-2), the full actuation time of the control surface occurs in 150 vehicle lengths. Though aerodynamic surfaces are effective at trimming the vehicle for long term flight, rapid maneuvers can not be achieved with such conventional actuation methods. Faster control methods are necessary for rapid maneuverability of hypersonic vehicles at cruise speeds.

1.2 Literature Review

Flow control by means of energy deposition has, over the past hundred years, gained popularity because it requires no moving parts and has actuation times on the order of nanoseconds. Flow control can be broken into the following groups

1. Dielectric Barrier Discharge (DBD)
2. Laser/Microwave Discharge
3. Magneto-Hydrodynamics (MHD)/Magneto-Gasdynamics (MGD)

The following summaries provide brief introductions to the different areas of energy deposition flow control research. More comprehensive reviews can be found in Schutze, Knight, Bletzinger [15, 16, 17, 18, 19].

1.2.1 Dielectric Barrier Discharge

Dielectric barrier discharge refers to a configuration in which two plates (planar or cylindrical) with an applied voltage difference are separated by a dielectric (non-conducting) interface. The most common configuration in flow control has an asymmetric arrangement of plates. The electrical field lines between the two plates are then curved [20], which creates a paraelectric effect. When enough energy is applied, a breakdown of the gas occurs. Breakdown at atmospheric pressure takes the form of 'micro-discharges.' That is, small

filaments of conductive gas (plasma) are generated between the exposed electrode and the dielectric. The filaments generate a charge near the surface, which inhibits the electric field. Without the electric field, the filaments disappear. The entire process occurs on the order of nanoseconds, which leaves very little time for Joule heating of the gas (heat transfered to the gas via the current through the conductive gas). Thus, the process is primarily athermal. The gas is driven by the movement of ions in the curved electric field, which transfer momentum to the neutral gas. The flow velocity is low, on the order of 1-10 m/s. Applications for DBDs are vast, industrial applications range from ozone generation, surface treatment (increase in surface energy), silent discharge CO_2 lasers to the plasma display panels seen in plasma televisions [21]. Flow include delay of separation in high lift airfoils [22, 23, 24] noise reduction [25], vortex shedding control [26]. The DBD is well-characterized, experiments have quantified the forces produced (on the order of mN/m) [27, 28], and flow velocities induced (on the order of 10 m/s) [27]. Additionally, much progress in computational efforts has been achieved, as reviewed in Jayaraman and Shyy [20]. Dielectric barrier discharge shows great promise for low-speed flow control.

1.2.2 Laser and Microwave Energy Deposition

Laser and microwave energy deposition is attractive because energy deposition can be created at a distance from the energy generating source. Though the physical mechanisms by which breakdown is achieved is fundamentally different between microwave and laser induced plasma generation, drag reduction is primarily a thermal phenomenon [29]. Thus the mechanism by which the plasma is created has a secondary effect on the plasma-shock interaction. Laser and microwave energy deposition are effective at reducing supersonic wave drag, particularly on blunt bodied vehicles [30, 31, 32, 33, 34]. Additionally, much research has been performed in an effort to user laser and microwave energy deposition to reduce peak heating in shock-shock interactions [35]. Extensive reviews in this area have been published by Knight *et al* [16], Fomin *et al* [36], Knight *et al* [17], Bletzinger *et al* [18] and Knight [19].

1.2.3 Magneto Hydrodynamics

Magneto hydrodynamics is the coupling of an electrically conductive fluid with an applied magnetic field. Magneto gasdynamics is the same coupling but the fluid is specifically an ionized gas (such as air colliding with a hypersonic vehicle). The magnetic field is applied perpendicular to the velocity vector of the fluid flow. An electric field is induced by their cross product following the equation [37]

$$\vec{E}_{ind} = \vec{v} \times \vec{B}_{app} \tag{1.1}$$

where $\vec{E}_{ind}$ is the induced electric field, $\vec{v}$ is the velocity vector of the fluid, and $\vec{B}_{app}$ is the applied magnetic field vector. From Ohm's law, there is a current generated in the fluid, $\vec{J}_{ind}$ proportional to the electrical conductivity, $\varkappa$

$$\vec{J}_{ind} = \varkappa \vec{E}_{ind} \tag{1.2}$$

The cross product of the current and the magnetic field yields a ponderomotive force, $\vec{F}_{ind}$ perpendicular to both

$$\vec{F} = \vec{J}_{ind} \times \vec{B}_{app} \tag{1.3}$$

An externally applied electric field can be employed, $\vec{E}_{app}$, which adds an extra term to the conductivity and the force equations, respectively

$$\vec{J} = \varkappa \left(\vec{E}_{app} + \vec{E}_{ind} \right) = \varkappa \left(\vec{E}_{app} + \vec{v} \times \vec{B}_{app} \right) \tag{1.4}$$

$$\vec{F} = \vec{J} \times \vec{B}_{app} = \varkappa \left(\vec{E}_{app} + \vec{v} \times \vec{B}_{app} \right) \times \vec{B}_{app} \tag{1.5}$$

If the electric field is applied in the opposite direction of $\vec{v} \times \vec{B}_{app}$ then the force from the electric field acts to accelerate the fluid flow. The ponderomotive force from the magnetic field acts in the opposite direction, however, thus in order to achieve an acceleration, the force from the electric field must be greater than the force from the magnetic field. Much success has been achieved with MHD systems, particularly in combination with DBDs in the areas of shock wave/turbulent boundary layer interaction [38] and improved performance of scramjet engines [39], [40], [41]. Surveys as Knight [17], Shang [42] and Cambel [37] provide comprehensive reviews on MHD systems.

1.2.4 SparkJet

The SparkJet is a recent concept that creates a surface jet using energy deposition. The SparkJet device consists of a small recessed surface cavity (volume $\sim$0.1 cm^3) with a converging nozzle. The cavity is pulsed with energy deposition which can be in the form of a spark discharge, microwave discharge or a focused laser. The energy deposited rapidly heats and pressurizes the air in the cavity, creating a plasma. The hot, high pressure air evacuates the cavity through the converging nozzle forming a jet. The SparkJet uses no additional fuel, requires no tubing and has no moving parts. SparkJets have been studied by several groups under different names: "SparkJet" ^{TM}by John's Hopkins Applied Physics Lab [1], "Pulsed-Plasma Jet Actuator" by University of Texas at Austin [5] and the "Plasma Synthetic Jet" by ONERA [43]. Work by these groups is detailed in the following paragraphs.

Johns Hopkins Applied Physics Lab

The development and characterization of the SparkJet has been ongoing at John's Hopkins Applied Physics Lab (APL) since 2003. Characterization has taken the form of experimental, computational and analytical work. Additionally, APL holds a patent for the SparkJet [44]. The initial design for the SparkJet was a cylindrical cavity encased in ceramic with a cathode at the bottom, a nearby grid and an anode at the top of the cavity [1]. The configuration is shown in Figure 1.1. The device was operated by first applying an electrical potential between anode and cathode that is less than the breakdown potential. Shortly thereafter a voltage drop is initiated between the anode and grid which ionizes the surrounding air. The free electrons generated initiate breakdown between the anode and cathode. The streamer formed between the anode and the cathode rapidly heats and pressurizes the air in the cavity; this was termed the energy deposition stage. The hot, high pressure air in the cavity then evacuates to the ambient air in the discharge stage. Finally, surrounding air is pulled back into the cavity in the refill stage. The three stages are depicted graphically in Figure 1.2.

Investigation of this device included a one-dimensional analytical model, a computational

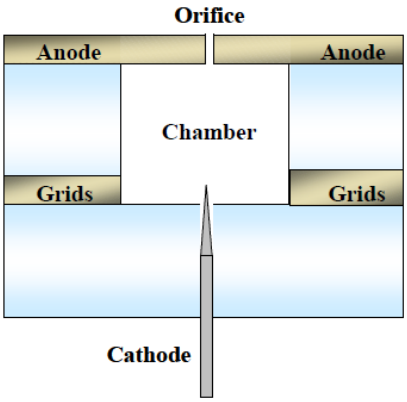

Figure 1.1: First Generation SparkJet Device at APL [1]

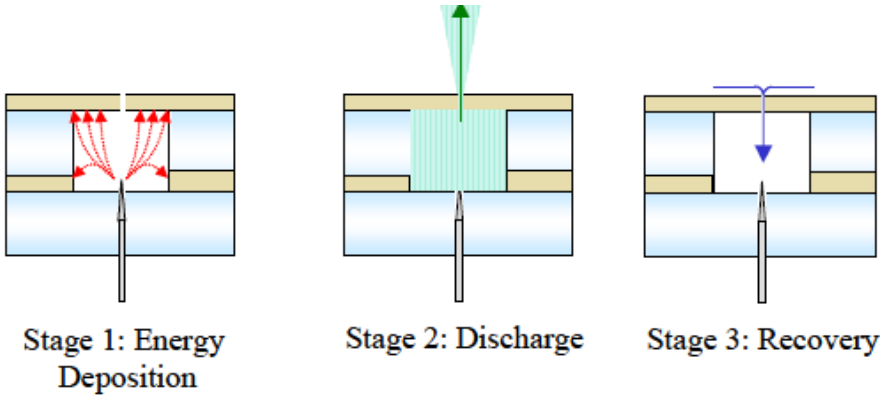

Figure 1.2: Three Stages of SparkJet Operation [1]

simulation and an experiment [1]. The analytical model estimated the time that the discharge was sonic, the necessary amount of energy lost through the cavity wall to refill the cavity and an estimation of temperature and pressure in the cavity after the energy deposition stage. The computations predicted supersonic flows out of the cavity. An experiment documented the SparkJet flow with Schlieren images.

In 2004, APL investigated a second generation SparkJet [2]. The second generation device removed the grid electrode, had a blunt tipped cathode (for increased life) and employed interchangeable components which allowed for different cavity volume and discharge diameter. A schematic of the improved device is shown in Figure 1.3. A parametric study was performed which evaluated the effect of changing the cavity volume and orifice diameter. Figure 1.4(a) shows that the exit velocity decreases with an increase in chamber volume. The general trend is predicted by the analytical model. Figure 1.4(b) shows a 20% increase in discharge velocity for a 2.5 increase in orifice diameter. The analytical model does not predict any change in discharge velocity for a varying orifice diameter. Finally, both experiments and the analytical model show a decrease in discharge duration for larger orifice diameters, as depicted in Figure 1.4(c). Finally, an increase in cavity volume yielded an increased discharge time in both the analytical prediction and experimental measurements, Figure 1.4(d). Discharge velocity was extracted from photographs taken with a high speed camera, however, measurement uncertainty was not specified. Difficulties in proper seeding yielded an unsuccessful attempt at particle image velocimetry (PIV) [45]. A CFD simulation predicted the effect of energy deposition and cavity volume on the total impulse. It was shown that an increase in either yielded a larger total volume [2].

A third incarnation of the SparkJet was presented in 2006 to meet the requirements of PIV triggering [3]. The newest device (shown in Figure 1.5) is fashioned from Macor, an insulating ceramic and utilizes three electrodes, a ground electrode, a main electrode and a trigger electrode. High resolution PIV measurements were obtained, as seeding was successful with the use of a fog machine. The velocity field and out of plane vorticity from the experiments are shown in Figure 1.6 at $t = 150\ \mu s$. The maximum velocity of 100 m/s is measured at $t = 200\ \mu s$. Additionally a miniaturized thrust stand was employed to measure force from the device. The impulse bit versus energy deposited is shown in Figure

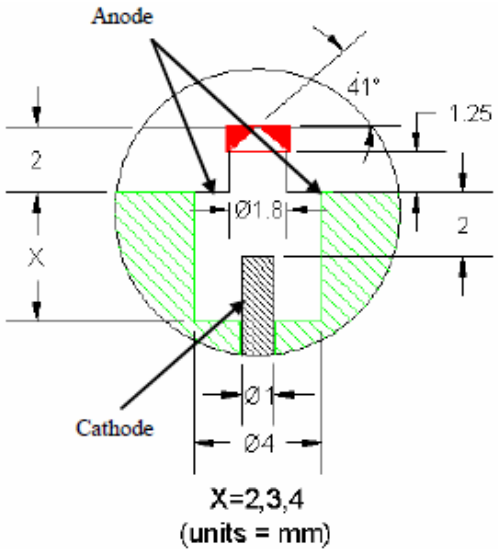

Figure 1.3: Second Generation SparkJet Device [2]

1.7.

In 2011, APL partnered with Florida State University (FSU) to quantify the heating efficiency of the SparkJet [4]. An analytical relation between heating efficiency and internal cavity pressure was deduced. The internal cavity pressure was measured at both APL and FSU with a PCB dynamic pressure sensor. Figure 1.8 shows the heating efficiency deduced from the pressure in blue. A second method, in which the theoretical Joule heating is estimated and compared to current and resistance across the electrodes. The estimation of efficiency is shown in pink in Figure 1.8. The heating efficiency is shown to be between 20% and 30%.

University of Texas Austin

A group at the University of Texas at Austin (UTA) has investigated the SparkJet for use in delay of separation in shock wave/turbulent boundary layer interactions [46]. The device studied at UTA consists of a cathode-anode pair that is pulsed with a high current electric arc. A schematic of the device is shown in Figure 1.9. Experimental characterization of the device in quiescent air at 35 Torr has shown that velocities of 250 m/s can be generated at the cavity exit with 0.5 J of energy deposited [46]. A maximum pulsation frequency was also

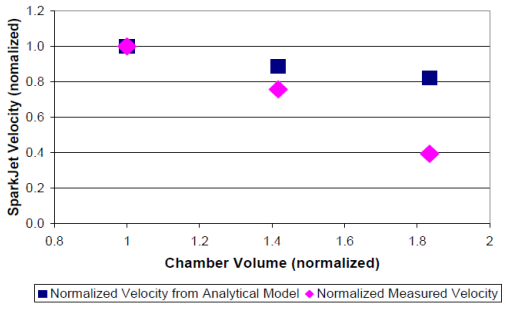

(a) Discharge Velocity Vrs. Orifice Diameter

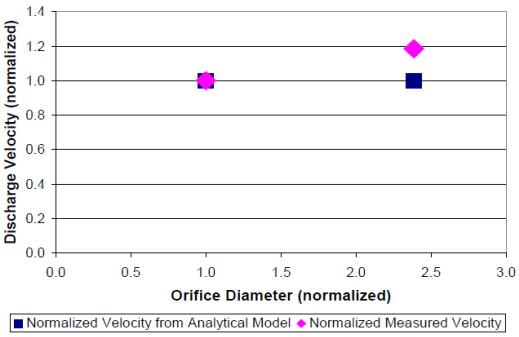

(b) Discharge Velocity Vrs. Cavity Volume

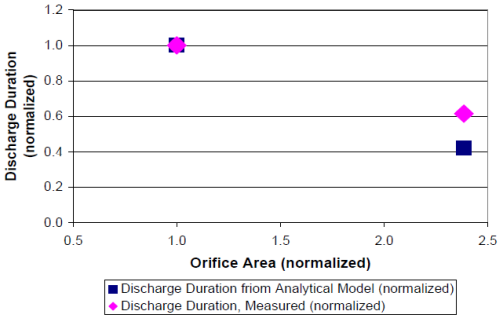

(c) Discharge Duration Vrs. Orifice Diameter

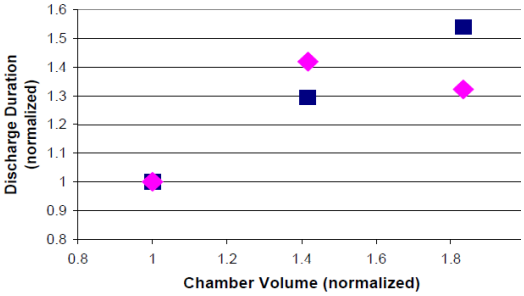

(d) Discharge Duration Vrs. Cavity Volume

Figure 1.4: Parametric Study Performed at APL [2]

Figure 1.5: Third Generation SparkJet Device [3]

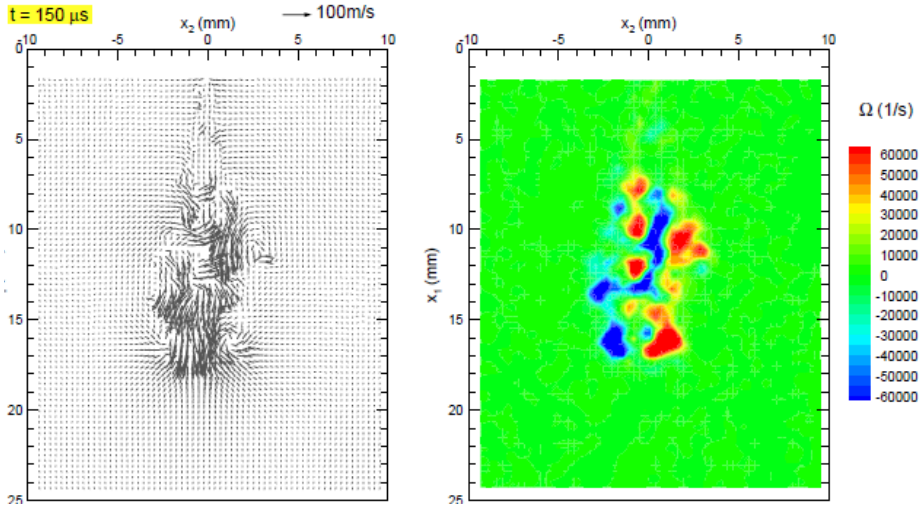

Figure 1.6: Velocity and Vorticity Fields [3]

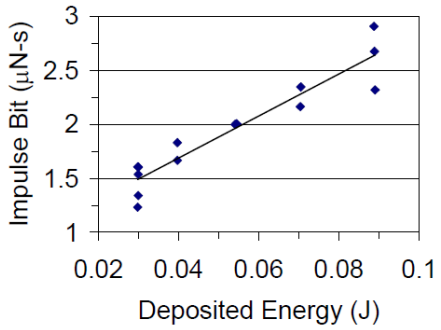

Figure 1.7: Impulse Versus Energy Deposited [3]

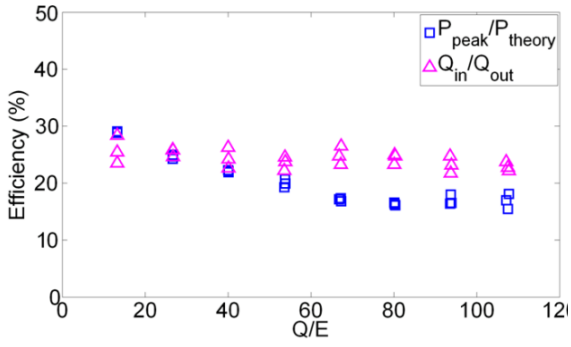

Figure 1.8: Heating Efficiency of SparkJet [4]

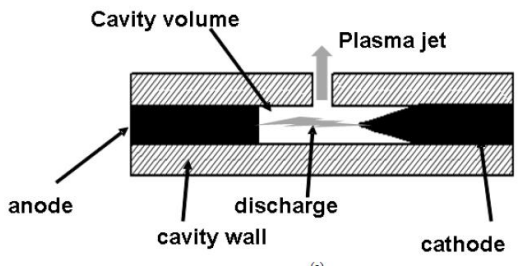

Figure 1.9: SparkJet Device Studied at UTA [5]

found. Pulsing the cavity above 5 kHz lead to misfiring [46]. To investigate the use in shock/ turbulent boundary layer separation, the SparkJet was analyzed in a wind tunnel with a static pressure of 35 Torr. A SparkJet was placed upstream of a 30^o compression corner in Mach 2.76 flow. An upstream movement of the shock foot was noted with the introduction of the SparkJet [46]. Further increase in shock manipulation was observed for SparkJets which were pitched and skewed in relation to the incoming flow [46]. A study of the optimum location of the SparkJet relative to the compression ramp showed that the best location for shock wave manipulation was significantly upstream of the compression ramp. When the SparkJet was pulsed at this location, the shock pulsed upstream at approximately the same frequency as the SparkJet pulsing frequency [5]. The plasma jet was shown to penetrate 1.5 boundary layer thicknesses into a Mach 3 cross flow. A Schlieren image is shown in Figure 1.10 [6]. Additionally, optical emission spectroscopy was performed to determine the rotational and vibrational temperatures of the gas after energy deposition. The heating efficiency of the energy deposition was 10%. The majority of the energy deposited (90%) went into vibrational excitation of the gas.

ONERA

A team at ONERA has examined the SparkJet [43]. Both experiments and computations have been carried out. The experiments study the repetitively pulsed operation of the SparkJet. An experimental optimization of the orifice diameter with a converging exit was performed. CFD results showed that a converging/diverging nozzle is preferable for the

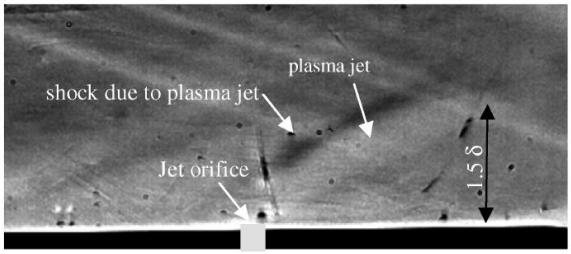

Figure 1.10: SparkJet in Mach 3 Cross Flow [6]

pulsed operation of the SparkJet. The diverging component increased the Mach number of the exhaust by 15%. The feasibility of using the nozzle as a vortex generator was examined computationally. The computations showed the existence of counter-rotating vortices for a skewed jet [43].

Chapter 2

Problem Definition

The goal of this paper is to characterize a single pulse of the SparkJet for flight control. The work begins with a characterization of the jet exiting into quiescent air. Both analytical and computational methods are employed. The SparkJet is also explored issuing into a turbulent supersonic cross flow boundary layer. The SparkJet issuing into the cross flow boundary layer is a computational investigation. Finally, the case of the SparkJet issuing into a quiescent environment is compared to experiments performed at the University of Illinois.

2.1 SparkJet in Quiescent Air

The single pulse of the SparkJet into a quiescent environment is studied as a first step in the characterization of the SparkJet. The problem is fully characterized by five dimensionless parameters, as defined in Table 2.1. The geometric parameters, D, d, L, β are shown in Figure 2.1.

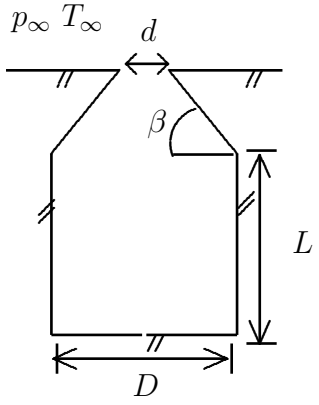

Figure 2.1: Cavity in Quiescent Air

Dimensionless Parameter	Description	Definition	Value
ϵ	Energy Deposition	$Q/p_\infty V$	1, 5, 10
γ	Specific Heat Ratio	c_p/c_v	1.4
δ	Diameter Ratio	d/D	0.1
λ	Cavity Height Ratio	L/D	1
β	Taper Angle	β	47.7^o

Table 2.1: SparkJet in Quiescent Air Dimensionless Parameters

Parameter	Description	Definition	Value
ϵ	Energy Deposition	$Q/p_\infty V$	5
γ	Specific Heat Ratio	c_p/c_v	1.4
δ	Diameter Ratio	d/D	0.1
λ	Cavity Height Ratio	L/D	1
β	Taper Angle	β	47.7^o
M_∞	Freestream Mach Number	u_∞/a_∞	3
Re_θ	Freestream Reynolds Number	$\rho_\infty u_\infty \theta/\mu_\infty$	1400
d/δ	Cavity Diameter to Boundary Layer Height	d/δ	1 and 5

Table 2.2: SparkJet in Cross Flow Dimensionless Parameters

The energy is assumed to be deposited instantaneously at the initial time and heat and pressurize the cavity uniformly. The energy deposited is modeled as a high temperature and pressure region and the details of the plasma physics are not modeled. An analytical model is developed assuming a one-dimensional and quasi-steady flow. The computational analysis is two-dimensional, axi-symmetric and time-accurate. Both methods assume the flow is inviscid and non-heat conducting. Three values of dimensionless energy deposition are computed, $\epsilon = 1, 5, 10$.

2.2 SparkJet in Turbulent Mach 3 Cross Flow

In order to understand how the SparkJet operates within a supersonic flight environment, computations of a single pulse of the SparkJet in a turbulent Mach 3 cross flow are performed. Nine dimensionless parameters characterize the flow, as shown in Table 2.2 where θ refers to the momentum thickness of the boundary layer and the geometry parameters are as shown in Figure 2.2.

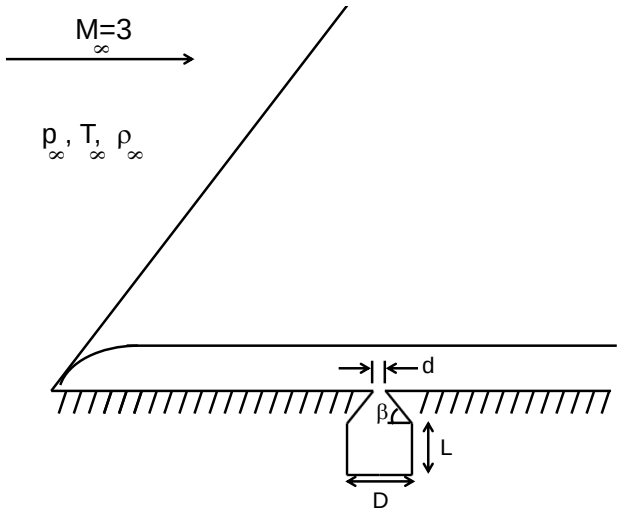

Figure 2.2: Cavity in Cross Flow

Similar to the SparkJet issuing into a quiescent environment, the energy deposition is assumed to be deposited instantaneously at the initial time and heat and pressurize the cavity uniformly. Also similar to the quiescent environment case, the details of the plasma physics are not modeled. The energy deposition parameter is fixed for this study $\epsilon = 5$ and the effect of changing the ratio of the cavity diameter to the boundary layer height is evaluated for $d/\delta = 1$ and 5.

2.3 Comparison to Experiments at University of Illinois

In order to confirm the validity of the computational work, comparisons are made to experimental measurements performed at the University of Illinois. Only the quiescent environment case is evaluated.

2.3.1 SparkJet Exiting into Quiescent Air

A SparkJet-like device was designed and manufactured at the University of Illinois. A schematic of the device is shown in Figure 2.3. The device design differs from those created at other institutions by both the circuitry and the geometry. A high voltage pulse followed by an anode-cathode arc discharge deposits energy rapidly to the air inside the cavity. Additionally, there is a constant diameter cylindrical orifice at the top of the device,

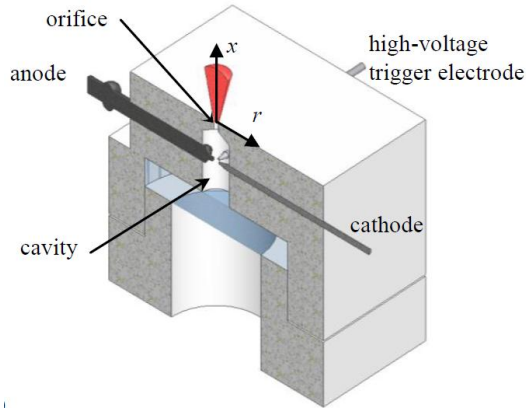

Figure 2.3: Schematic of SparkJet-Like Device Designed at University of Illinois [7]

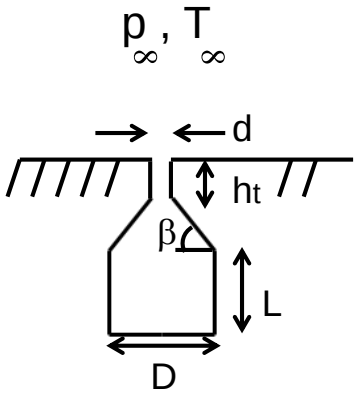

Figure 2.4: Illinois Cavity Cross Section

dimensions are shown in Figure 2.4. A table of the experimental conditions and cavity geometry is shown in Table 2.3. Details of instrumentation and experimental setup can be found in Reedy *et al* [7].

	Ambient Conditions	
p_∞	pressure	99300 Pa
T_∞	temperature	273 K
	Cavity Geometry	
d	orifice diameter	0.83 mm
D	cavity diameter	4.76 mm
L	height of cylindrical cavity	10.16 mm
β	exit angle	31^o
h_t	height of cylindrical throat	1.35 mm
V_e	volume of electrodes	6.7 mm^3
	Energy Deposited	
Q	energy deposition	42, 330, 4000 mJ

Table 2.3: Illinois Experimental Conditions and Cavity Geometry

Chapter 3

Governing Equations

3.1 Single Pulse into Quiescent Air

3.1.1 Governing Equations

The SparkJet issuing into quiescent air assumes laminar and inviscid flow. Thus, the governing equations are the unsteady, compressible Euler equations for a perfect gas.

$$\frac{\partial \rho}{\partial t} + \frac{\partial \rho u_j}{\partial x_j} = 0 \tag{3.1}$$

$$\frac{\partial \rho u_i}{\partial t} + \frac{\partial \rho u_i u_j}{\partial x_j} = -\frac{\partial p}{\partial x_i} \tag{3.2}$$

$$\frac{\partial \rho e}{\partial t} + \frac{\partial (\rho e + p) u_j}{\partial x_j} = 0 \tag{3.3}$$

where ρ is density, p is the pressure, u_i is the velocity in the i^{th} Cartesian coordinate direction x_i and $e = c_v T + \frac{u_j u_j}{2}$ is the total energy per unit mass. The Einstein summation convention is assumed.

3.1.2 Boundary Conditions

A diagram of the boundary conditions for the domain of interest is shown in Figure 3.1. The gas is assumed inviscid in this analysis, and thus the boundary condition at the wall is free slip. The outer boundary of the quiescent flow domain is assumed to be at atmospheric pressure. The outer boundary is sufficiently far from the throat to avoid affecting the flow in the vicinity of the cavity for the duration of the simulations.

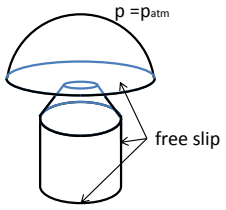

Figure 3.1: Boundary Conditions

3.1.3 Initial Conditions

The initial conditions are shown in Figure 3.2. The fluid above the cavity is assumed to be initially quiescent and at atmospheric conditions. The fluid within the cavity is assumed to be instantaneously and uniformly heated by the energy deposited at $t = 0$.

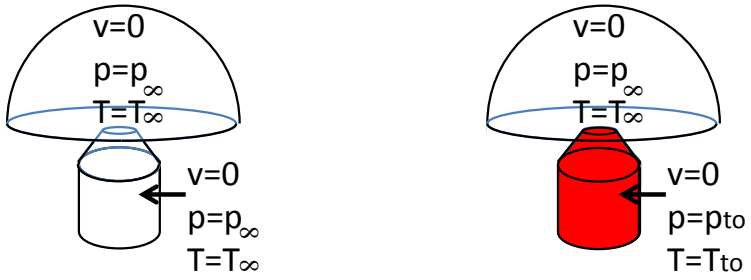

(a) Before Energy Deposited ($t < 0$) (b) After Energy Deposited ($t > 0$)

Figure 3.2: Initial Conditions

The initial conditions in the cavity can be obtained if we know the energy deposited, Q. It is assumed that the density of the gas in the cavity is equal to the freestream density, $\rho_{t_o} = \rho_\infty$, as the energy is deposited. It is also assumed that an amount of the energy, Q, goes into heating the gas. In reality, Q is only a fraction of the actual discharge energy because a fraction of the energy deposition goes into non-equilibrium effects. The initial temperature of the cavity can be found by assuming that energy is added at constant volume ($Q = mc_v\Delta T$) where m is mass and ΔT represents the temperature change. Rearranging, with the ideal gas equation Equation (3.4) is found.

$$T_{t_o} = T_\infty \left[1 + \left(\frac{Q}{p_\infty V}\right)(\gamma - 1)\right] \tag{3.4}$$

The initial pressure can be found from the ideal gas equation, assuming the density in the

cavity remains constant as energy is deposited,

$$\frac{p_{to}}{p_\infty} = \frac{T_{to}}{T_\infty} = \left[1 + \left(\frac{Q}{p_\infty V}\right)(\gamma - 1)\right] \tag{3.5}$$

3.2 Single Pulse into Turbulent Cross-Flow

3.2.1 Governing Equations

The single pulse into a turbulent boundary layer at Mach 3 necessitates the use of the Navier Stokes equations

$$\frac{\partial \rho}{\partial t} + \frac{\partial \rho u_k}{\partial x_k} = 0 \tag{3.6}$$

$$\frac{\partial \rho u_i}{\partial t} + \frac{\partial u_i u_j}{\partial x_j} = -\frac{\partial p}{\partial x_i} + \frac{\partial \tau_{ij}}{\partial x_j} \tag{3.7}$$

$$\frac{\partial \rho e}{\partial t} + \frac{\partial (\rho e + p) u_j}{\partial x_j} = -\frac{\partial q_j}{\partial x_j} + \frac{\partial (u_j \tau_{ij})}{\partial x_j} \tag{3.8}$$

where $\tau_{ij} = -\frac{2}{3}\mu \frac{\partial u_k}{\partial x_k}\delta_{ij} + \mu\left(\frac{\partial u_i}{\partial x_j} + \frac{\partial u_j}{\partial x_i}\right)$.

The grid required to capture the smallest turbulent eddies is very fine and would require a much longer computational time than desired. Instead of resolving the smallest eddies, the Reynolds averaged Navier Stokes equations are employed and a turbulence model is used for closure.

The Reynolds Averaged Navier Stokes equations (RANS) utilizes the Favre average

$$\tilde{f} = \frac{\overline{\rho f}}{\bar{\rho}} \tag{3.9}$$

where $\tilde{f}$ indicates a Favre average of variable f and the overbar indicates an ensemble average. Ensemble averaging takes the average value over an infinite number of datasets,

$$\bar{f} = \lim_{N \to \infty} \frac{1}{N} \sum_{\varphi=1}^{N} f^{(\varphi)} \tag{3.10}$$

where $f^{(\varphi)}$ is the φ^{th} dataset value for f. A decomposition of variable f can be achieved with Favre averaging

$$f = \tilde{f} + f'' \tag{3.11}$$

where f'' is the deviation from the Favre averaged value.

Ensemble averaging is applied to the compressible Navier Stokes equations with some values written in terms of their Favre averages

$$\frac{\partial \bar{\rho}}{\partial t} + \frac{\partial \bar{\rho}\tilde{u}_k}{\partial x_k} = 0 \tag{3.12}$$

$$\frac{\partial \bar{\rho}\tilde{u}_i}{\partial t} + \frac{\partial \bar{\rho}\tilde{u}_i\tilde{u}_k}{\partial x_k} = -\frac{\partial \bar{p}}{\partial x_i} + \frac{\partial}{\partial x_k}\left(-\overline{\rho u_i'' u_k''} + \overline{\tau}_{ik}\right) \tag{3.13}$$

$$\frac{\partial \bar{\rho}\tilde{e}}{\partial t} + \frac{\partial}{\partial x_k}\left(\bar{\rho}\tilde{e} + \bar{p}\right)\tilde{u}_k = \frac{\partial}{\partial x_k}\left(-c_p\overline{\rho T'' u_k''} + \bar{q}_k\right) + \frac{\partial}{\partial x_k}\left(-\overline{\rho u_j'' u_k''}\tilde{u}_j + \bar{\tau}_{jk}\tilde{u}_j\right) \tag{3.14}$$

$$+\frac{\partial}{\partial x_k}\left(-\frac{1}{2}\overline{\rho u_j'' u_j'' u_k''} + \overline{u_j''\tau_{jk}}\right) \tag{3.15}$$

$$\bar{p} = \bar{\rho}R\tilde{T} \tag{3.16}$$

If we assume

$$\frac{\overline{u_i''}}{\tilde{u}} << 1 \quad \text{and} \quad \frac{\overline{T''}}{\tilde{T}} << 1 \tag{3.17}$$

then we can rewrite the molecular shear stress as

$$\bar{\tau}_{ij} = -\frac{2}{3}\tilde{\mu}\frac{\partial \tilde{u}_k}{\partial x_k}\delta_{ij} + \tilde{\mu}\frac{\partial \tilde{u}_i}{\partial x_j} + \tilde{\mu}\frac{\partial \tilde{u}_j}{\partial x_i} \tag{3.18}$$

where $\tilde{\mu} = \mu\left(\tilde{T}\right)$ (not a Favre average) and

$$\bar{q}_k = -k\left(\tilde{T}\right)\frac{\partial \tilde{T}}{\partial x_k} \tag{3.19}$$

which will be denoted as $\tilde{q}_k$. By the same assumption as Equation (3.17),

$$-\frac{1}{2}\overline{\rho u_j'' u_j'' u_k''} << \frac{\partial}{\partial x_k}\left(\bar{\rho}\tilde{e} + \tilde{p}\right)u_k \tag{3.20}$$

thus the term on the left is neglected from the energy equation. Additionally,

$$\overline{u_j''\tau_{jk}} << \tilde{u}_j\bar{\tau}_{jk} \tag{3.21}$$

and the left hand side term is negligible in the context of the energy equation.

Thus, the RANS equations are

$$\frac{\partial \bar{\rho}}{\partial t} + \frac{\partial \bar{\rho}\tilde{u}_k}{\partial x_k} = 0 \tag{3.22}$$

$$\frac{\partial \bar{\rho}\tilde{u}_i}{\partial t} + \frac{\partial \bar{\rho}\tilde{u}_i\tilde{u}_k}{\partial x_k} = -\frac{\partial \bar{p}}{\partial x_i} + \frac{\partial}{\partial x_k}\left(-\overline{\rho u_i'' u_k''} + \bar{\tau}_{ik}\right) \tag{3.23}$$

$$\frac{\partial \bar{\rho}\tilde{e}}{\partial t} + \frac{\partial}{\partial x_k}\left(\bar{\rho}\tilde{e} + \bar{p}\right)\tilde{u}_k = \frac{\partial}{\partial x_k}\left(-c_p\overline{\rho T'' u_k''} + \bar{q}_k\right) + \frac{\partial}{\partial x_k}\left(-\overline{\rho u_j'' u_k''}\tilde{u}_j + \bar{\tau}_{jk}\tilde{u}_j\right) \tag{3.24}$$

$$\bar{p} = \bar{\rho}R\tilde{T} \tag{3.25}$$

where $-\overline{\rho u_i'' u_k''}$ is the Reynolds stress and $-c_p\overline{\rho T'' u_k}$ is the turbulent heat flux. These two new parameters necessitate a turbulence model for closure of the equations.

$$-\overline{\rho u_i'' u_j''} = 2\mu_T\left(S_{ij} - \frac{1}{3}\frac{\partial \tilde{u}_k}{\partial x_k}\delta_{ij}\right) - \frac{2}{3}\bar{\rho}k\delta_{ij} \tag{3.26}$$

$$-c_p\overline{\rho T'' u_k} = -\frac{\mu_T}{Pr_T}c_p\frac{\partial \tilde{T}}{\partial x_j} \tag{3.27}$$

The turbulence model is described in Section 4.3.3.

3.2.2 Boundary Conditions

The boundary conditions are no-slip and adiabatic at the walls of the cavity and external wall. The incoming flow profile is statistically stationary turbulent Mach 3 boundary layer. The incoming flow profile is generated in EDDYBL [47] and interpolated to the grid used in GASPex (Section 4.3).

3.2.3 Initial Conditions

The statistically stationary Mach 3 turbulent boundary layer profile is the initial condition of the ambient flow. The cavity is assumed to be initially at the static pressure and temperature as the freestream for simplicity. The energy is applied instantaneously and uniformly through the cavity. Thus, the transient starts with pressure and temperature in the cavity at p_{to} and T_{to}, respectively, which are governed by Equation (3.5).

3.3 Impulse Definition

The impulse I represents the time-integrated total force induced by the jet. It is defined by Equation (3.28).

$$I(t) = \int_0^t \int_A \left(p - p_\infty + \rho v^2\right) dA\, dt \tag{3.28}$$

where t is the jet discharge time and A is the exit area of the cavity.

To understand why the impulse is the parameter of interest, consider a SparkJet at distance R from the center of gravity of a body, as shown in Figure 3.3.

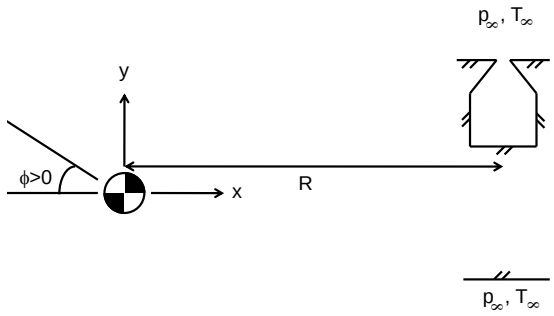

Figure 3.3: Analysis of SparkJet for Flight Control

By the conservation of angular momentum,

$$M\frac{d^2\phi}{dt^2} = \mathcal{T} \tag{3.29}$$

where M is the moment of inertia about the center of gravity of the body, ϕ is the rotation angle, and $\mathcal{T}$ is the torque about the center of gravity. The instantaneous force in the y-direction due to the SparkJet is given by

$$F = \int_A \left(p - p_\infty + \rho v^2\right) dA \tag{3.30}$$

where A is the exit area of the cavity. Thus, the instantaneous torque about the center of gravity due to the SparkJet is

$$\mathcal{T} = R\int_A \left(p - p_\infty + \rho v^2\right) dA \tag{3.31}$$

assuming the cavity dimensions are small compared to R. Thus,

$$M\frac{d^2\phi}{dt^2} = R\int_A \left(p - p_\infty + \rho v^2\right) dA \tag{3.32}$$

For a vehicle maneuver, the rate of rotation is the key parameter. Integrating Equation (3.32) in time, and assuming the rate of rotation is zero at $t = 0$,

$$\frac{M}{R}\frac{d\phi}{dt} = \int_0^{t_f}\int_A \left(p - p_\infty + \rho v^2\right) dA\, dt \tag{3.33}$$

where t_f is the total discharge time of the SparkJet for one pulse. The right hand side of Equation (3.33) is the total impulse, $I(t_f)$, as defined in Equation (3.28).

3.4 Dimensional Analysis

In order to determine the total impulse for the single pulse SparkJet issuing into a quiescent environment, eight dimensional quantities and one angle must be known [1] (see Fig. 2.2).

$$I = f(p_\infty, \rho_\infty, L, d, \beta, D, Q, c_p, c_v) \tag{3.34}$$

Including the impulse, the total number of parameters of the problem is ten. All of the dimensional quantities can be represented by four fundamental units: mass, length, time and temperature. Thus, there are six dimensionless parameters that define the problem. The dimensionless parameters are indicated in Table 3.1.

The dimensionless energy deposition parameter ϵ is proportional to the ratio of the energy added Q to the internal energy of the fluid in the cavity prior to the energy deposition

$$\epsilon = \frac{Q}{p_\infty V} = \frac{Q}{\rho_\infty R T_\infty V} = \frac{1}{(\gamma - 1)}\frac{Q}{m_\infty e_{i_\infty}}$$

where $m_\infty = \rho_\infty V$ is the initial mass in the cavity and $e_{i_\infty} = c_v T_\infty$ is the internal energy per unit mass in the cavity prior to energy deposition. Thus, ϵ is a measure of the magnitude of the energy deposited.

The dimensionless impulse parameter ϑ is proportional to the ratio of the instantaneous impulse generated by the jet to the impulse generated by the collinear elastic collision of a

[1] Here the total impulse $I(t_f)$ is denoted I for simplicity.

rigid body A of mass m_∞ with initial kinetic energy Q to a second rigid body B of identical mass that was initially at rest. This can be seen as follows: assume for $t < 0$ that body A has initial velocity u_A and body B has zero initial velocity. Assume an instantaneous collinear collision at $t = 0$. The momentum of the body B after the collision is $m_\infty u_B = I$ where I is the impulse exerted on B. From conservation of momentum, $m_\infty u_A = m_\infty u_B$, and from conservation of energy, $\frac{1}{2} m_\infty u_A^2 = \frac{1}{2} m_\infty u_B^2 = Q$. Thus, $I = \sqrt{2 m_\infty Q}$.

This analysis assumes that the ratio of specific heats is $\gamma = 1.4$.

Symbol	*Definition*	*Description*
ϵ	$\frac{Q}{p_\infty V}$	energy deposition
ϑ	$\frac{I}{\sqrt{\rho_\infty V Q}}$	impulse
δ	$\frac{d}{D}$	geometry
λ	$\frac{L}{D}$	geometry
β	β	geometry
γ	$\frac{c_p}{c_v}$	specific heat ratio

Table 3.1: Dimensionless Parameters

Chapter 4

Methodology

4.1 SparkJet in Quiescent Environment

4.1.1 Analytical Method

Dimensionless Impulse

An analytical result is obtained for a one-dimensional quasi-steady cavity discharging into quiescent air. The impulse is defined as the force of air from the cavity integrated in time, given by Equation (3.28).

The time integration can be broken into two parts. Assuming constant properties across the exit area,

$$I = \underbrace{\int_0^{t_1} \left(p - p_\infty + \rho v^2\right) A \, dt}_{I_1} + \underbrace{\int_{t_1}^{t_f} \left(p - p_\infty + \rho v^2\right) A \, dt}_{I_2} \tag{4.1}$$

where $0 \leq t \leq t_1$ corresponds to the time interval wherein the flow at the throat is sonic (if such occurs) and $t_1 \leq t \leq t_f$ corresponds to the time interval of subsonic flow which terminates when the total pressure in the cavity equals the ambient pressure.

Minimum Energy Addition for Sonic Flow

The limits of integration of (4.1) depend on whether the energy addition is sufficient for the initially sonic flow at the throat. Since the flow is assumed isentropic from the cavity to the throat,

$$p_{th} = p_t \left[1 + \frac{(\gamma - 1)}{2} M_{th}^2\right]^{-\gamma/(\gamma-1)} \tag{4.2}$$

The initial throat pressure is

$$p_{th_o} = p_{t_o} \left[1 + \frac{(\gamma - 1)}{2} M_{th_o}^2\right]^{-\gamma/(\gamma-1)} \tag{4.3}$$

For initially sonic flow at the throat, $p_{th_o} > p_\infty$ and $M_{th} = 1$. Thus, the condition for initially sonic flow at the throat is

$$\frac{p_{t_o}}{p_\infty} > \left(\frac{\gamma+1}{2}\right)^{\gamma/(\gamma-1)} \tag{4.4}$$

The ratio of initial pressure in the cavity to ambient pressure is given by Equation (3.5). Therefore, the condition for initially sonic velocity at the throat is

$$\frac{Q}{p_\infty V} > \frac{1}{\gamma-1}\left[\left(\frac{\gamma+1}{2}\right)^{\gamma/(\gamma-1)} - 1\right] \simeq 2.23 \text{ for } \gamma = 1.4 \tag{4.5}$$

Subsonic Throat Integral

For the subsonic portion of the discharge, the pressure at the exit p_{th} is equal to the ambient pressure p_∞. Equation (3.28) becomes

$$I_2 = A\int_{t_1}^{t_f} \rho_{th} v_{th}^2 dt \tag{4.6}$$

This is re-written in terms of the total pressure. We introduce the constant, κ and variable, ξ, in terms of the initial cavity total pressure p_{to}, the ambient pressure p_∞ and the instantaneous cavity total pressure p_t.

$$\kappa = \left(\frac{p_{to}}{p_\infty}\right)^{(\gamma-1)/\gamma} \tag{4.7}$$

$$\xi = \left(\frac{p_t}{p_{to}}\right)^{(\gamma-1)/\gamma} \tag{4.8}$$

Since the flow is assumed quasi-steady, the static temperature and velocity at the throat are related to the total temperature inside the cavity by

$$c_p T_{th} + \tfrac{1}{2} v_{th}^2 = c_p T_t \tag{4.9}$$

where T_t is the instantaneous stagnation temperature in the cavity. Therefore, since the flow in the cavity is isentropic,

$$\begin{aligned}
\rho_{th} v_{th}^2 &= \frac{p_{th}}{R T_{th}} 2c_p \left(T_t - T_{th}\right) \\
&= \frac{2c_p}{R}\, p_{th}\left(\frac{T_t}{T_{th}} - 1\right) \\
&= \frac{2\gamma}{\gamma-1}\, p_{th}\left[\left(\frac{p_t}{p_\infty}\right)^{(\gamma-1)/\gamma} - 1\right]
\end{aligned}$$

$$
\begin{aligned}
&= \frac{2\gamma}{\gamma-1}\, p_{th}\left[\left(\frac{p_t}{p_{to}}\frac{p_{to}}{p_\infty}\right)^{(\gamma-1)/\gamma} - 1\right] \\
&= \frac{2\gamma}{\gamma-1}\, p_\infty\,(\kappa\xi - 1) \qquad (4.10)
\end{aligned}
$$

The rate of change of mass $m(t)$ in the cavity is

$$\frac{dm}{dt} = -\dot{m}_{th} \qquad (4.11)$$

and thus

$$dt = -\frac{dm}{\rho_{th} v_{th} A} \qquad (4.12)$$

To find dm,

$$
\begin{aligned}
m &= \rho_t V \\
&= \rho_{t_o}\left(\frac{\rho_t}{\rho_{t_o}}\right) V \\
&= \rho_{t_o} V \left(\frac{p_t}{p_{t_o}}\right)^{1/\gamma} \\
&= \xi^{1/(\gamma-1)} \rho_{t_o} V \qquad (4.13)
\end{aligned}
$$

and thus

$$dm = \frac{\rho_{t_o} V}{\gamma-1}\,\xi^{(2-\gamma)/(\gamma-1)}\, d\xi \qquad (4.14)$$

Furthermore, from (4.9),

$$v_{th} = \sqrt{\frac{2c_p T_{t_o}}{\kappa}\,(\kappa\xi - 1)} \qquad (4.15)$$

Therefore,

$$\rho_{th} v_{th} = \frac{\rho_{th} v_{th}^2}{v_{th}} = p_\infty \frac{2\gamma}{\gamma-1}\sqrt{\frac{\kappa}{2c_p T_{t_o}}}\sqrt{\kappa\xi - 1} \qquad (4.16)$$

and

$$dt = -\frac{\rho_{t_o} V}{2\gamma p_\infty A}\sqrt{\frac{2c_p T_{t_o}}{\kappa}}\,\frac{\xi^{(2-\gamma)/(\gamma-1)}}{\sqrt{\kappa\xi - 1}}\, d\xi \qquad (4.17)$$

combining (4.6), (4.10) and (4.17),

$$I_2 = -\sqrt{\frac{2c_p T_{t_o}}{\kappa}}\,\frac{\rho_{t_o} V}{(\gamma-1)}\int_{\xi_1}^{\xi_f}\sqrt{\kappa\xi - 1}\,\xi^{(2-\gamma)/(\gamma-1)}\, d\xi \qquad (4.18)$$

and for $\gamma = 1.4$,

$$I_2 = -\sqrt{\frac{2c_p T_{t_o}}{\kappa}}\,\frac{\rho_{t_o} V}{0.4}\int_{\xi_1}^{\xi_f}\sqrt{\kappa\xi - 1}\;\xi^{3/2}\, d\xi \qquad (4.19)$$

Introducing a new variable $\alpha^2 = \kappa\xi$,

$$I_2 = -\sqrt{2c_pT_{t_o}}\frac{5\rho_{t_o}V}{\kappa^3}\int_{\alpha_1}^{\alpha_f}\sqrt{\alpha^2-1}\,\alpha^4 d\alpha \tag{4.20}$$

and thus

$$\begin{aligned} I_2 &= -\sqrt{2c_pT_{t_o}}\frac{5\rho_{t_o}V}{\kappa^3}\frac{1}{48}\left[\alpha\sqrt{\alpha^2-1}\left(8\alpha^4-2\alpha^2-3\right)\right. \\ &\quad \left.-3\log\left(\sqrt{\alpha^2-1}+\alpha\right)\right]\Big|_{\alpha_1}^{\alpha_2} \end{aligned} \tag{4.21}$$

The limits of integration can be determined from the definition of α,

$$\alpha = \sqrt{\kappa\xi} = \sqrt{\left(\frac{p_t}{p_{th}}\right)^{\frac{\gamma-1}{\gamma}}} = \sqrt{1+\frac{\gamma-1}{2}M_{th}^2}$$

since $p_{th} = p_\infty$. Thus at $t = t_f$, the final time, $M_{th} = 0$ and $\alpha_f = 1$. If the throat is initially sonic, then t_1 corresponds to the moment when M_{th} just drops below one so $\alpha_1 = \sqrt{1.2}$. If the throat is initially subsonic, $t_1 = 0$ and

$$\begin{aligned} \alpha_1 &= \left(\frac{T_{t_o}}{T_\infty}\right)^{\frac{\gamma-1}{2\gamma}} \\ &= \left[1+(\gamma-1)\,\frac{Q}{p_\infty V}\right]^{(\gamma-1)/2\gamma} \end{aligned} \tag{4.22}$$

Thus, (4.21) becomes

$$\begin{aligned} I_2 &= \frac{5\sqrt{2}}{48}\sqrt{c_pT_{t_o}}\frac{\rho_{t_o}V}{\kappa^3}\left[\alpha_1\sqrt{\alpha_1^2-1}\left(8\alpha_1^4-2\alpha_1^2-3\right)\right. \\ &\quad \left.-3\log\left(\sqrt{\alpha_1^2-1}+\alpha_1\right)\right] \end{aligned} \tag{4.23}$$

The dimensionless impulse ϑ can be expressed in terms of the dimensionless energy deposition ϵ (see Table 3.1) as

$$\begin{aligned} \vartheta_2 = \frac{I_2}{\sqrt{\rho_\infty VQ}} &= \frac{5\sqrt{7}}{48}(\epsilon)^{-1/2}\left[1+\frac{2}{5}\epsilon\right]^{-5/14} \\ &\quad \left[\alpha_1\sqrt{\alpha_1^2-1}\left(8\alpha_1^4-2\alpha_1^2-3\right)\right. \\ &\quad \left.-3\log\left(\sqrt{\alpha_1^2-1}+\alpha_1\right)\right] \end{aligned} \tag{4.24}$$

where

$$\alpha_1 = \begin{cases} \left[1+\frac{2}{5}\epsilon\right]^{1/7} & \text{for } \epsilon < 2.23 \\ \sqrt{1.2} & \text{for } \epsilon \geq 2.23 \end{cases} \tag{4.25}$$

Sonic Throat Integral

Similarly, the first integral can be obtained, noting that the throat Mach number is constant, $M_{th} = 1$.

$$\begin{aligned} I_1 &= A\int_0^{t_1} \left[(p_{th} - p_\infty) + \rho_{th} v_{th}^2\right] dt \\ &= A\int_0^{t_1} p_{th}\left[1 - \frac{p_\infty}{p_{th}} + \gamma M_{th}^2\right] dt \end{aligned} \tag{4.26}$$

$$\tag{4.27}$$

Define

$$\eta = \frac{p_t}{p_{t_o}} \tag{4.28}$$

then

$$\begin{aligned} p_{th} &= p_{t_o}\left(\frac{p_t}{p_{t_o}}\right)\left(\frac{p_{th}}{p_t}\right) \\ &= p_{t_o}\eta\left[1 + \frac{\gamma-1}{2}M_{th}^2\right]^{-\gamma/(\gamma-1)} \\ &= \frac{p_{t_o}}{\sigma}\eta \end{aligned} \tag{4.29}$$

where

$$\sigma = \left(\frac{\gamma+1}{2}\right)^{\gamma/(\gamma-1)} \tag{4.30}$$

and thus

$$\frac{p_\infty}{p_{th}} = \frac{p_\infty}{p_{t_o}}\frac{\sigma}{\eta} \tag{4.31}$$

Therefore

$$I_1 = \frac{p_{t_o}A}{\sigma}\int_0^{t_1}\left[\eta(1+\gamma) - \frac{p_\infty}{p_{t_o}}\sigma\right] dt \tag{4.32}$$

Similar to the subsonic integral case, the time differential can be obtained in terms of total pressure by the mass conservation equation,

$$dt = -\frac{V}{a_{t_o}A\gamma}\left(\frac{\gamma+1}{2}\right)^{\frac{\gamma+1}{2(\gamma-1)}}\eta^{\frac{1-3\gamma}{2\gamma}}d\eta \tag{4.33}$$

Thus,

$$\begin{aligned} I_1 &= -\frac{Vp_{t_o}}{a_{t_o}\gamma\sigma}\left(\frac{\gamma+1}{2}\right)^{\frac{\gamma+1}{2(\gamma-1)}} \\ &\quad \int_{\eta_0}^{\eta_1}\left[(1+\gamma)\,\eta^{\frac{1-\gamma}{2\gamma}} - \frac{p_\infty}{p_{t_o}}\sigma\eta^{\frac{1-3\gamma}{2\gamma}}\right]d\eta \\ I_1 &= -\frac{Vp_{t_o}}{a_{t_o}\gamma}\sigma^{\frac{1-\gamma}{2\gamma}}\left[2\gamma\eta^{\frac{\gamma+1}{2\gamma}} + \frac{p_\infty}{p_{t_o}}\sigma\frac{2\gamma}{\gamma-1}\eta^{\frac{1-\gamma}{2\gamma}}\right]|_{\eta_0}^{\eta_1} \end{aligned}$$

where at $t = 0$, $p_t = p_{t_o} \rightarrow \eta_0 = 1$, and at $t = t_1$, $p_t/p_{t_o} = \frac{p_t}{p_{th}} \frac{p_{th}}{p_{t_o}} = \left(\frac{p_\infty}{p_{t_o}}\right) \sigma \rightarrow \eta_1 = \left(\frac{p_\infty}{p_{t_o}}\right) \sigma$. Thus,

$$I_1 = \frac{V p_{t_o}}{a_{t_o}} \sqrt{\frac{8}{\gamma+1}} \left[1 + \frac{\sigma}{(\gamma-1)} \frac{p_\infty}{p_{t_o}} - \frac{\gamma}{\gamma-1} \left(\frac{p_\infty}{p_{to}} \sigma\right)^{\frac{\gamma+1}{2\gamma}}\right]$$

The dimensionless impulse, ϑ, in terms of dimensionless energy deposition, ϵ is

$$\vartheta_1 = \sqrt{\frac{8}{\gamma(\gamma+1)} \left(\frac{1}{\epsilon} + (\gamma-1)\right)} \left[1 + \frac{\sigma}{\gamma-1} \frac{p_\infty}{p_{t_o}} - \frac{\gamma}{\gamma-1} \left(\frac{\sigma p_\infty}{p_{t_o}}\right)^{\frac{\gamma+1}{2\gamma}}\right] \tag{4.34}$$

where $\frac{p_{t_o}}{p_\infty} = 1 + \epsilon(\gamma - 1)$

If the energy deposition is just enough to create an initially sonic condition at the throat, then $1 + \epsilon(\gamma - 1) = \sigma$, and the sonic impulse is zero.

The subsonic and sonic contributions to the total dimensionless impulse are graphed against each other for varying dimensionless energy deposition parameter in Figure 4.1.

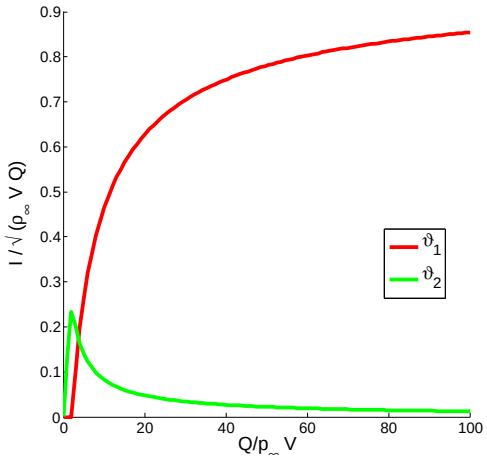

Figure 4.1: Sonic (ϑ_1) and Subsonic (ϑ_2) Contributions to Dimensionless Impulse Versus Dimensionless Energy Deposition

Limit of Dimensionless Impulse

For the dimensionless impulse parameter chosen, ϑ, there exists a finite limit for large dimensionless energy deposition, ϵ.

$$\lim_{\epsilon \rightarrow \infty} \vartheta = \lim_{\epsilon \rightarrow \infty} \vartheta_1 + \lim_{\epsilon \rightarrow \infty} \vartheta_2 \tag{4.35}$$

The first term is the sonic impulse, evaluated from Equation (4.34). The second and third term in the limit go to zero, and the first term remains.

$$\lim_{\epsilon\to\infty}\vartheta_1 \quad = \quad \sqrt{\frac{8\left(\gamma-1\right)}{\gamma\left(\gamma+1\right)}} \tag{4.36}$$

For $\gamma = 1.4$, the limit is 0.976.

The second term in Equation (4.35) is the subsonic impulse. From Equation (4.24),

$$\lim_{\epsilon\to\infty}\vartheta_2 = \frac{5\sqrt{7}}{48}\frac{1}{\sqrt{\epsilon}}\frac{1}{\left(1+\frac{2}{5}\epsilon\right)^{5/14}}\sqrt{1.2} = 0 \tag{4.37}$$

Thus, the limit of the impulse is

$$\lim_{\epsilon\to\infty}\vartheta = \sqrt{\frac{8\left(\gamma-1\right)}{\gamma\left(\gamma+1\right)}} \tag{4.38}$$

Mass in Cavity

Additionally, the mass in the cavity at any given time can be written in terms of total pressure in the cavity

$$m \quad = \quad \rho_t V = \rho_{t_o}\frac{\rho_t}{\rho_{t_o}}V = \rho_{t_o}V\left(\frac{p_t}{p_{t_o}}\right)^{1/\gamma} \tag{4.39}$$

Thus, the mass in the cavity at the end of the discharge cycle divided by the mass at the initial time is

$$\begin{aligned}\frac{m|_{\eta=p_\infty/p_{t_o}}}{m|_{\eta=1}} &= \left(\frac{p_\infty}{p_{t_o}}\right)^{1/\gamma} = \left(\frac{T_\infty}{T_{t_o}}\right)^{1/\gamma} \Rightarrow \\ \frac{m|_{t=t_2}}{m|_{t=0}} &= \left[\frac{1}{1+\epsilon\left(\gamma-1\right)}\right]^{1/\gamma}\end{aligned} \tag{4.40}$$

Discharge Time

Through a similar analysis to the impulse, the total discharge time can be found in terms of the dimensionless energy deposition parameter, ϵ. The integrand is solved assuming a specific heat ratio of air $\gamma = 1.4$. The subsonic integral can be obtained by simplifying (4.17),

$$t_f - t_1 = -\frac{V\kappa^{\frac{\gamma+1}{2(\gamma-1)}}}{2Aa_{to}}\sqrt{\frac{2}{\gamma-1}}\int_{\xi_1}^{\xi_2}\frac{\xi^{\frac{(2-\gamma)}{\gamma-1}}}{\sqrt{\kappa\xi-1}}d\xi \tag{4.41}$$

Introducing $\mu^2 = \kappa\xi - 1$,

$$t_f - t_1 = -\frac{V}{Aa_{to}}\sqrt{\frac{2\kappa}{\gamma-1}}\int_{\mu_1}^{\mu_f}\left(\mu^2+1\right)^{\frac{2-\gamma}{\gamma-1}}d\mu \tag{4.42}$$

for $\epsilon < 2.23$, the flow is initially subsonic and the lower limit of integration is a function of ϵ, $\mu_1 = \sqrt{\kappa - 1}$. For $\epsilon \geq 2.23$, the flow at the throat is initially sonic and the lower limit of integration is constant, $\mu_1 = \sqrt{\frac{\gamma-1}{2}}$. For both cases, the flow at the throat terminates when $p_t = p_\infty$ and $\mu_f = 0$. Thus, the subsonic integral for $\epsilon < 2.23$ is

$$\begin{aligned} t_f - t_1 \quad = \quad & \left(\frac{V}{a_{to}A}\right)\frac{\sqrt{5}}{8}\left(\frac{p_{to}}{p_\infty}\right)^{1/7} \\ & \left\{\sqrt{\left(\frac{p_{to}}{p_\infty}\right)^{2/7}-1}\left[2\left(\frac{p_{to}}{p_\infty}\right)^{3/7}+3\left(\frac{p_{to}}{p_\infty}\right)^{1/7}\right]\right. \\ & \left.+\,3\log\left[\left(\frac{p_{to}}{p_\infty}\right)^{1/7}+\sqrt{\left(\frac{p_{to}}{p_\infty}\right)^{2/7}-1}\right]\right\} \end{aligned} \tag{4.43}$$

For $\epsilon \geq 2.23$,

$$t_f - t_1 = 1.1029\left(\frac{V}{a_{to}A}\right)\left(\frac{p_{to}}{p_\infty}\right)^{1/7} \tag{4.44}$$

The sonic integral for an initially sonic flow at the cavity exit ($\epsilon > 2.23$) is found from Equation (4.33)

$$t_1 = -\frac{V}{a_{t_o}A\gamma}\left(\frac{\gamma+1}{2}\right)^{\frac{\gamma+1}{2(\gamma-1)}}\int_1^{\frac{p_\infty}{p_{to}}\left(\frac{\gamma+1}{2}\right)^{\frac{\gamma}{\gamma-1}}}\eta^{\frac{1-3\gamma}{2\gamma}}d\eta \tag{4.45}$$

This is solved for $\gamma = 1.4$,

$$t_1 = \frac{V}{a_{to}A}8.640\left[0.9129\left(\frac{p_{to}}{p_\infty}\right)^{1/7}-1\right] \tag{4.46}$$

Dimensionless time is introduced

$$\tau = ta_{to}A/V \tag{4.47}$$

The total discharge time for initially sonic flow, $\epsilon \geq 2.23$, is

$$\tau_f = 8.99\left(1+0.4\epsilon\right)^{1/7} - 8.64 \tag{4.48}$$

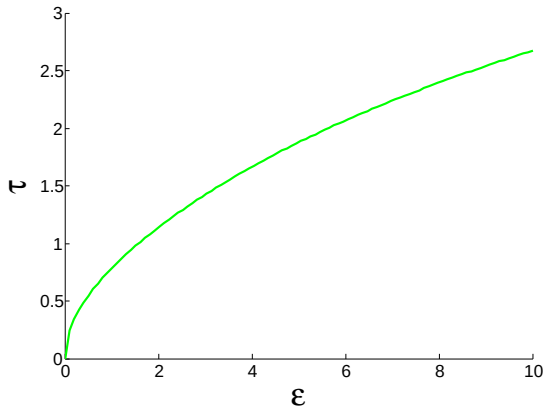

Figure 4.2: Dimensionless Discharge Duration Versus Dimensionless Energy Deposition Parameter for $\gamma = 1.4$

and for $\epsilon < 2.23$,

$$\begin{aligned}\tau_f &= \frac{\sqrt{5}}{8}\left(\frac{p_{to}}{p_\infty}\right)^{1/7} \\ &\quad \left\{\sqrt{\left(\frac{p_{to}}{p_\infty}\right)^{2/7}-1}\left[2\left(\frac{p_{to}}{p_\infty}\right)^{3/7}+3\left(\frac{p_{to}}{p_\infty}\right)^{1/7}\right]\right. \\ &\quad \left.+\,3\log\left[\left(\frac{p_{to}}{p_\infty}\right)^{1/7}+\sqrt{\left(\frac{p_{to}}{p_\infty}\right)^{2/7}-1}\right]\right\} \qquad (4.49)\end{aligned}$$

where

$$\frac{p_{to}}{p_\infty} = 1 + (\gamma - 1)\epsilon \qquad (4.50)$$

The analytical result for the dimensionless discharge time versus dimensionless energy deposition parameter for $\gamma = 1.4$ is shown in Figure 4.2.

It is evident from Equation (4.48), that the discharge time has no theoretical limit as the dimensionless energy deposition parameter approaches infinity. Instead, this is physically limited by the maximum feasible energy density, Q/V.

Total Pressure in Cavity

The total pressure in the cavity can be found from the analytical result for discharge time, Equations (4.17) and (4.33).

For $\epsilon < 2.23$, the following implicit equation is used to solve for the total pressure with numerical root-finding techniques,

$$\begin{aligned}
&\mu\sqrt{\mu^2+1}\left(2\mu^2+5\right)+3\log\left(\mu+\sqrt{\mu^2+1}\right)\\
&-\mu_o\sqrt{\mu_o^2+1}\left(2\mu_o^2+5\right)-3\log\left(\mu_o+\sqrt{\mu_o^2+1}\right)\\
&+\frac{8}{\sqrt{5}}\frac{\tau}{\sqrt{\mu_o^2+1}}=0 \text{ for } \tau\leq\tau_f
\end{aligned} \tag{4.51}$$

where

$$\mu = \sqrt{\left(\frac{p_t}{p_\infty}\right)^{(\gamma-1)/\gamma}-1} \tag{4.52}$$

$$\mu_o = \sqrt{\left(\frac{p_{to}}{p_\infty}\right)^{(\gamma-1)/\gamma}-1} \tag{4.53}$$

$$\frac{p_{to}}{p_\infty} = 1+0.4\epsilon \tag{4.54}$$

For $\epsilon >= 2.23$ for $\tau \leq \tau_1$,

$$\frac{p_t}{p_\infty}=\frac{1+0.4\epsilon}{\left(\frac{\tau}{8.64}+1\right)^7} \tag{4.55}$$

for $\tau > \tau_1$, the following implicit equation can be solved with numerical techniques to find p_t/p_∞ for each τ,

$$\begin{aligned}
&\mu\sqrt{\mu^2+1}\left(2\mu^2+5\right)+3\log\left(\mu+\sqrt{\mu^2+1}\right)\\
&-3.946+\left(\frac{8}{\sqrt{5}}\right)\frac{\tau-\tau_1}{(1+0.4\epsilon)^{1/7}}=0
\end{aligned} \tag{4.56}$$

where τ_1 is the time of the sonic portion of the discharge, from Equation (4.46),

$$\tau_1 = 8.64\left[0.9129\left(1+0.4\epsilon\right)^{1/7}-1\right] \tag{4.57}$$

Similar results for total pressure in time are found for a pressure vessel without energy deposition by Dutton [48].

Total Temperature and Density in Cavity

Knowing the total pressure as a function of time, the total temperature and density can be calculated with the following relations :

$$\frac{T_t}{T_\infty} = \frac{T_t}{T_{to}}\frac{T_{to}}{T_\infty} \tag{4.58}$$

$$= \left(\frac{p_t}{p_{to}}\right)^{(\gamma-1)/\gamma} [1+(\gamma-1)\epsilon] \tag{4.59}$$

$$= \left(\frac{p_t}{p_\infty}\frac{p_\infty}{p_{to}}\right)^{(\gamma-1)/\gamma} [1+(\gamma-1)\epsilon] \tag{4.60}$$

$$= (1+0.4\epsilon)^{5/7}\left(\frac{p_t}{p_\infty}\right)^{2/7} \tag{4.61}$$

$$\begin{aligned}\frac{\rho_t}{\rho_\infty} &= \frac{\rho_t}{\rho_{to}} \\ &= \left(\frac{p_t}{p_{to}}\right)^{1/\gamma} \\ &= \left(\frac{p_t}{p_\infty}\frac{p_\infty}{p_{to}}\right)^{1/\gamma} \\ &= \left(\frac{p_t/p_\infty}{1+0.4\epsilon}\right)^{5/7}\end{aligned} \tag{4.62}$$

Thus, knowing $\frac{p_t}{p_\infty}$ as a function of time, the time-accurate total temperature and density are also known.

4.1.2 Computational Method

The problem is solved using the commercial code ANSYS CFX [49]. The solution domain was discretized in ANSYS ICEM CFD. ANSYS CFX employs a coupled implicit finite volume solver to the Euler equations. The generalized form of the equations are linearized and assembled into a solution matrix. The linearized system is solved using an Incomplete Lower Upper Factorization method with an Algebraic Multigrid Method for accelerated convergence.

Computational Parameters

Linear Equation Solution

The linearized system of equations can be written in a general form :

$$[A]\,\phi = b$$

Start with an approximate solution : ϕ^n.

The residual is calculated : $r^n = b - A\phi^n$.

Find correction : $\phi' = A^{-1}r^n$.

Next solution vector is found : $\phi^{n+1} = \phi^n + \phi'$.

Iterate with ϕ^{n+1} until convergence criteria are met.

where ϕ is the solution vector for the mass and momentum equations.

$$\phi = \left\{ \begin{array}{c} u \\ v \\ w \\ p \end{array} \right\}$$

Algebraic Multigrid Method

CFX uses the Algebraic Multigrid Method to accelerate convergence of the linear equation solution. Typically, iterative solvers are able to quickly converge errors on the order of the grid cell wavelength. However, larger errors take many more iterations to converge. By solving the solution to the same set of equations for conglomerate grid cells, larger errors can be attenuated quickly. The Algebraic Multigrid Method employed in CFX first generates a series of coarser grid systems of equations by adding the control volume cells of the given grid. The coarsest grid set of equations is solved first, then the finer solutions of equations are solved through successive iterations. The finest grid solved is the solution grid input to CFX by the user.

High Speed Numerics

High speed numerics was activated for this simulation. The high speed numerics option activates two numerical techniques which can be useful for high speed flows. The first numerical effect is to dissipate transverse instability near shocks to mitigate the carbuncle effect. The second effect is an activation of the 'high resolution Rhie Chow' option.

Compressibility

The calculation models the flow as compressible. Compressibility was activated in CFX using an ideal gas. The density is not part of the solution vector, and is therefore treated differently in the solution vector, ϕ. The discretization of the density is linearized in terms of the pressure as follows:

$$\begin{aligned}(\rho U)^{n+1} &\cong \rho^{n+1}U^n + \rho^n U^{n+1} - \rho^n U^n \rho^{n+1} \\ &\cong \rho^n + \frac{\partial \rho}{\partial p}|_T \left(p^{n+1} - p^n\right)\end{aligned}$$

Energy Deposition Model

The dimensionless energy deposition parameters, ϵ, are chosen to be 1, 5, and 10 for the three computations. The initial pressure in the cavity was calculated from the ideal gas equation assuming constant density.

Grid

The mesh statistics are shown in Table 4.1. A typical used for the computation is shown in Figures 4.3 and 4.4.

	Cavity	Outer Domain
Elements	822,751	603,211
Avg Length/Side	0.02	0.15

Table 4.1: Mesh Statistics (Lengths are Dimensionless)

A grid refinement study was performed to determine the sensitivity of the dimensionless impulse parameter. A grid with twice the number of cells as the aforementioned grid was run with $\epsilon = 10$. The resulting impulse was 4.8% different from the coarse grid. Thus, the estimated uncertainty in the calculation of the impulse is less than 5%.

Time Step

A time-accurate simulation was performed in CFX. A constant time step was chosen. The time step is presented in non-dimensional form, $\Delta t \; a_{to} A/V$, where a_{to} is the initial speed

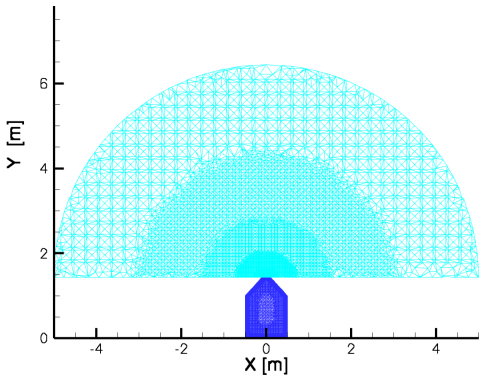

Figure 4.3: Computational Grid

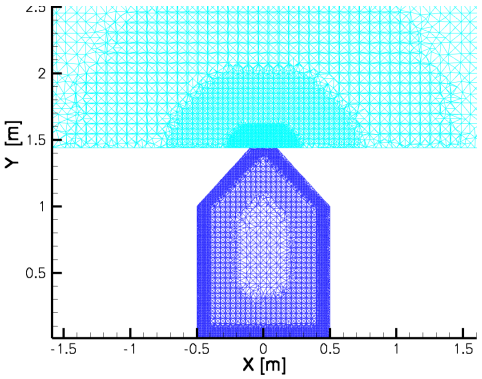

Figure 4.4: Close-Up of Cavity Grid

of sound in the cavity, A is the area of the jet exit and V is the SparkJet cavity volume. A constant dimensionless time step was set for the calculations to 10^{-3} and 10^{-4} for the results and contour calculations, respectively. The contour calculation has a smaller time step to aid in visualization.

To determine if the impulse is sensitive to the time step, the difference between the two computations with time steps an order of magnitude apart were calculated. The difference in dimensionless instantaneous impulse between a computation for $\epsilon = 8.5$ with a dimensionless time steps of 10^{-3} and 10^{-4} is 0.3%, as shown in Table 4.2.

Results Grid $\Delta\tau = 1 \cdot 10^{-3}$	Contour Grid $\Delta\tau = 1 \cdot 10^{-4}$	Difference
13.997	13.951	0.3 %

Table 4.2: Instantaneous dimensionless impulse at $\tau = 0.01$

4.2 Comparison to Illinois Experiments

The comparison to the Illinois SparkJet issuing into a quiescent environment experiments are performed in exactly the same way as the previous computations of a SparkJet issuing into a quiescent environment are solved. ANSYS CFX is used for the computations, and thus the computational methodology described in Section 4.1.2 holds true. The grid and time step are distinctly selected and are described in the following paragraphs.

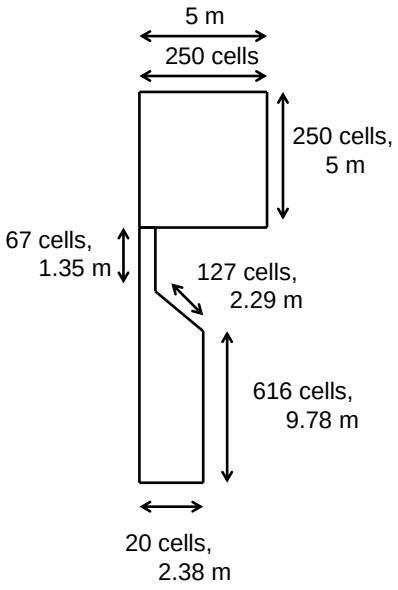

Figure 4.5: Dimensions and Discretization of Illinois SparkJet for Computation

4.2.1 Grid

The relative geometry of the experiments as described in Table 2.3 is retained in the computational model. In order to avoid roundoff error, the lengths are multiplied by 1000. Because the relative dimensions are the same as the experiment, this has no negative impact on the results of the computation. The relative size of the grid cells was chosen to be slightly finer than the resolution of the PIV measurements. To reduce computation time, only a one-degree wedge of the cavity and outer domain was computed. This is a reasonable modification because the problem is axisymmetric about the centerline of the cavity.

The height of the cavity was also modified to account for volume reduction from the electrodes. An estimated 6.7 mm^3 of SparkJet cavity volume was occupied by the electrodes in the Illinois experiments. Thus, the volume of the computational model was reduced by this amount by reducing the height of the cavity. The final dimensions and discretization parameters are shown in Figure 4.5.

4.2.2 Time Step

The time step was conservatively selected for a CFL number less than one. This ensured that the solution was resolved enough to portray accurate flow physics, and that accurate comparison to the Illinois PIV dataset times could be achieved. The timestep was selected to be $\Delta t = 1 \cdot 10^{-5}\ s$, which ensured the time it took for a wave to travel across one cavity cell was captured per timestep.

4.3 SparkJet in Cross Flow

The single pulse into a turbulent boundary layer cross flow was computed using Aerosoft's GASPex finite volume solver. The finite volume solver solves the Reynold's averaged Navier Stokes equations. The fluxes are computed across cell boundaries using Roe's scheme and cell-centered flow variables are reconstructed to cell boundaries using the Modified Upwind Scheme for Conservation Laws (MUSCL). The equations are integrated in time using a dual-time stepping scheme. The $k-\omega$ turbulence model is utilized.

4.3.1 Flux Algorithm: Roe's Scheme

Roe's Scheme is an algorithm which computes the fluxes at the faces of each cell based on the reconstructed conserved variables. The scheme is derived from an exact solution to an approximation of the generalized Riemann problem. Consider the following one-dimensional Euler equations in non-conservative differential form

$$\frac{\partial Q}{\partial t} + A\frac{\partial Q}{\partial x} = 0 \tag{4.63}$$

where A is the Jacobian of the flux matrix $A = \frac{\partial F}{\partial Q}$.

$$A(Q) = \begin{pmatrix} 0 & 1 & 0 \\ (\gamma-3)\frac{u^2}{2} & (3-\gamma)u & \gamma-1 \\ -Hu + \frac{(\gamma-1)u^3}{2} & H-(\gamma-1)u^2 & \gamma u \end{pmatrix} \tag{4.64}$$

where $H = e + \frac{p}{\rho}$ is the total enthalpy.

Roe approximates Equation (4.63) using the averaged values from each side of the cell face

$$\frac{\partial Q}{\partial t} + \tilde{A}\frac{\partial Q}{\partial x} = 0 \tag{4.65}$$

where $\tilde{A}$ is the Roe averaged matrix, a function of the Roe averaged velocity, $\tilde{u}$ and the Roe averaged enthalpy, $\tilde{H}$

$$\tilde{A} = \begin{pmatrix} 0 & 1 & 0 \\ (\gamma-3)\frac{\tilde{u}^2}{2} & (3-\gamma)u & \gamma-1 \\ -\tilde{H}\tilde{u} + \frac{(\gamma-1)\tilde{u}^3}{2} & \tilde{H} - (\gamma-1)\tilde{u}^2 & \gamma\tilde{u} \end{pmatrix} \tag{4.66}$$

where

$$\tilde{u} = \frac{\sqrt{\rho_l}u_l + \sqrt{\rho_r}u_r}{\sqrt{\rho_l}+\sqrt{\rho_r}} \quad \text{and} \quad \tilde{H} = \frac{\sqrt{\rho_l}H_l + \sqrt{\rho_r}H_r}{\sqrt{\rho_l}+\sqrt{\rho_r}}$$

For the exact solution the reader is referred to Knight [50]. Roe's scheme, which is derived from the exact solution, is given below. The faces of each cell correspond to $i+\frac{1}{2}$, and the cell centers correspond to the i locations.

$$F_{i+\frac{1}{2}} = \frac{1}{2}\left(F(Q_l) + F(Q_r) + \sum_{j=1}^{3} \alpha_j \left|\tilde{\lambda}_j\right| \tilde{e}_j \right) \tag{4.67}$$

where

$$\alpha_1 = \left[1 - \frac{(\gamma-1)}{2}\frac{\tilde{u}^2}{\tilde{a}^2}\right]\Delta\rho + \left[(\gamma-1)\frac{\tilde{u}}{\tilde{a}^2}\right]\Delta\rho u - \left[\frac{\gamma-1}{\tilde{a}^2}\right]\Delta\rho e \tag{4.68}$$

$$\alpha_2 = \left[\frac{(\gamma-1)}{4}\frac{\tilde{u}^2}{\tilde{a}^2} - \frac{\tilde{u}}{2\tilde{a}}\right]\Delta\rho + \left[\frac{1}{2\tilde{a}} - \frac{(\gamma-1)}{2}\frac{\tilde{u}}{\tilde{a}^2}\right]\Delta\rho u + \left[\frac{\gamma-1}{2\tilde{a}^2}\right]\Delta\rho e \tag{4.69}$$

$$\alpha_3 = \left[\frac{(\gamma-1)}{4}\frac{\tilde{u}^2}{\tilde{a}^2} + \frac{\tilde{u}}{2\tilde{a}}\right]\Delta\rho - \left[\frac{1}{2\tilde{a}} + \frac{(\gamma-1)}{2}\frac{\tilde{u}}{\tilde{a}^2}\right]\Delta\rho u + \left[\frac{\gamma-1}{2\tilde{a}^2}\right]\Delta\rho e \tag{4.70}$$

where the $\tilde{}$ represents the Roe averaged value

$$\tilde{a} = \sqrt{(\gamma-1)(\tilde{H} - \frac{1}{2}\tilde{u}^2)} \tag{4.71}$$

and the Δ is the difference between values of the left and right side of the cell interface $\Delta\rho = \rho_l - \rho_r$, and similar for the other conserved variables, where all variables denoted with $_l$ and $_r$ are the reconstructed variables at the cell face from the left and right side of the face, respectively.

4.3.2 Reconstruction: Modified Upwind Scheme for Conservation Laws

A second order accurate Modified Upwind Scheme for Conservation Laws (MUSCL) scheme is used to reconstruct the conserved variable vector, Q. As proposed by Anderson *et al* [51], the MUSCL scheme is an upwind scheme that minimizes oscillations at discontinuities by limiting the reconstructed values based on the following conditions :

$$\min(Q_{i-1}, Q_i, Q_{i+1}) \leq Q^l_{i+\frac{1}{2}} \leq \max(Q_{i-1}, Q_i, Q_{i+1}) \tag{4.72}$$

$$\min(Q_{i-1}, Q_i, Q_{i+1}) \leq Q^r_{i-\frac{1}{2}} \leq \max(Q_{i-1}, Q_i, Q_{i+1}) \tag{4.73}$$

The one-dimensional formulation is shown here.

The primitive function is used to integrate the conserved variables, Q, from $x_{i-\frac{3}{2}}$ to an arbitrary x within a given cell.

$$I(x) = \int_{x_{i-\frac{3}{2}}}^{x} \mathcal{Q}\ dx \tag{4.74}$$

for $x_{i-\frac{3}{2}} \leq x \leq x_{i+\frac{1}{2}}$

The integrated quantity is interpolated to second order accuracy by a polynomial interpolation with Newton Basis. The interpolation scheme is

$$P(x) = a_0 + a_1(x - x_{i-\frac{3}{2}}) + a_2(x - x_{i-\frac{1}{2}})(x - x_{i-\frac{3}{2}}) \tag{4.75}$$

where the coefficients, a_0, a_1, and a_2 are found via divided differences [50].

The reconstruction of $\mathcal{Q}$, then, is obtained by differentiating the interpolated integral with respect to x :

$$Q_i(x) = \frac{dP}{dx} \tag{4.76}$$

for $x_{i-\frac{1}{2}} \leq x \leq x_{i+\frac{1}{2}}$ and

$$Q_i(x) \quad = \quad a_1 + a_2\left[(x - x_{i-\frac{1}{2}}) + (x - x_{i-\frac{3}{2}})\right] \tag{4.77}$$

The reconstruction values for the Q at the cell face are

$$Q^l_{i+\frac{1}{2}} = Q_i + \frac{1}{4}\left[(1-\kappa)\widehat{\Delta Q}_{i-\frac{1}{2}} + (1+\kappa)\widehat{\Delta Q}_{i+\frac{1}{2}}\right] \tag{4.78}$$

$$Q^r_{i+\frac{1}{2}} = Q_i - \frac{1}{4}\left[(1-\kappa)\widehat{\Delta Q}_{i+\frac{1}{2}} + (1+\kappa)\widehat{\Delta Q}_{i-\frac{1}{2}}\right] \tag{4.79}$$

For a value of $\kappa = \frac{1}{3}$ the following values of $\widehat{\Delta Q}_{i+\frac{1}{2}}$ are used where $b = (3-\kappa)/(1-\kappa)$.

When $\Delta Q_{i+\frac{1}{2}} \geq 0$ and $\Delta Q_{i-\frac{1}{2}} \geq 0$

$$\widehat{\Delta Q}_{i-\frac{1}{2}} = \begin{cases} \Delta Q_{i-\frac{1}{2}} & \text{if} \quad \Delta Q_{i-\frac{1}{2}} \leq b\Delta Q_{i+\frac{1}{2}} \\ b\Delta Q_{i+\frac{1}{2}} & \text{if} \quad \Delta Q_{i-\frac{1}{2}} > b\Delta Q_{i+\frac{1}{2}} \end{cases} \tag{4.80}$$

$$\widehat{\Delta Q}_{i+\frac{1}{2}} = \begin{cases} \Delta Q_{i+\frac{1}{2}} & \text{if} \quad \Delta Q_{i+\frac{1}{2}} \leq b\Delta Q_{i-\frac{1}{2}} \\ b\Delta Q_{i-\frac{1}{2}} & \text{if} \quad \Delta Q_{i+\frac{1}{2}} > b\Delta Q_{i-\frac{1}{2}} \end{cases} \tag{4.81}$$

When $\Delta Q_{i+\frac{1}{2}} \geq 0$ and $\Delta Q_{i-\frac{1}{2}} \leq 0$

$$\widehat{\Delta Q}_{i-\frac{1}{2}} = \begin{cases} \Delta Q_{i-\frac{1}{2}} & \text{if} \quad \Delta Q_{i-\frac{1}{2}} \geq -2\Delta Q_{i+\frac{1}{2}} \\ -2\Delta Q_{i+\frac{1}{2}} & \text{if} \quad \Delta Q_{i-\frac{1}{2}} < -2\Delta Q_{i+\frac{1}{2}} \end{cases} \tag{4.82}$$

$$\widehat{\Delta Q}_{i+\frac{1}{2}} = \begin{cases} \Delta Q_{i+\frac{1}{2}} & \text{if} \quad \Delta Q_{i+\frac{1}{2}} \leq -2\Delta Q_{i-\frac{1}{2}} \\ -2\Delta Q_{i-\frac{1}{2}} & \text{if} \quad \Delta Q_{i+\frac{1}{2}} > -2\Delta Q_{i-\frac{1}{2}} \end{cases} \tag{4.83}$$

When $\Delta Q_{i+\frac{1}{2}} \leq 0$ and $\Delta Q_{i-\frac{1}{2}} \leq 0$

$$\widehat{\Delta Q}_{i-\frac{1}{2}} = \begin{cases} \Delta Q_{i-\frac{1}{2}} & \text{if} \quad \Delta Q_{i-\frac{1}{2}} \geq b\Delta Q_{i+\frac{1}{2}} \\ b\Delta Q_{i+\frac{1}{2}} & \text{if} \quad \Delta Q_{i-\frac{1}{2}} < b\Delta Q_{i+\frac{1}{2}} \end{cases} \tag{4.84}$$

$$\widehat{\Delta Q}_{i+\frac{1}{2}} = \begin{cases} \Delta Q_{i+\frac{1}{2}} & \text{if} \quad \Delta Q_{i+\frac{1}{2}} \geq b\Delta Q_{i-\frac{1}{2}} \\ b\Delta Q_{i-\frac{1}{2}} & \text{if} \quad \Delta Q_{i+\frac{1}{2}} < b\Delta Q_{i-\frac{1}{2}} \end{cases} \tag{4.85}$$

When $\Delta Q_{i+\frac{1}{2}} \leq 0$ and $\Delta Q_{i-\frac{1}{2}} \geq 0$

$$\widehat{\Delta Q}_{i-\frac{1}{2}} = \begin{cases} \Delta Q_{i-\frac{1}{2}} & \text{if} \quad \Delta Q_{i-\frac{1}{2}} \leq -2\Delta Q_{i+\frac{1}{2}} \\ -2\Delta Q_{i+\frac{1}{2}} & \text{if} \quad \Delta Q_{i-\frac{1}{2}} > -2\Delta Q_{i+\frac{1}{2}} \end{cases} \tag{4.86}$$

$$\widehat{\Delta Q}_{i+\frac{1}{2}} = \begin{cases} \Delta Q_{i+\frac{1}{2}} & \text{if} \quad \Delta Q_{i+\frac{1}{2}} \geq -2\Delta Q_{i-\frac{1}{2}} \\ -2\Delta Q_{i-\frac{1}{2}} & \text{if} \quad \Delta Q_{i+\frac{1}{2}} < -2\Delta Q_{i-\frac{1}{2}} \end{cases} \tag{4.87}$$

4.3.3 Turbulence Evaluation

According to Morkovin's Hypothesis [52] the density fluctuations have little effect on the structure of the turbulence provided that $\sqrt{\overline{\rho'^2}} << \bar{\rho}$. Morkovin's hypothesis allows the extension of incompressible turbulence models to compressible flows below Mach 5.

The Wilcox 1988a $k-\omega$ [47] is employed to close the system of equations. The $k-\omega$ model is a two-equation model, and thus determines turbulence parameters k and ω without knowledge of the upstream turbulence. Two partial differential equations for the turbulent kinetic energy, k and specific dissipation rate, ω, are solved alongside of the RANS equations. Eddy viscosity, μ_T, dissipation ϵ and turbulent length scale, l, are given in terms of k and ω.

$$\rho\frac{\partial k}{\partial t}+\rho u_j\frac{\partial k}{\partial x_j}=\tau_{ij}\frac{\partial u_i}{\partial x_j}-\beta^*\rho k\omega+\frac{\partial}{\partial x_j}\left[\left(\mu+\sigma^*\mu_T\right)\frac{\partial k}{\partial x_j}\right] \tag{4.88}$$

$$\rho\frac{\partial \omega}{\partial t}+\rho u_j\frac{\partial \omega}{\partial x_j}=\alpha\frac{\omega}{k}\tau_{ij}\frac{\partial u_i}{\partial x_j}-\beta\rho\omega^2+\frac{\partial}{\partial x_j}\left[\left(\mu+\sigma\mu_T\right)\frac{\partial \omega}{\partial x_j}\right] \tag{4.89}$$

$$\alpha=\frac{5}{9},\quad \beta=\frac{3}{40},\quad \beta^*=\frac{9}{100},\quad \sigma=\frac{1}{2},\quad \sigma^*=\frac{1}{2} \tag{4.90}$$

$$\mu_T=\frac{\rho k}{\omega},\quad \epsilon=\beta^*\omega k,\quad l=\frac{k^{1/2}}{\omega} \tag{4.91}$$

At the grid points closest to the wall, k and ω are given by $k=\frac{u_\tau^2}{\sqrt{\beta^*}}$ $\omega=\frac{u_\tau}{\sqrt{\beta^*}\kappa y}$ where u_τ is the friction velocity and κ is the von Karman constant.

4.3.4 Time Integration

The governing equations were integrated in time with a second order implicit dual-time step integration scheme. Dual time stepping introduces a term which is a derivative in a pseudo time to the governing equations. The modified equations are integrated in pseudo time until a steady state in pseudo time is reached and the introduced derivative term is driven to zero. For faster convergence, additional inner iterations were performed on a linearized set of equations for each of the iterations performed in the dual-time stepping.

Dual-Time Stepping

The Navier Stokes equations written in control volume form can be written

$$\frac{\partial}{\partial t}\int\int\int Q dt + \int\int_{S(t)} (F - F_v)\cdot \hat{n} dS - \int\int\int_{V(t)} W dV = 0 \tag{4.92}$$

where Q represents a vector of conserved quantities, F is the flux vector and W represents the source terms.

The dual time-stepping scheme introduces a new term to the left hand side, which is a derivative in pseudo time.

$$\frac{\partial}{\partial \tau}\int\int\int Q dV + \frac{\partial}{\partial t}\int\int\int_{V(t)} Q dV + \int\int_{S(t)} (F - F_v)\cdot \hat{n} dS - \int\int\int_{V(t)} W dV = 0 \tag{4.93}$$

The modified equations are then integrated in pseudo time until a steady state is reached in pseudo time. That is, the equations are integrated until the first term in 4.93 approaches zero and equation 4.93 approaches equation 4.92.

Additional Inner Iterations

GASP recommends iterating a linearized form of the system of equations within each pseudo-time iteration for faster convergence. Gauss-Seidel relaxation scheme is used to linearize the system of equations and iterations are performed on the linearized system. The resulting conserved variable solution updates the non-linear system in equation 4.93.

4.3.5 Validation of Turbulence in GASPex and EDDYBL

A statistically stationary turbulent boundary layer flow is imported from EDDYBL for the inflow condition. An inflow condition of Mach 3, $T_\infty = 293$ K and $p_\infty = 101325$ Pa over an adiabatic wall was used in the EDDYBL simulation. The boundary layer was modeled with 218 grid points. The conditions at the end of the EDDYBL domain with a Reynolds number based on momentum thickness of 1400 was imported to GASPex. To verify the $k-\omega$ model in GASPex and EDDYBL, they were compared against theoretical values for U^* and c_f. Both the EDDYBL and GASPex computations started with a statistically stationary inflow boundary layer from EDDYBL at $Re_\theta = 1400$. Both computations were computed

for at least ten boundary layer lengths before comparison with theoretical profiles. The theoretical formulas are given below.

Theory

Velocity Profile

The velocity profile for a compressible turbulent boundary layer is approximated with three correlations, one for the viscous sublayer, one for the logarithmic region and one for the wake region. The three relations are given below [53]

Transformed Distance and Velocity

The compressible correlations are defined in terms of a transformed distance velocity, y^+ and U^*, respectively.

$$y^+ = \frac{y u_\tau}{\nu_w} \tag{4.94}$$

where u_τ is the friction velocity, ν_w is the kinematic viscosity at the wall.

$$u_\tau = \sqrt{\frac{\tau_w}{\rho_w}} \tag{4.95}$$

where τ and ρ are the shear stress and density, respectively.

To account for the effect of compressibility, a density weighted function is used

$$U^* = \int_{u_w}^{u} \sqrt{\frac{T_w}{T}} du \tag{4.96}$$

where u is velocity, T is temperature, the subscript w is the condition at the wall.

Logarithmic Region

The transformed velocity in the viscous sublayer is given by the empirical equation:

$$\frac{U^*}{u_\tau} = \frac{1}{\kappa} \log y^+ + C^* \tag{4.97}$$

where C^* is a constant for an adiabatic flow, it was chosen as 5.0, to match the value that EDDYBL uses. The parameter κ is also constant, chosen as 0.41 to match EDDYBL.

Wake Region

The portion of the boundary layer closest to the edge looks similar to a wake region. The empirical equation for the wake region is as follows

$$\frac{u^*}{u_\tau} = \frac{1}{\kappa}\log y^+ + C^* + \frac{\Pi}{\kappa}w(\frac{y}{\delta}) \tag{4.98}$$

where Π is a measure of the strength of the wake, it was taken to be 0.55 in this computation, $w(\frac{y}{\delta})$ is Cole's wake function $w(\frac{y}{\delta}) = 2\sin^2(\frac{\pi}{2}\frac{y}{\delta})$.

Skin Friction

The prediction of skin friction in supersonic flow utilizes subsonic flow theory. A correlation between incompressible and compressible flow is used to match the subsonic skin friction theory to compressible flow.

The Karman-Schoenherr equation in terms of Re_θ [54] relates the skin friction to Reynolds number.

$$\left(\frac{1}{\sqrt{\overline{C_f}}}\right) = 17.08\left(\log_{10}\overline{Re_\theta}\right)^2 + 25.11\log_{10}\overline{Re_\theta} + 6.012 \tag{4.99}$$

where the $\overline{C_f}$ and $\overline{Re_\theta}$ are the incompressible skin friction and Reynolds number based on momentum thickness, respectively.

To relate the compressible and incompressible skin friction, transform functions, F_c and F_θ are introduced [54]

$$\overline{C_f} = F_c C_f \tag{4.100}$$

$$\overline{Re_\theta} = F_\theta Re_\theta \tag{4.101}$$

where C_f and Re_θ are the compressible skin friction and Reynolds number based on momentum thickness, respectively.

Van Driest [55] introduced the following transform

$$F_c = \frac{rm}{\left(\sin^{-1}\alpha + \sin^{-1}\beta\right)^2} \tag{4.102}$$

$$F_\theta = \frac{\mu_e}{\mu_w} \tag{4.103}$$

$$r = 0.9 \tag{4.104}$$

$$m = 0.2M_e^2 \tag{4.105}$$

$$\alpha = \frac{2A^2 - B}{\sqrt{4A^2 + B^2}} \tag{4.106}$$

$$\beta = \frac{B}{\sqrt{4A^2 + B^2}} \tag{4.107}$$

$$A = sqrt\frac{rm}{F} \tag{4.108}$$

$$B = \frac{1 + rm - F}{F} \tag{4.109}$$

$$F = \frac{T_w}{T_e} \tag{4.110}$$

where subscripts w and e represent the wall and edge conditions, respectively.

Velocity Profile Comparison

The boundary layer velocity profile from the GASPex computation at the steady state value just above the centerline of the cavity is shown with the theoretical profile in Figure 4.6. The profile agrees within 10% of the theoretical value, which is reasonable.

The comparison of the EDDYBL boundary layer velocity profile is shown against the theoretical values in Figure 4.7. The profile agrees well with the theory.

Skin Friction

The comparison of the EDDYBL and GASPex computation of skin friction versus Reynolds number based on momentum thickness is shown in Figure 4.8. The values from both computations fall within ten percent of the theoretical values for skin friction based on Reynolds number.

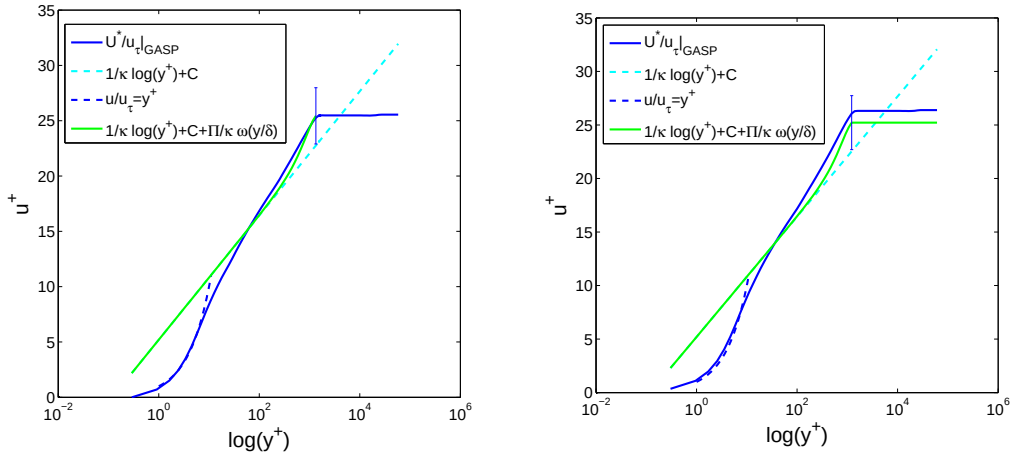

(a) $d/\delta = 1$ (b) $d/\delta = 5$

Figure 4.6: Boundary Layer Profile in Steady State

4.3.6 Grid

Resolving the Boundary Layer

To accurately resolve the boundary layer y^+ should be less than one, where $y^+ = yu_\tau/\nu_w$, u_τ is the friction velocity, $u_\tau = \sqrt{\frac{\tau_w}{\rho_w}}$, τ_w and ρ_w are the shear stress and the density at the wall, respectively, ν_w is the kinematic viscosity at the wall, $\nu_w = \mu_w/\rho_w$. The y^+ value was estimated using the values from EDDYBL at the inflow condition. Previous studies show that EDDYBL and CFX predict the temperature at the wall and hence the viscosity at the wall differently, which effects the y^+ value, so a scaling parameter was used, calculated from previous studies, to account for this difference. The final value of the height of the first cell in the boundary layer was chosen to be $1 \cdot 10^{-6}$ m. This corresponds to $y^+ = 0.3$.

Views of the grid from the top, side and bottom are shown in Figure 4.9. The red indicates the collar region, which is a refined cylindrical grid in the outer domain which captures the jet flow.

Bow Shock Upstream of Jet

The jet will act temporarily as a flow obstruction that generates a bow shock upstream. The maximum distance upstream the bow shock will be from the jet can be estimated by

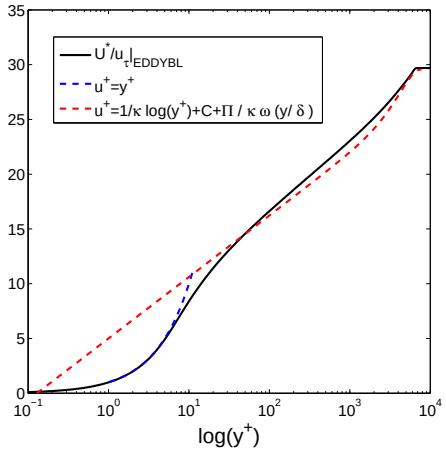

(a) $d/\delta = 1$ and $d/\delta = 5$

Figure 4.7: EDDYBL Boundary Layer Profile in Steady State

the steady state value of a solid cylinder in the same flow situation. From Hirschel [56], the bow shock will sit one cylinder diameter upstream from a cylinder in Mach 3 flow. The jet was placed ten cylinder diameters downstream from the inflow boundary condition to account for any further upstream bow shock movement.

Symmetry of the Domain

To reduce the number of cells in the domain, the symmetry about the plane normal to the flow direction was utilized. The number of cells was reduced by a factor of two by use of the symmetry.

4.3.7 Time Step

Because the dual-time stepping scheme is used for the cross-flow computations, the solution is stable for all time steps (it is not CFL limited). Thus, a time-step based on the flow physics was chosen for each. The relevant physical parameter by which to limit the time scheme is the time it takes for a sonic wave to travel across the cavity. There should be at least ten timesteps within the timespan of a wave traversing the SparkJet cavity. The $d/\delta = 1$ and $d/\delta = 5$ cases had a timestep of $\Delta t = 1 \cdot 10^{-8}$ s. This corresponds to a CFL=5,

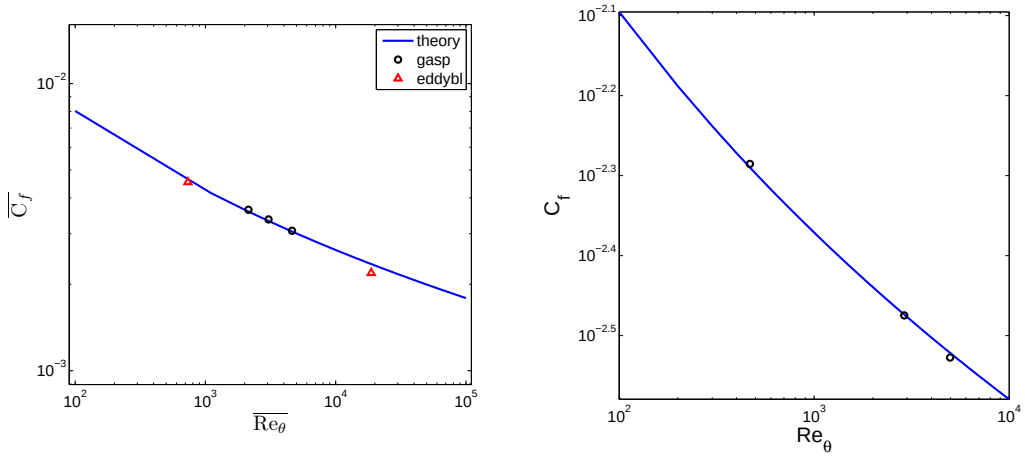

(a) $d/\delta = 1$ (b) $d/\delta = 5$

Figure 4.8: Skin Friction Vrs. Reynold's Number in Steady State

and hundreds of timesteps for each sonic wave traverse of the cavity. Such a small timestep was used because a solution could not be found for larger timesteps.

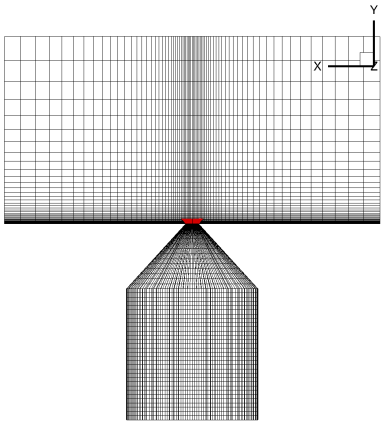

(a) Side View

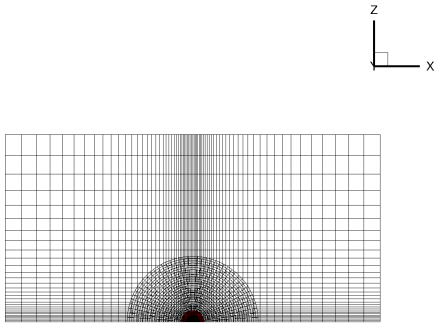

(b) Bottom View

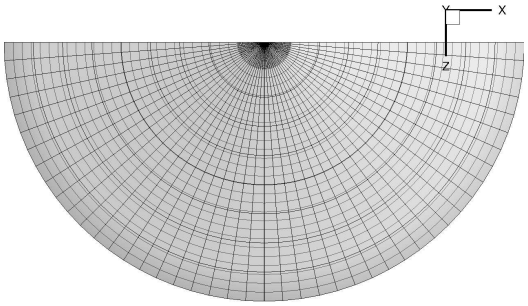

(c) Cavity Top

Figure 4.9: Grid

Chapter 5

Results

5.1 Single Pulse in Quiescent Air

5.1.1 Comparison of Computation to Analysis

Dimensionless Impulse and Mass Fraction

Three different energy deposition parameter values, $Q/p_\infty V$, were computed to quantify a relationship between the analytical solution and the CFD calculation. Both the computational method and analytical method assume that the flow is inviscid. However, the analytical calculation assumes one-dimensional and quasi-steady flow, while the computational calculation accounts for shape effects (axisymmetric, two-dimensional) and unsteady effects (time-dependency). Thus, the comparison of the computational to the analytical result will quantify the effect of shape and dependency on time. The three values for dimensionless energy deposition parameter are shown in Table 5.1 together with the geometric parameters.

$\frac{Q}{p_\infty V}$	1	5	10
$\frac{L}{D}$		1	
$\frac{d}{D}$		0.2	
β		47.7^o	

Table 5.1: Three Values of Dimensionless Energy Deposition

A comparison of the dimensionless impulse and mass fraction at the end of the discharge cycle is shown in Figures 5.1 and 5.2, respectively. The dimensionless impulse demonstrates

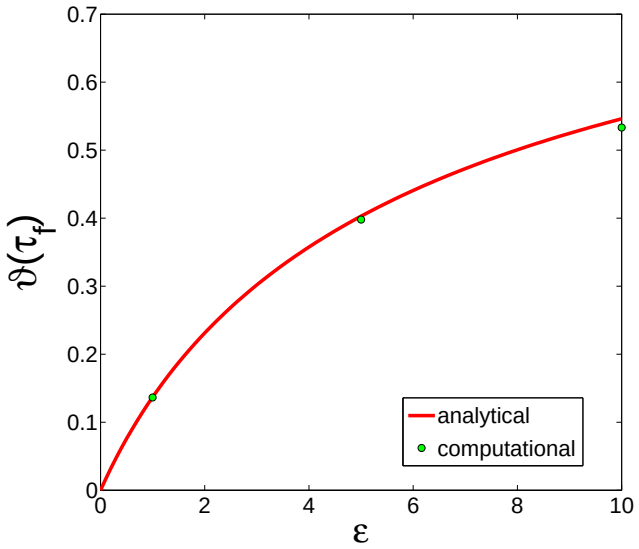

Figure 5.1: Impulse Results for $\gamma = 1.4$

close agreement between the analytical and computational result. The difference between the analytical and computed impulse is 0.4%, 1.3% and 2.3% for $Q/p_\infty V = 1$, 5, and 10, respectively. The difference between the computational result and the analytical result falls within the error of uncertainty of the calculation. The dimensionless mass in the cavity at the end of the discharge is shown in Figure 5.2. The difference between the analytical and computational dimensionless mass in the cavity at the end of discharge falls within the uncertainty of the calculation.

Total Pressure in Cavity

The results are graphed in Figure 5.3. The one-dimensional analysis reasonably predicts the total pressure in the cavity. The maximum instantaneous error is 14%, as seen in Table 5.2.

Table 5.2: Difference Between One-Dimensional Analysis Prediction and Computational Prediction of Total Pressure in Cavity

ϵ	Maximum Difference	τ at Maximum Error
1	6.5%	0.3
5	12.2%	1.3
10	14.0%	2.1

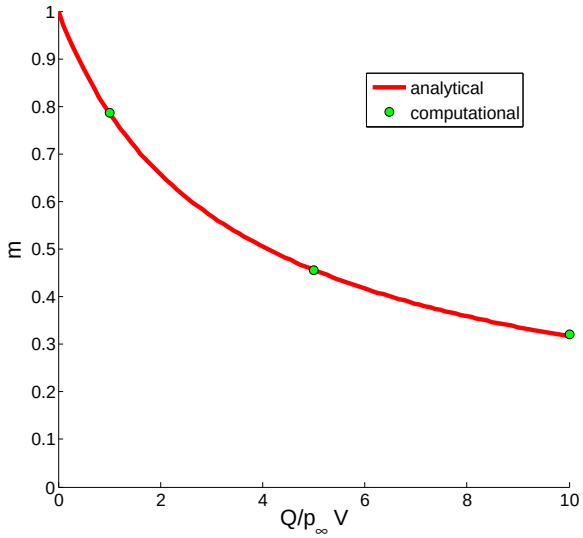

Figure 5.2: Mass in Cavity at End of Pulse for $\gamma = 1.4$

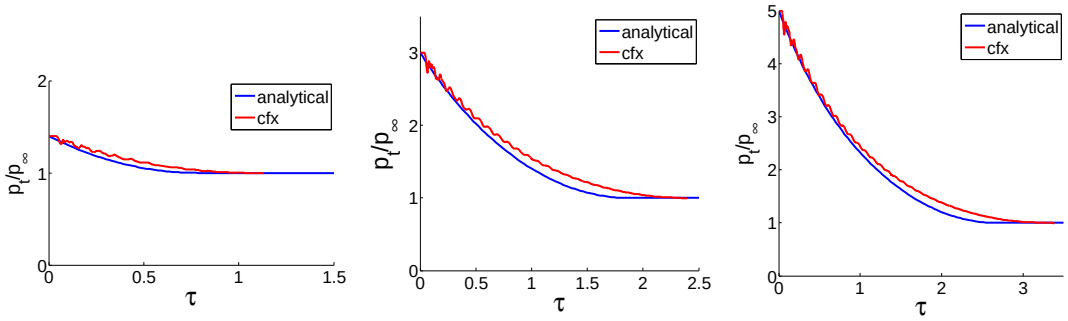

(a) $\epsilon = 1$ (b) $\epsilon = 5$ (c) $\epsilon = 10$

Figure 5.3: Total Pressure in Cavity Versus Time, Analytical and Computational Results

5.1.2 Monte Carlo Analysis of Geometrical Sensitivity

The close agreement between the analytical and computational results suggests that the dimensionless impulse and mass at the end of the discharge cycle are essentially independent of the dimensionless geometry parameters of the cavity. The analytical study is one-dimensional; in essence, it assumes that the geometry has an aerodynamic throat, but no other geometric parameters are considered. The fact that the computations, which model the geometry, agree closely with the analytical results indicates that the dimensionless impulse is insensitive to the geometry (for the uniformly distributed energy deposition assumed in this study). To test this theory, a computational geometry sensitivity study was performed. The sensitivity of the impulse to the geometry parameters is evaluated. The geometry of the cavity is fully described by three dimensionless quantities, L/D, d/D and β. Instead of exhausting each of the three parameters and their infinite combinations with the other parameters, a Monte Carlo study was performed. Ten analyses were performed with randomly generated values for each of the three dimensionless geometry parameters. Each of the parameters were found using MATLAB's random number generator, and were confined to the following limits

$$0.1 \leq \frac{d}{D} \leq 0.5 \tag{5.1}$$

$$1 \leq \frac{L}{D} \leq 10 \tag{5.2}$$

$$30^o \leq \beta \leq 60^o \tag{5.3}$$

Dimensionless Impulse

The sensitivity of impulse to the energy deposition parameter is known, so a fixed value of $\epsilon = 5$ was chosen. The external domain was extended to $10D$ in all directions in order account for longer discharge times, to reduce the influence of reflected sonic waves produced by the cavity on the impulse.

The resulting parameters are shown in Table 5.3. The values of dimensionless impulse are shown in Table 5.4, and graphed versus case number in Figure 5.4. The resulting values indicate that the dimensionless impulse is insensitive to the dimensionless geometry

parameters of the cavity.

Table 5.3: Random Values for Sensitivity Study

Case*	$\frac{d}{D}$	$\frac{L}{D}$	β
1	0.30	9.1	36^o
2	0.46	7.3	33^o
3	0.22	8.2	45^o
4	0.42	7.3	60^o
5	0.26	4.6	39^o
6	0.34	7.3	48^o
7	0.14	2.8	36^o
8	0.14	7.3	54^o
9	0.30	1.0	39^o
10	0.42	3.7	45^o

*$\epsilon = 5$ in all cases

Table 5.4: Random Values for Sensitivity Study

Case	$\frac{I}{\sqrt{\rho_\infty V Q}}$
1	0.4166
2	0.4118
3	0.4148
4	0.4118
5	0.4052
6	0.4100
7	0.4099
8	0.3924
9	0.4188
10	0.4180
analytical	0.4029
standard deviation	0.006
maximum error	4%

Dimensionless Discharge Time

The dimensionless discharge time results were evaluated for each of the Monte Carlo geometry sensitivity cases. The discharge time was taken to be the time that the velocity integrated over the cavity exit was zero, *i.e.* the dimensionless time (tAa_{to}/V) at which $\int_A v dA = 0$.

The dimensionless discharge time is somewhat sensitive to geometry. The discharge time are graphed for each case number in Figure 5.5. The maximum difference between the

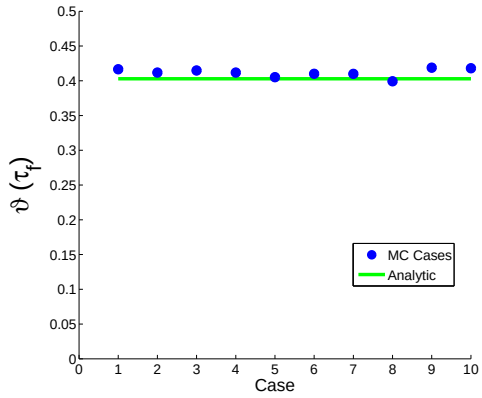

Figure 5.4: Dimensionless Impulse for Each Geometry Variation

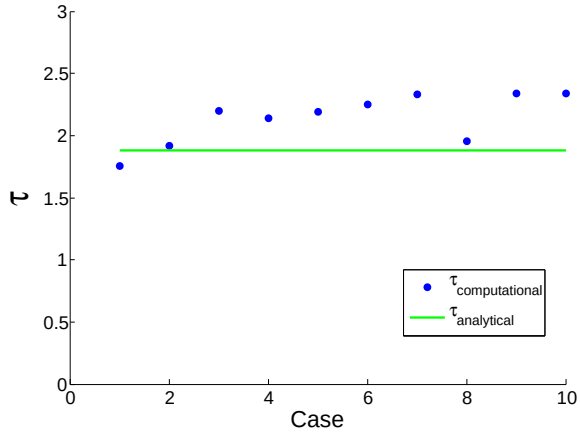

Figure 5.5: Dimensionless Discharge Time for Each Geometry Variation

analytical and computed discharge times is 24%, and the dimensionless standard deviation is 0.2. A graph of the velocity integrated over the discharge orifice area versus time for Monte Carlo case 8 is shown in Figure 5.6. The dimensionless time between peaks is 0.0408, which corresponds to the dimensionless time required for an acoustic wave to traverse the length of the cavity twice based on the initial stagnation temperature. In dimensional terms, for a cavity with a volume of 100 mm^3 and a discharge diameter of 1 mm (such as the cavity given in the dimensional example, Chapter 7.1), this would be 15 μs. The velocity at the orifice is clearly affected by expansion wave movement within the cavity, which is a transient phenomenon not modeled in the one-dimensional analytical study. Thus, the dimensionless discharge time is not well predicted by the one-dimensional analytical solution.

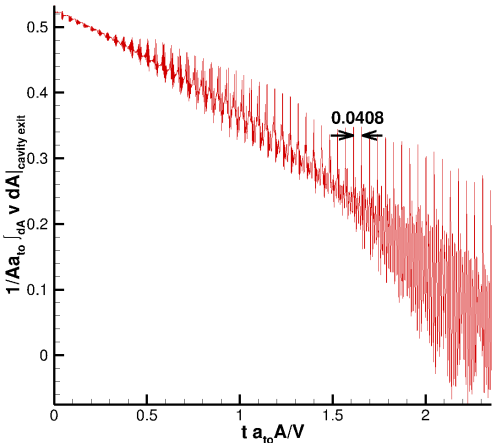

Figure 5.6: Velocity Integrated Over Cavity Exit Versus Time

5.1.3 Flow Contours

Flow contours and parameter graphs are shown throughout the discharge cycle in Figures 5.7-5.11. The dimensionless time between contour plots is $\Theta = \frac{t_f}{10}\frac{a_{to}A}{V}$, where t_f is the total calculation time, a_{to} is the initial speed of sound in the cavity, A is the area of the orifice and V is the volume of the cavity. The images are generated with a different grid than the impulse calculations for visualization purposes. The far boundary in the impulse calculations is significantly farther from the cavity exit plane. The initial condition is set to simulate an instantaneous energy deposition pulse at time zero of $\epsilon = 8.5$. A shock wave moves from the cavity exit to the low pressure region (into the ambient fluid), and an expansion fan moves toward the high pressure direction (into the cavity). This is similar to a Riemann shock tube [50]. The contact surface can be seen as a jump in temperature following the blast wave (Figure 5.7). The streamlines outside of the throat continue to converge toward the centerline of the throat. Thus, an aerodynamic throat is formed above the cavity exit. This is labeled in the parameter curve of Figure 5.7 as the virtual throat.

At 3Θ into the transient (Figure 5.8), the expansion fan and blast wave have moved further into the high pressure and low pressure sides, respectively. The contact surface follows the blast wave above the cavity exit plane. The aerodynamic throat is more apparent in the instantaneous streamlines. The flow at the edge of the cavity exit accelerates to accommodate a turn in flow direction, and thus the Mach number near the exit edge is

much higher than the centerline Mach number. The aerodynamic throat has moved farther above the cavity exit.

At 4Θ, Figure 5.9, a vortex ring forms around the edge of the cavity exit plane. This is typical of nozzle flows because the velocity discontinuity between the jet and the quiescent air generates circulation at the edge of the jet.

At 6Θ, Figure 5.10, the height of the center of the vortex ring has increased. The instantaneous streamline plot shows a converging section until the virtual throat, then a diverging section, where the flow continues to accelerate. Thus the streamlines act as an aerodynamic nozzle above the exit of the physically converging nozzle. The pressure in the diverging section of the aerodynamic nozzle decreases to below the pressure behind the contact surface. Thus, a barrel shock forms. The barrel shock is obvious in the Mach number contour graph (Figure 5.10c).

At 9Θ, Figure 5.11, the vortex ring has moved away from the jet exit. The vortex ring has expanded about its center, and ceases to provide an aerodynamic throat for the jet flow. The jet exit is the throat, above which the flow expands and accelerates. The maximum Mach number occurs just prior to the barrel shock, which trails the contact surface and blast wave. The blast wave has reflected off the far boundary.

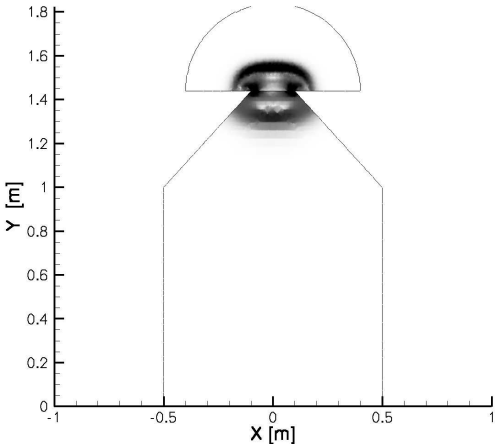

(a) Pressure Gradient Magnitude

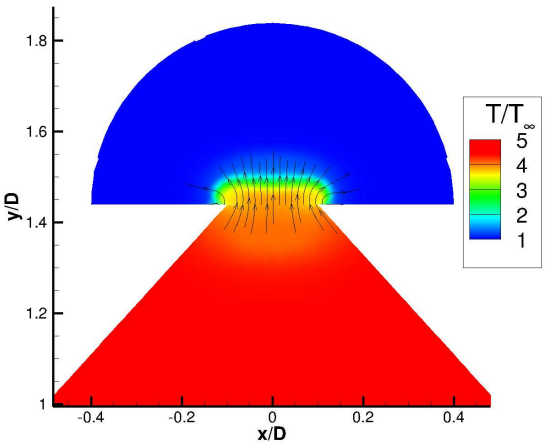

(b) Temperature Contours and Instantaneous Streamlines

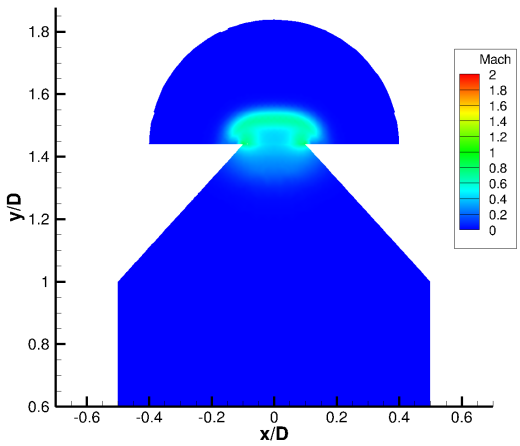

(c) Mach Number Contours

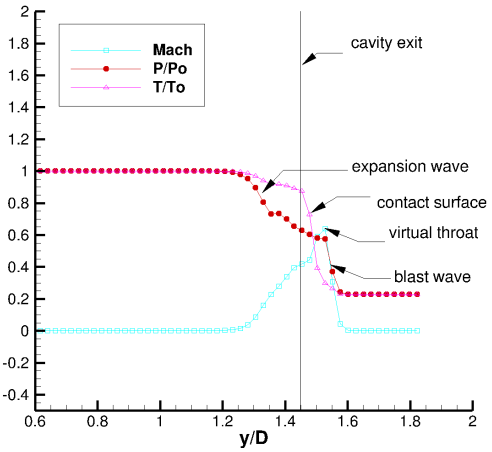

(d) Parameter Graph ($\frac{x}{D} = 0$)

Figure 5.7: SparkJet in Quiescent Environment Flow Contours at time = 2Θ

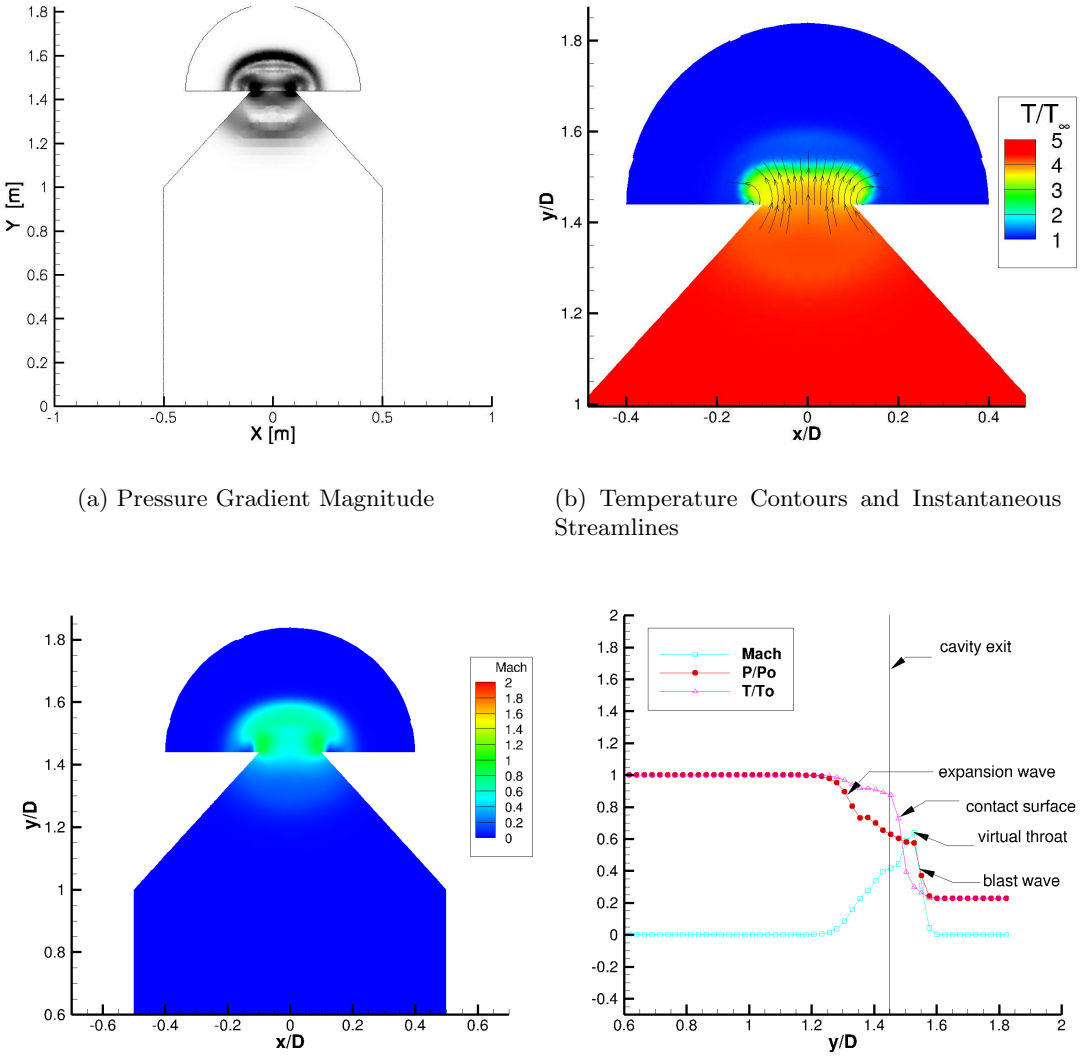

(a) Pressure Gradient Magnitude

(b) Temperature Contours and Instantaneous Streamlines

(c) Mach Number Contours

(d) Parameter Graph ($\frac{x}{D} = 0$)

Figure 5.8: SparkJet in Quiescent Environment Flow Contours at time = 2Θ

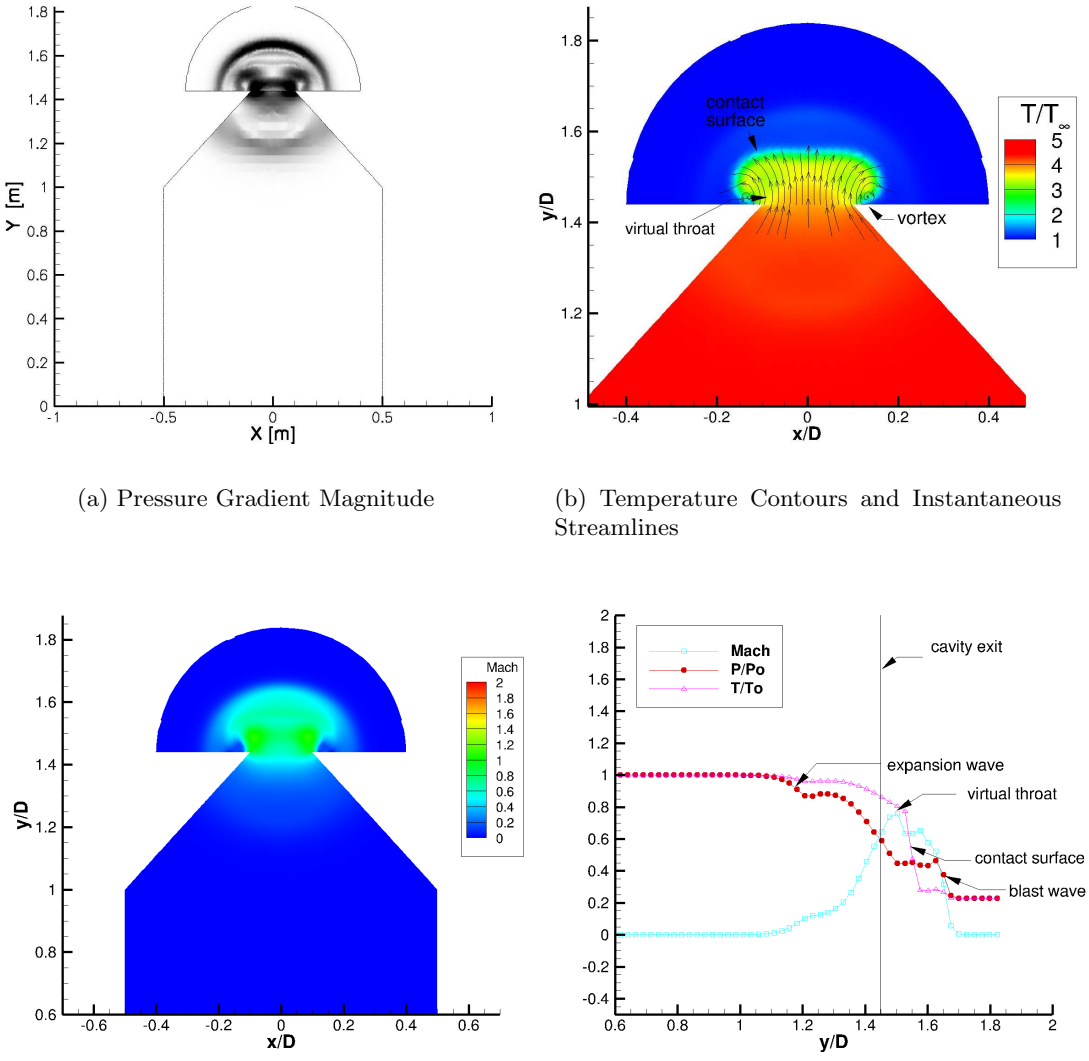

(a) Pressure Gradient Magnitude

(b) Temperature Contours and Instantaneous Streamlines

(c) Mach Number Contours

(d) Parameter Graph ($\frac{x}{D} = 0$)

Figure 5.9: SparkJet in Quiescent Environment Flow Contours at time = 4Θ

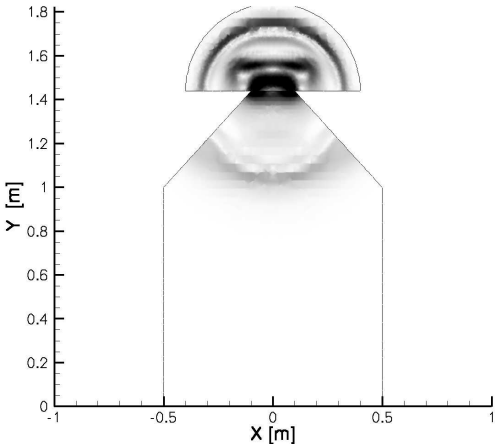

(a) Pressure Gradient Magnitude

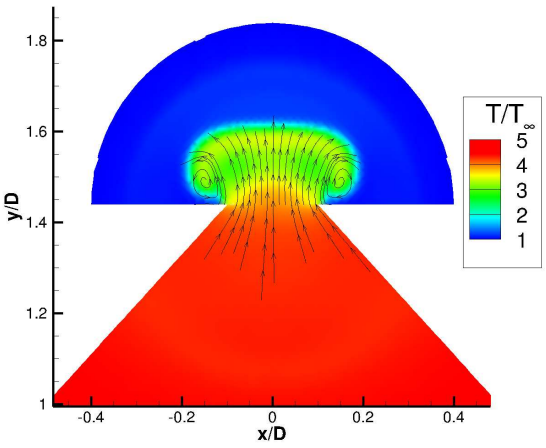

(b) Temperature Contours and Instantaneous Streamlines

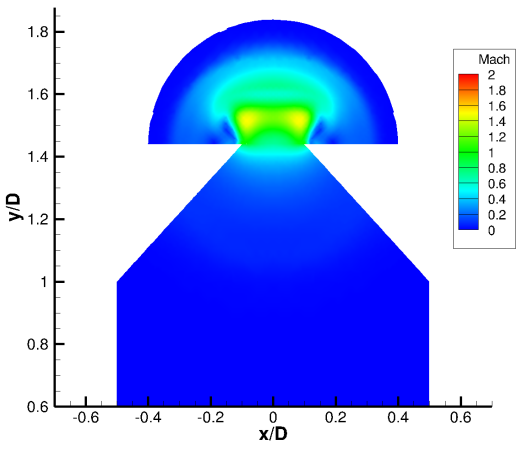

(c) Mach Number Contours

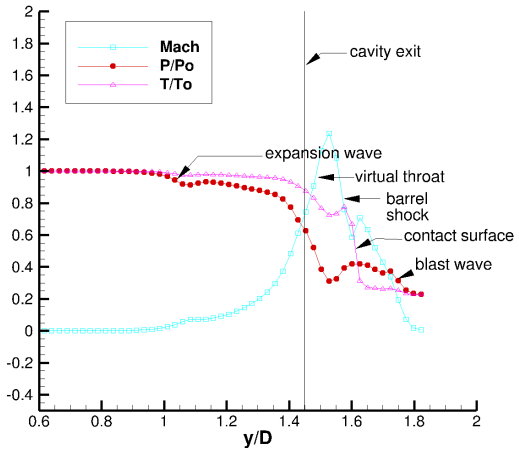

(d) Parameter Graph ($\frac{x}{D} = 0$)

Figure 5.10: SparkJet in Quiescent Environment Flow Contours at time = 6Θ

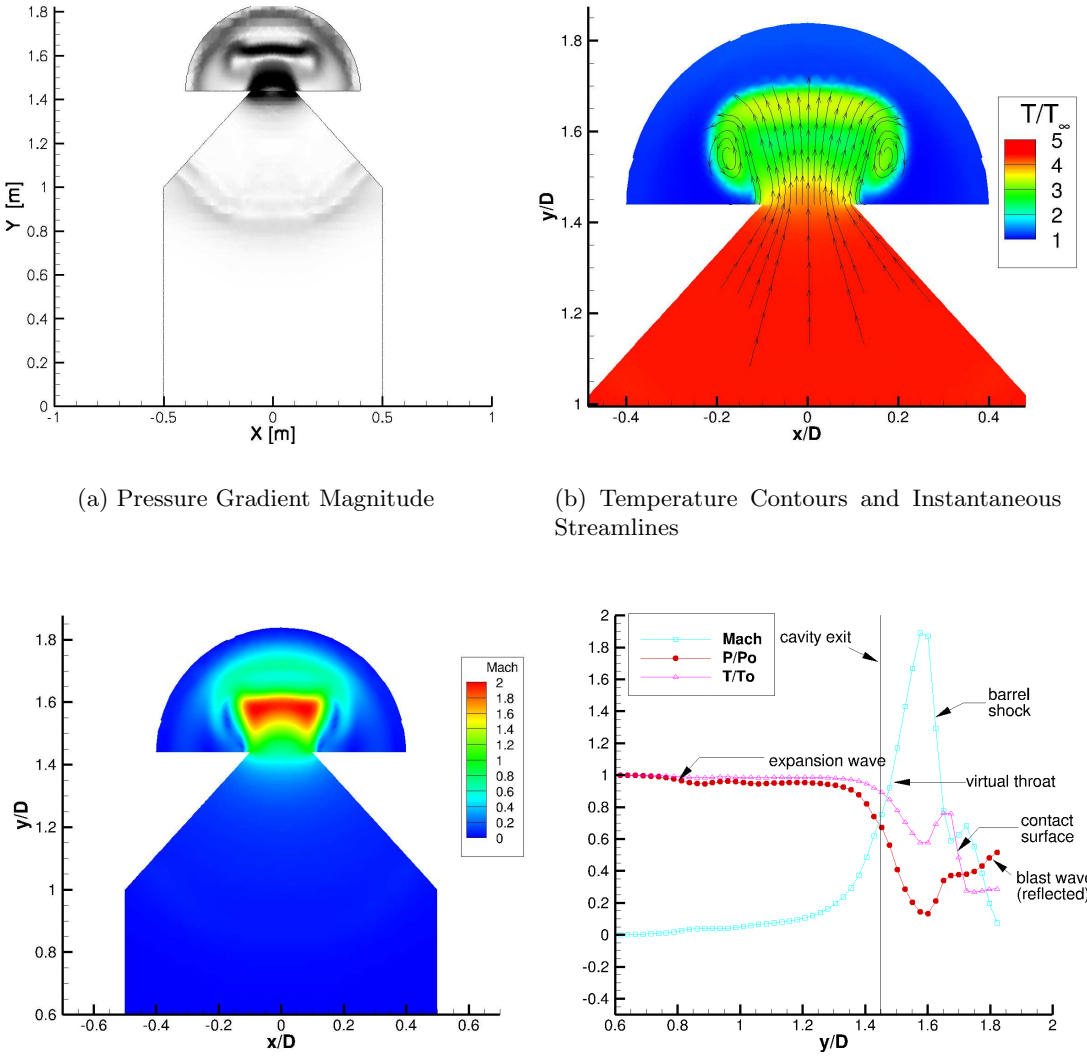

(a) Pressure Gradient Magnitude

(b) Temperature Contours and Instantaneous Streamlines

(c) Mach Number Contours

(d) Parameter Graph ($\frac{x}{D} = 0$)

Figure 5.11: SparkJet in Quiescent Environment Flow Contours at time = 9Θ

5.2 Comparison to Illinois SparkJet Experiments

The experimental conditions shown in Table 2.3 were replicated with a computational study. In comparing the computations with the experiments there are two significant unknowns that must be addressed.

1. the heating efficiency of the energy deposition
2. the shape and position of the arc discharge

To address the first unknown, three values of heating energy deposited were computed in the CFD calculations. The values were chosen to represent ten, fifteen and twenty percent heating efficiency of the mid-size capacitor which deposited 330 mJ.

The second unknown was addressed by assuming uniformly distributed energy deposition in the computations and creating a phase lag when comparing with the experiments. The phase lag represents the time it takes for the heated and pressurized air to move from the arc location to the orifice.

For a quantitative comparison between experiments and computations, the time varying velocity magnitude at selected points in the flow field is compared between experiments and computations. The phase lag mentioned in the preceding paragraph was chosen by matching the location of the barrel shock between the $Q = 4\ J$ experiment and the $Q = 33$ mJ computation. The points selected for comparison are shown on the velocity field from the 330 mJ experiment at 30 μs in Figure 5.12. The comparison of time varying velocity magnitudes at points 1 and 2 are shown in Figures 5.13(a) and 5.13(b), respectively. The closest match is between the highest energy deposited in the experiments, 4000 mJ and the lowest heating energy CFD case, 33 mJ. That is, an assumption of 0.8% heating efficiency is the closest match.

The heating efficiency, η, in the experiments can roughly be approximated by assuming the highest velocity in the flow near the cavity exit corresponds to the sonic velocity, and backtracking the temperature within the cavity, which can give us an idea of the heating energy deposited. With the help of Equation (3.5), we know

$$\eta = \frac{Q}{Q_{in}} = \frac{p_\infty V}{Q_{in}\,(\gamma - 1)} \left(\frac{a_{to}^2}{a_\infty^2} - 1 \right) \tag{5.4}$$

In the highest capacitance case, the maximum velocity near the throat is 350 m/s. This translates to a 0.1% heating efficiency. Previous studies indicate heating velocities may be higher. Johns Hopkins APL measured between 10% and 30% heating efficiency within their SparkJet (higher heating efficiency for lower input energy to internal energy ratio) [4]. This was acheived with a maximum sustained electrode spacing of 1.7 mm. An increase to 1.8 mm electrode spacing lead to a 35% heating efficiency, but multiple sparking was not possible. UTA performed spectroscopy to determine electron and ion temperatures in plasma created in their cavity [5]. Spectroscopy revealed a 10% heating efficiency. However, measured velocity of the discharge fell 60% short of predicted discharge velocity with 10% heating efficiency. The low efficiency calculated for the University of Illinois experiments is the subject of continuing investigation.

A comparison between the velocity fields of the experiments with $Q = 4000\ mJ$ and the computation of $Q = 33\ mJ$ are shown in Figures 5.14 through 5.17. At $t = 30\ \mu s$, the velocity profiles look very similar. At $t = 40\ \mu s$, the structure remains the same, though the velocity magnitude of the experiments have decreased, this corresponds to a valley in an oscillation seen in Figure 5.13(a) (the second point). By $t = 50\ \mu s$, the structure of the experiments is largely different than the computations. The jet flow in the experiments seems to be turbulent in the velocity magnitude contour from PIV at $t = 50\ \mu s$. The Reynolds number of the jet is $2 \cdot 10^4$, which is at the high end of the transition to turbulent mixing range identified in previous studies of turbulent jets [57]. Turbulent mixing prohibits the cellular structure seen in the computations. The computations assume a laminar flow, and the smallest eddies are not resolved with the computational grid, so the mixing behavior does not develop. The velocity magnitudes, however, remain similar throughout the remainder of the flow.

The experiments at $Q = 330\ mJ$ does not transition to turbulence, thus, to compare the structure of the jet flow, a comparison between the experiments with 330 mJ deposited and the computations with 33 mJ heating energy added is shown in Figures 5.18 through 5.21. The time lag is again estimated by matching the location of the barrel in the first image. Both the computations and the experiments show cellular structure, as would be expected in an underexpanded jet flow [58]. However, a phase difference between the two

cases occurs. This is because the energy deposited is different between the two cases, thus the speed at which each successive shock system travels into the flow is different.

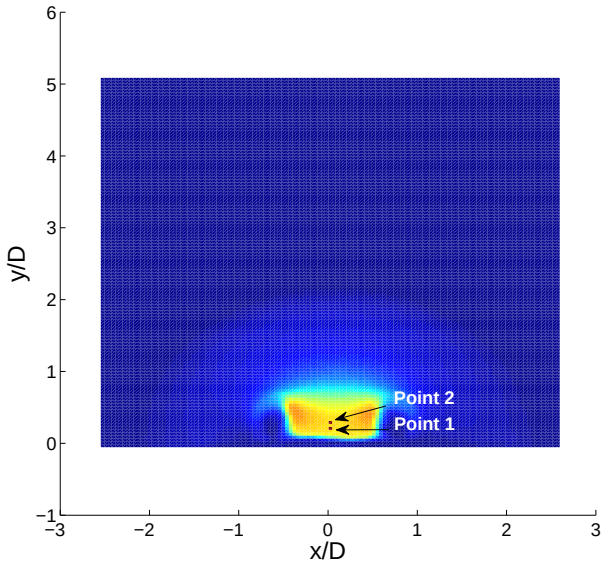

Figure 5.12: Locations of Velocity Magnitude Comparison

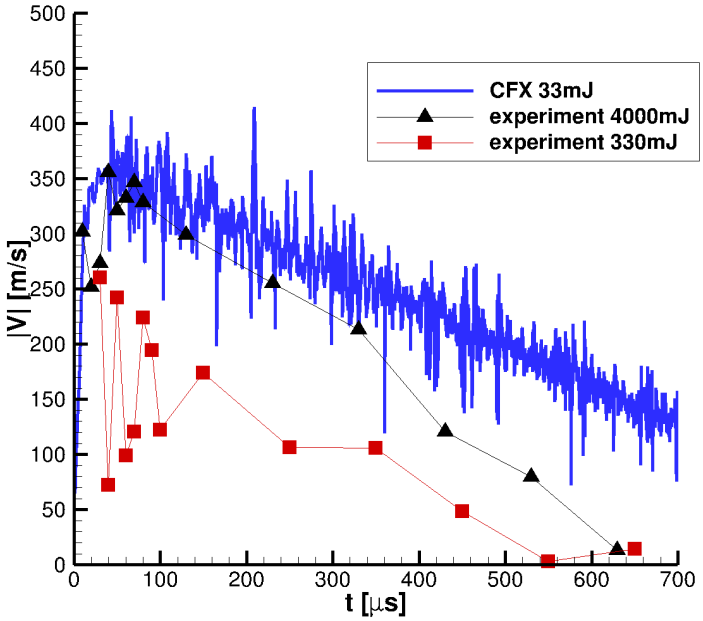

(a) Point 1

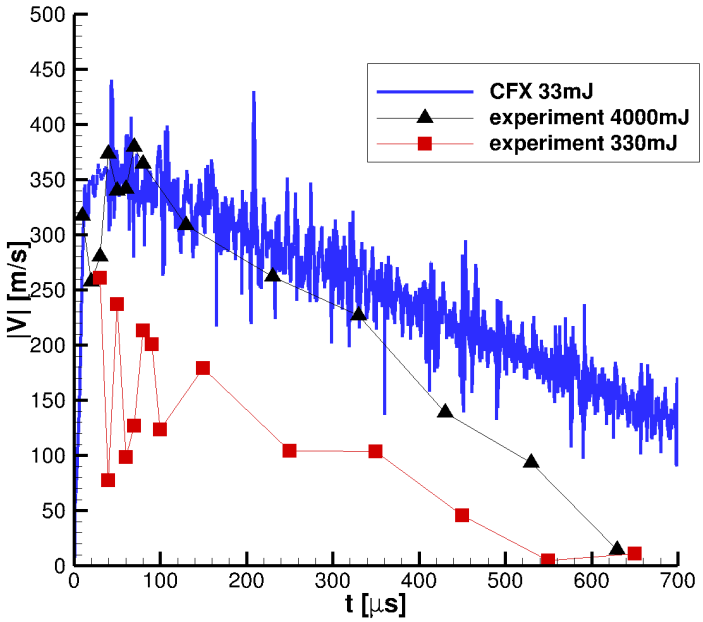

(b) Point 2

Figure 5.13: Velocity Magnitude Vrs. Time at Selected Point in Flow Field

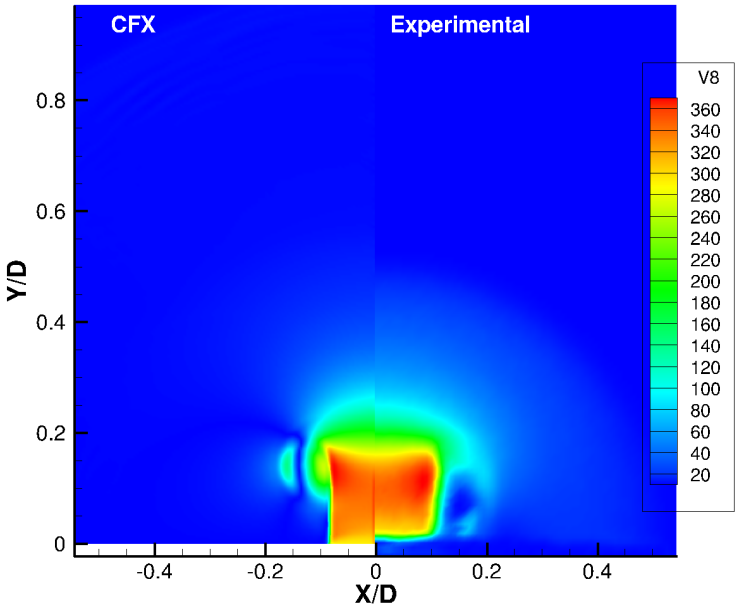

(a) t = 30 μs

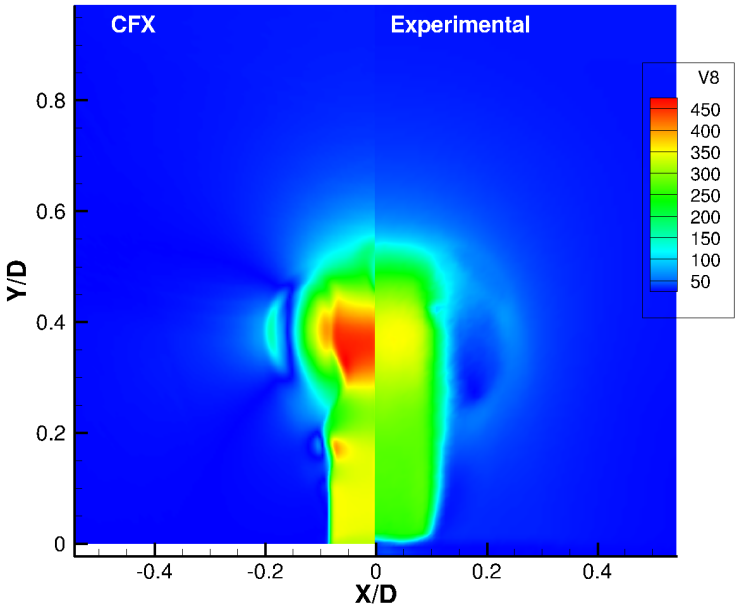

(b) t = 40 μs

Figure 5.14: Velocity Magnitude Contours of 4000 mJ Experiment and 33 mJ (0.8% heating efficiency) Computation

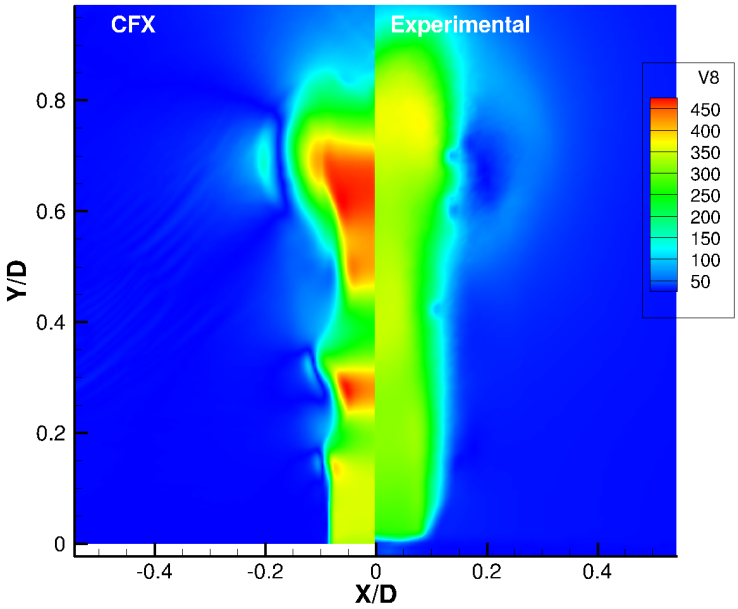

(a) t = 50 μs

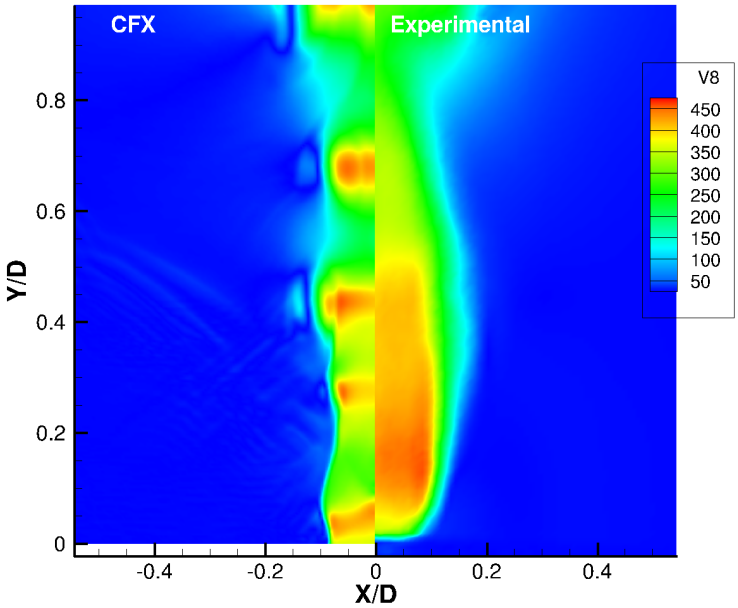

(b) t = 60 μs

Figure 5.15: Velocity Magnitude Contours of 330 mJ Experiment and 33 mJ (0.8% heating efficiency) Computation

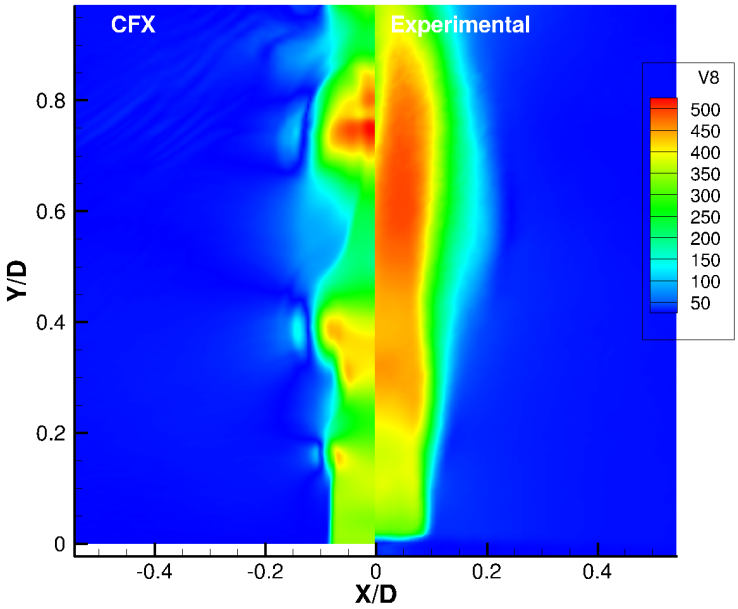

(a) t = 70 μs

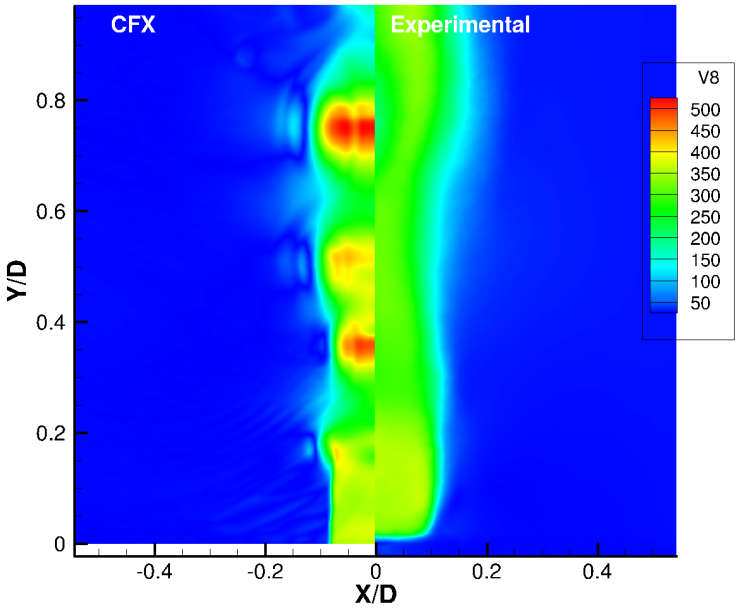

(b) t = 80 μs

Figure 5.16: Velocity Magnitude Contours of 4000 mJ Experiment and 33 mJ (0.8% heating efficiency) Computation

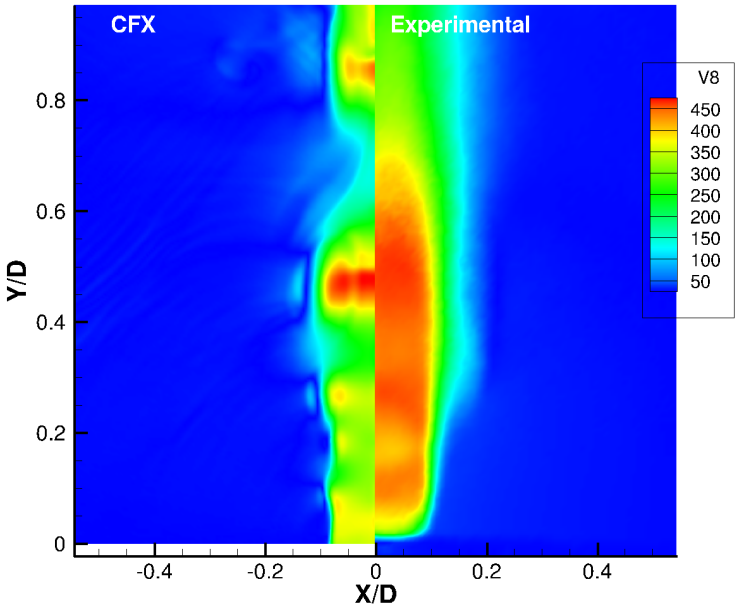

(a) t = 90 μs

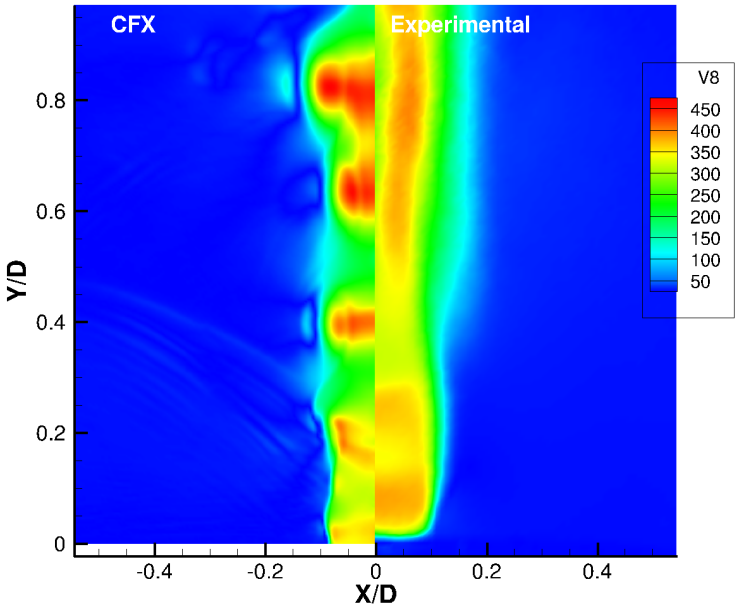

(b) t = 100 μs

Figure 5.17: Velocity Magnitude Contours of 4000 mJ Experiment and 33 mJ (0.8% heating efficiency) Computation

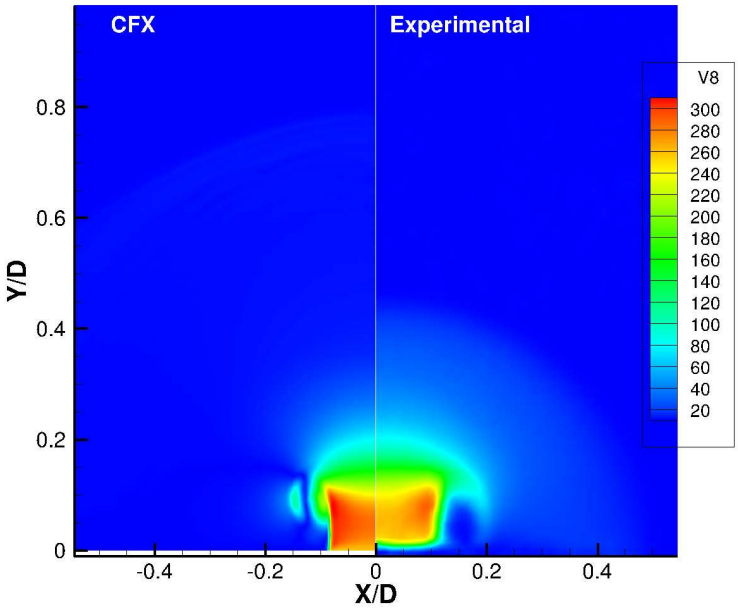

(a) t = 30 μs

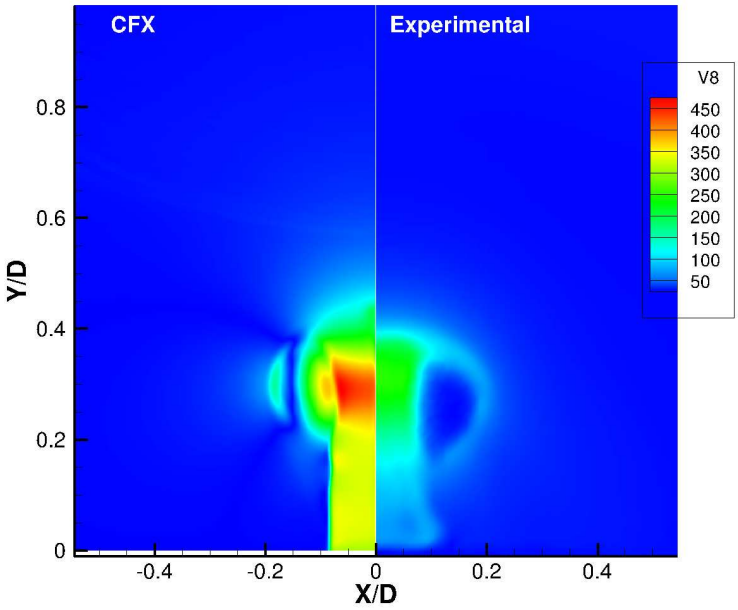

(b) t = 40 μs

Figure 5.18: Velocity Magnitude Contours of 330 mJ Experiment and 33 mJ (10% heating efficiency) Computation

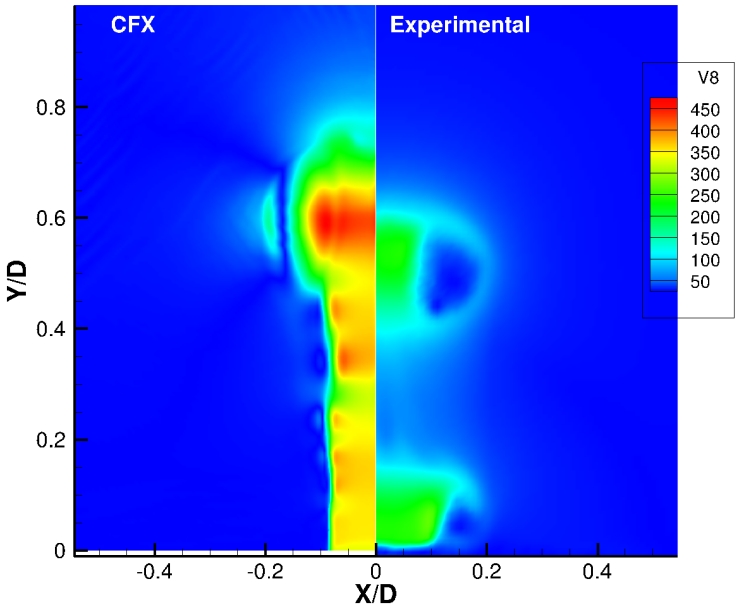

(a) t = 50 μs

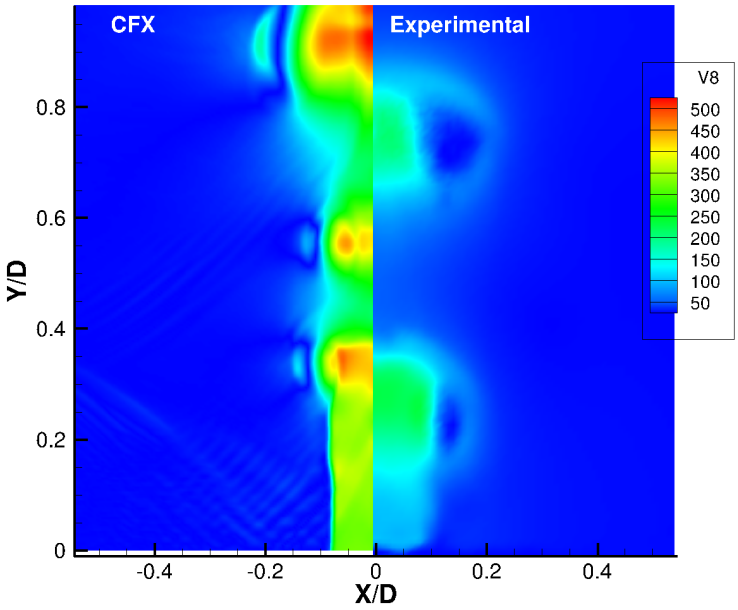

(b) t = 60 μs

Figure 5.19: Velocity Magnitude Contours of 330 mJ Experiment and 33 mJ (10% heating efficiency) Computation

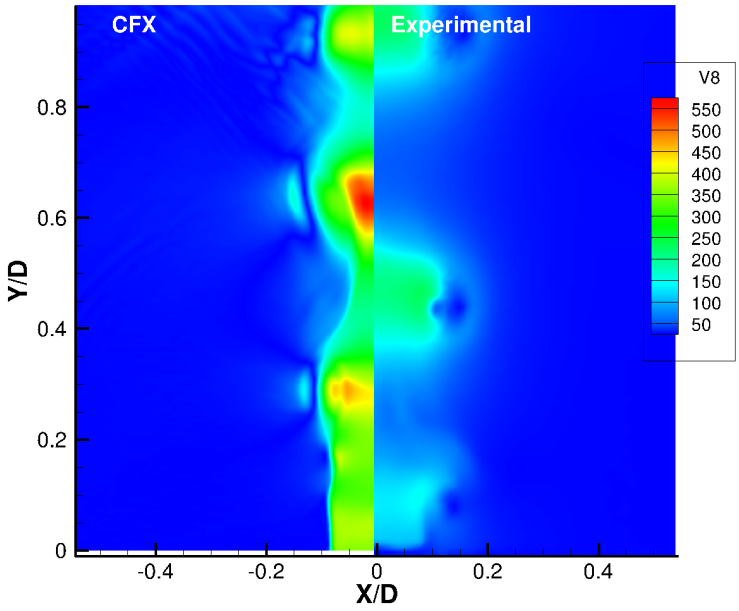

(a) t = 70 μs

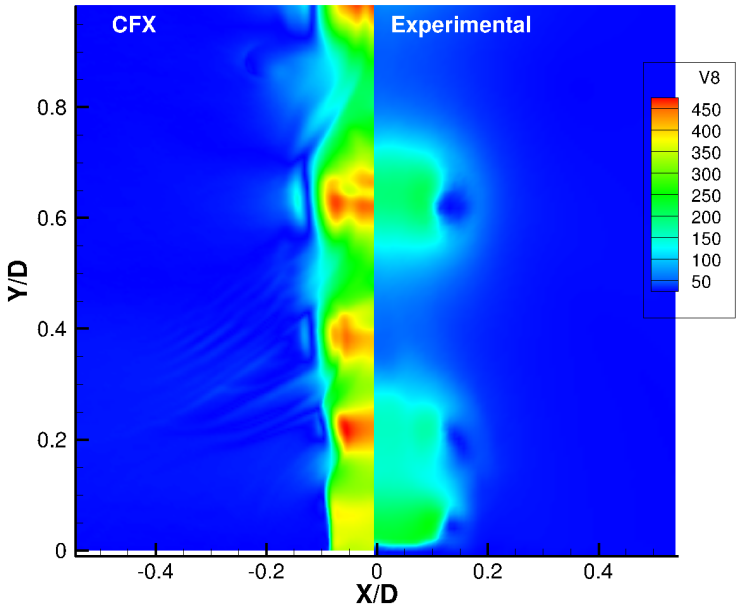

(b) t = 80 μs

Figure 5.20: Velocity Magnitude Contours of 330 mJ Experiment and 33 mJ (10% heating efficiency) Computation

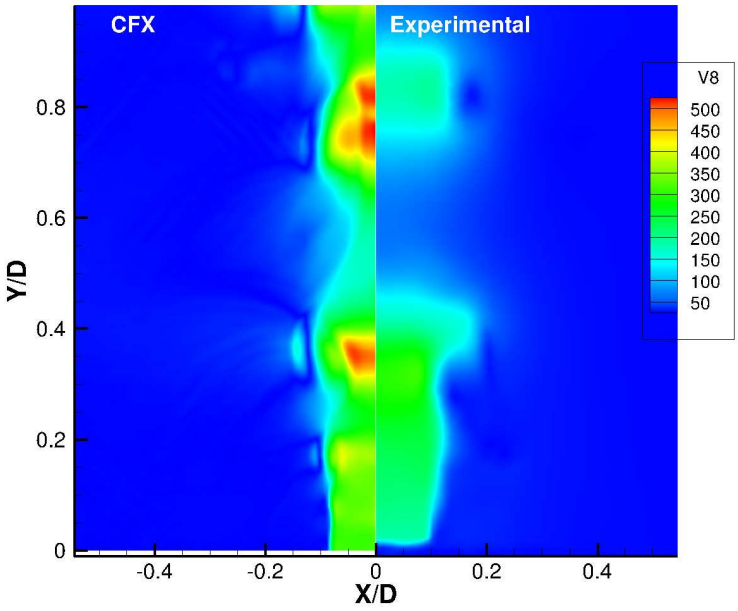

(a) t = 90 μs

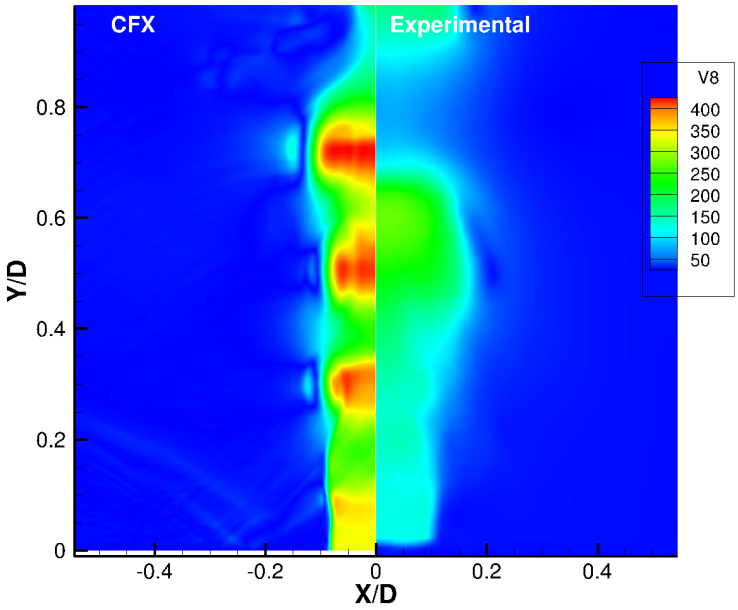

(b) t = 100 μs

Figure 5.21: Velocity Magnitude Contours of 330 mJ Experiment and 33 mJ (10% heating efficiency) Computation

5.3 Single Pulse into Cross Flow

In evaluating the SparkJet in a turbulent supersonic cross flow, three new dimensionless parameters (Table 2.2) are introduced to the problem (1) Mach number of the cross flow, (2) Reynolds number and (3) the relative size of cavity exit diameter to the boundary layer height. The relative size of the cavity exit diameter to the boundary layer height is studied as a first step in characterizing the SparkJet. Two values are chosen, $d/\delta = 1$ and 5.

5.3.1 Steady State

The steady state Mach 3 turbulent boundary layer flow over an adiabatic flat plate is the initial condition of the time-accurate computation of the SparkJet pulse into the cross flow.

To verify that the flow had sufficiently converged to a steady state, the boundary layer velocity profile and skin friction along the plate were compare to theoretical values. Profiles of velocity and skin friction are presented in Section 4.3.5.

5.3.2 Impulse

The dimensionless impulse as a function of dimensionless time is shown in Figure 5.22(a). The two relative cavity exit diameter sizes and the quiescent air case are shown. The dimensionless impulse is significantly larger in the cross flow case than the SparkJet issuing into quiescent air. This is due to significantly longer discharge times of a jet issuing into a cross flow case than a jet issuing into a quiescent environment. The dimensionless integrand is graphed versus dimensionless time in Figure 5.22(b). The quiescent air case achieves a higher velocity at the cavity orifice than the cross flow cases, but the cross flow case total discharge time is longer and the pressure at the jet exit is higher than the quiescent case. Thus, the impulse is greater for the cross-flow cases. The cross flow cases show that the peak ϑ is relatively insensitive to d/δ.

In Figure 5.23, the dimensionless impulse and mass fraction at the end of the discharge cycle are graphed against jet diameter to boundary layer height. In these figures the quiescent case is shown as $d/\delta = 0$, as the quiescent case is equivalent to a cavity in cross flow with an infinitely large boundary layer. The dimensionless impulse and mass fraction show

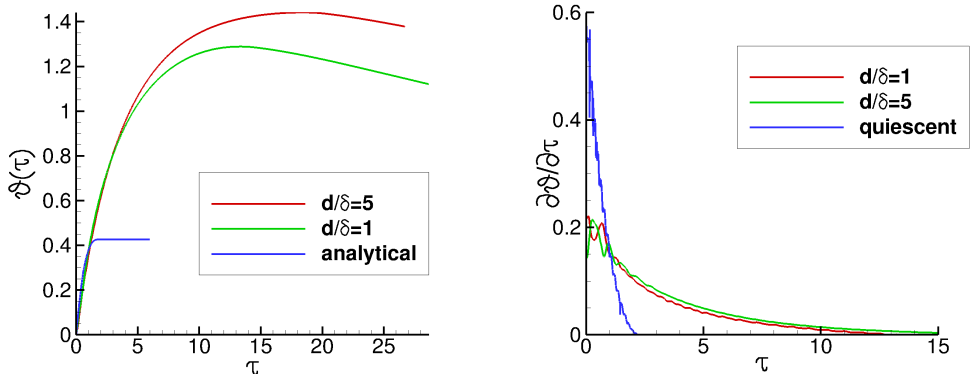

(a) Dimensionless Impulse

(b) Mass Fraction After Discharge

Figure 5.22: SparkJet in Cross-Flow

asymptotic behavior, where the both remain relatively constant with respect to d/δ for $d/\delta > 1$. The presence of the cross flow increases the dimensionless impulse, and decreases the mass left in the cavity after discharge. The cross-flow entrains more air from the cavity, leaving less mass behind. After the cavity has discharged, the cavity is similar to the driven cavity problem, where a low velocity circulation flow exists within the cavity, though no flow is being drawn in to refresh the cavity.

5.3.3 Flow Visualizations

Flow contours and visualizations are shown for $d/\delta = 1$ and 5. The dimensionless times at which the visualizations are shown are graphed on the dimensionless impulse integrand plot in Figure 5.24.

Figures 5.25 and 5.26 illustrate the dimensionless pressure contours for $d/\delta = 1$ and $d/\delta = 5$, respectively. At the beginning of the jet flow (Figures 5.25a and 5.26a) a sharp jump in pressure occurs upstream of the SparkJet and a normal shock is seen. This occurs within the boundary layer in the $d/\delta = 1$ case and extends outside of the boundary layer for $d/\delta = 5$. The boundary layer height is labeled in Figures 5.25a and 5.26a. As time progresses and the jet exhausts, the normal shock gives way to an oblique shock upstream of the jet and an expansion region downstream of the cavity orifice. These features are labeled, along with the sonic line, in Figures 5.25b and 5.26b. The structure of the jet

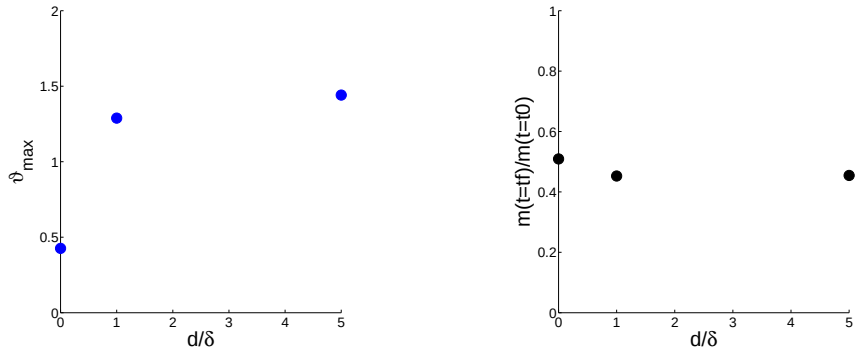

(a) Dimensionless Impulse

(b) Dimensionless Impulse Integrand

Figure 5.23: Dimensionless Impulse for SparkJet in Cross-Flow

exhaust is qualitatively similar for the remainder of the jet exhaust.

The Mach number contours and instantaneous streamlines are shown in Figures 5.27 and 5.28 for jet diameters one and five times the boundary layer height, respectively. At the initial disturbance caused by the jet flow, Figures 5.27a and 5.28a, the cross flow encounters a normal shock upstream of the jet and is steeply deflected above the jet, behind the normal shock. After the initial transient (Figures 5.27b-d and 5.28b-d), the flow structure remains relatively unchanged. The jet flow takes a sharp turn after exiting the cavity creating an oblique shock upstream and expansion fan downstream. The location where the sonic line intersects the streamlines from the cavity gives a rough estimation of the diameter of the aerodynamic throat area of the cavity. The diameter of the aerodynamic throat is an order of magnitude smaller than the diameter of the cavity orifice. The constricted exit area reduces the mass flow rate out of the cavity and creates longer jet exhaust durations. Thus, the effect of the cross flow is a sharp deflection of the jet flow, which reduces the mass flow rate of cavity exhaust and increases the discharge time of the cavity. As seen in the graph of the dimensionless impulse integrand (Figure 5.22), the longer discharge times create higher impulses than the jet exiting into quiescent air, despite lower velocity magnitude at the

throat.

The instantaneous surface streamlines are shown on the surface surrounding the jet exit plane from a top view perspective for $d/\delta = 1$ in Figure 5.29. At the beginning of the jet flow, Figure 5.29a shows a separation line upstream of the jet, which originates from a saddle point (S1) at the centerline. A nodal point (N1) indicates a stagnation point on the wall upstream of the jet. A saddle point (S2) appears downstream of the jet that separates the flow pulled upstream by the jet flow and flow entrained downstream by the wake of the jet. At $3/100\tau_f$ (Figure 5.29b), a nodal point appears between the jet and the S2 saddle point. The nodal point N2 marks another divider. Downstream of N2, the flow entrained in the jet is pulled upstream before entrainment; upstream of N2 the flow direction is downstream only. After the initial transient, the surface streamline structure is qualitatively uniform in time, as seen in Figure 5.29c and d. The quasi-steady surface streamline structure consists of a separation line, attachment line, saddle points S1 and S2, and nodal point N1. The separation line indicates the intersection of the shock surface with the wall. The attachment line indicates a line where flow attaches to the wall.

The surface streamlines for the $d/\delta = 5$ case are shown in Figure 5.30. At the beginning of the jet flow, Figure 5.30a, flow begins to expand around the jet flow. A little later in the transient, Figure 5.30b, the saddle point which marks the center of the separation line (S1), the nodal point marking the stagnation point on the wall (N1) and the saddle point S2 have developed. Similar to the $d/\delta = 1$ case, the surface streamlines develop into a quasi-steady structure after the initial transient has passed, as seen in Figures 5.30c and d. The flow features at the quasi-steady state are similar to the $d/\delta = 1$ case.

In Figures 5.31 and 5.32, the surface streamlines of the quasi-steady state are shown alongside the Mach contours of the center plane. Volumetric instantaneous streamlines from the jet orifice are shown in black. At the center of the X-Z plane which intersects the jet, a nodal point, N3, is shown within the jet exit plane. The nodal point N3 marks the center of the jet; the surrounding fluid is entrained around this point. The nodal points and saddle points are summarized in Table 5.5. The separation line in the surface streamline structure is seen just below the intersection of the oblique shock with the boundary layer.

Finally, volumetric instantaneous streamribbons are shown in Figures 5.33 and 5.34.

Label	Title	Flow Description
S1	Saddle Point	Origination of Separation line
S2	Saddle Point	Separates Flow Entrained Upstream and Downstream by the SparkJet
N1	Nodal Point	Stagnation Point on Wall Upstream of Jet
N2	Nodal Point	Divider Between Flow Pulled Upstream by Jet and Flow Uniformly Directed Downstream
N3	Nodal Point	Center of Jet, Which Entrains Surrounding Fluid

Table 5.5: Surface Streamline Label Descriptions

The streamribbons show that the flow is rotated just downstream of the separation line; this is the horse-shoe vortex created by the jet. The rotated flow is directed toward the wall, the attachment line indicates where the flow connects with the boundary layer.

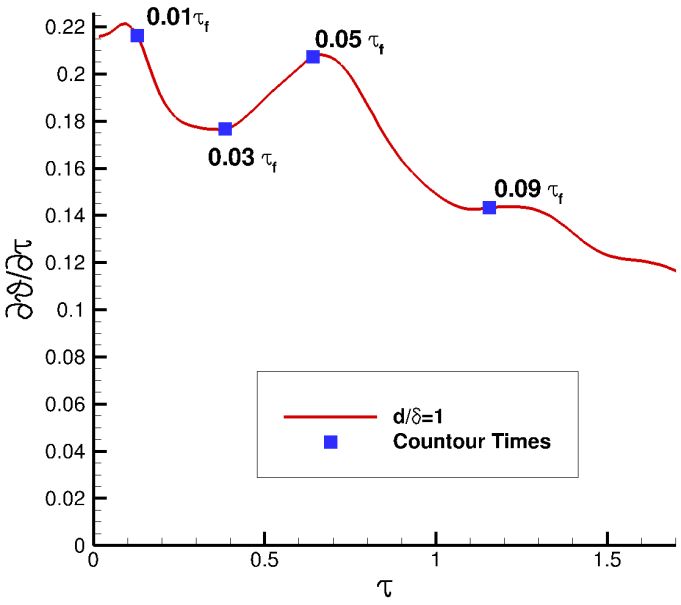

(a) $d/\delta = 1$

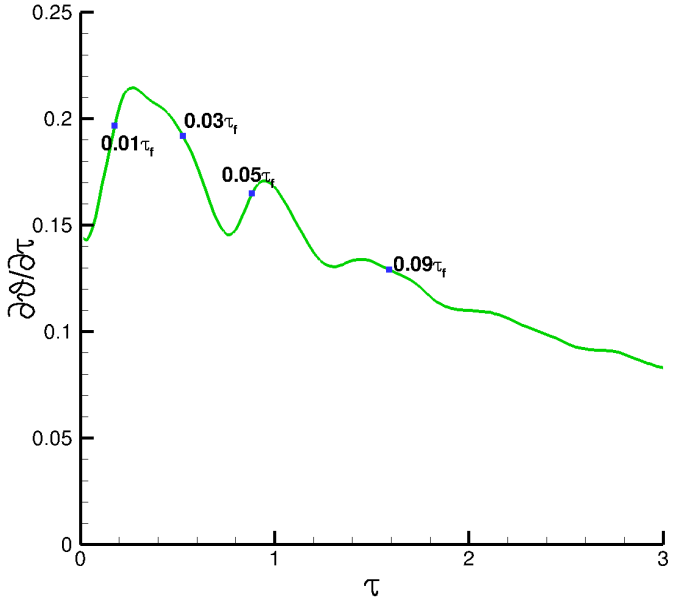

(b) $d/\delta = 5$

Figure 5.24: Dimensionless Times of Contour Plots

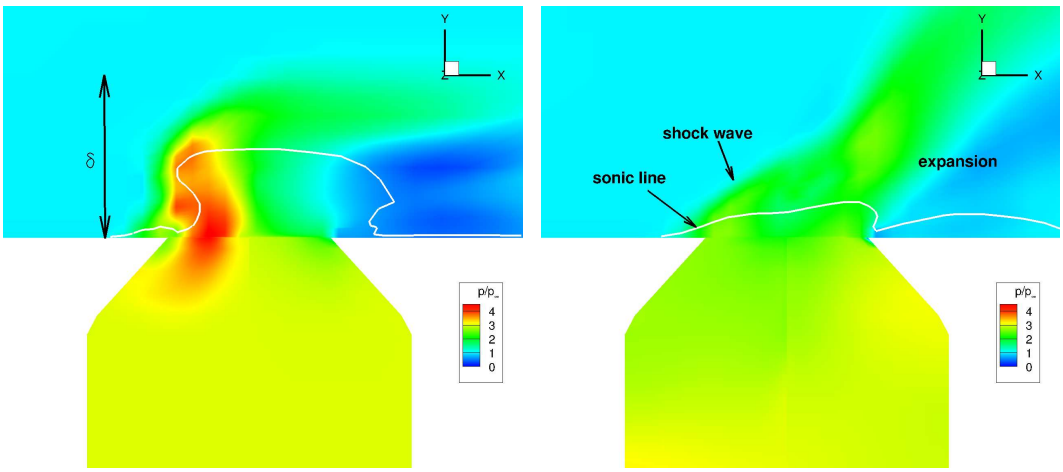

(a) $\tau = 1/100\tau_f$

(b) $\tau = 3/100\tau_f$

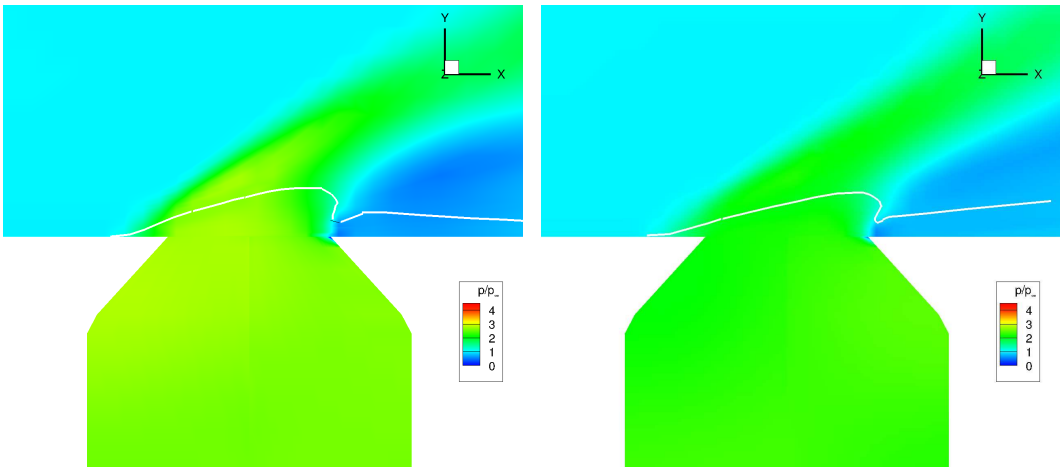

(c) $\tau = 5/100\tau_f$

(d) $\tau = 9/100\tau_f$

Figure 5.25: Pressure $d/\delta = 1$ (Sonic Line Shown in White)

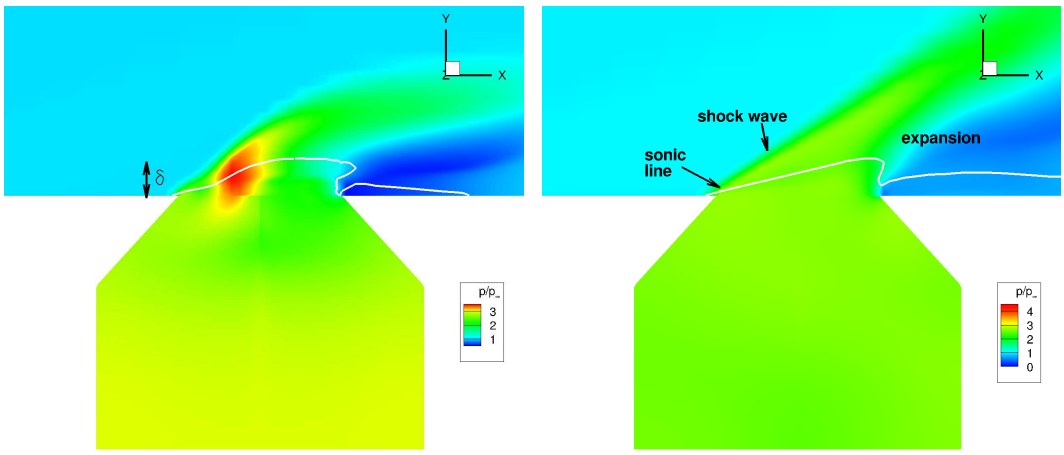

(a) $\tau = 1/100\tau_f$

(b) $\tau = 3/100\tau_f$

(c) $\tau = 5/100\tau_f$

(d) $\tau = 9/100\tau_f$

Figure 5.26: Pressure Contours $d/\delta = 5$

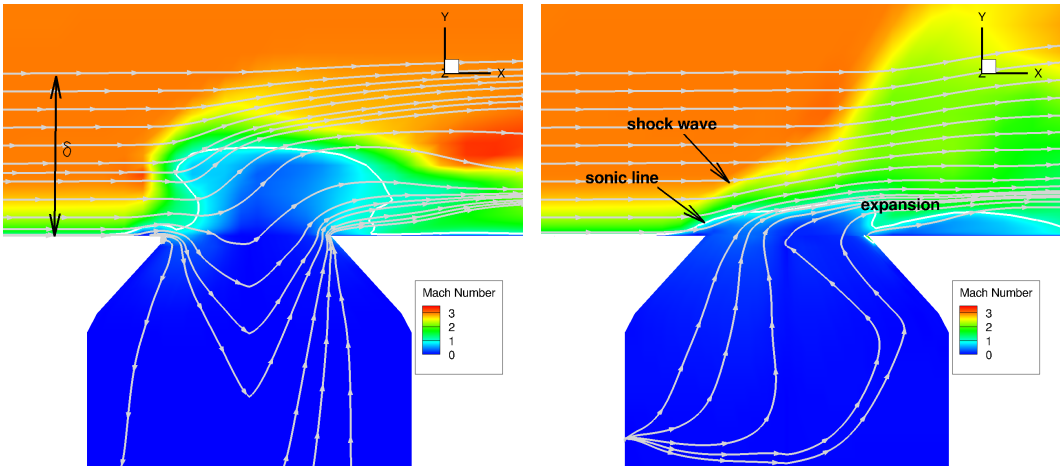

(a) $\tau = 1/100\tau_f$

(b) $\tau = 3/100\tau_f$

(c) $\tau = 5/100\tau_f$

(d) $\tau = 9/100\tau_f$

Figure 5.27: Mach Number and Instantaneous Streamlines $d/\delta = 1$ (Sonic Line Shown in White)

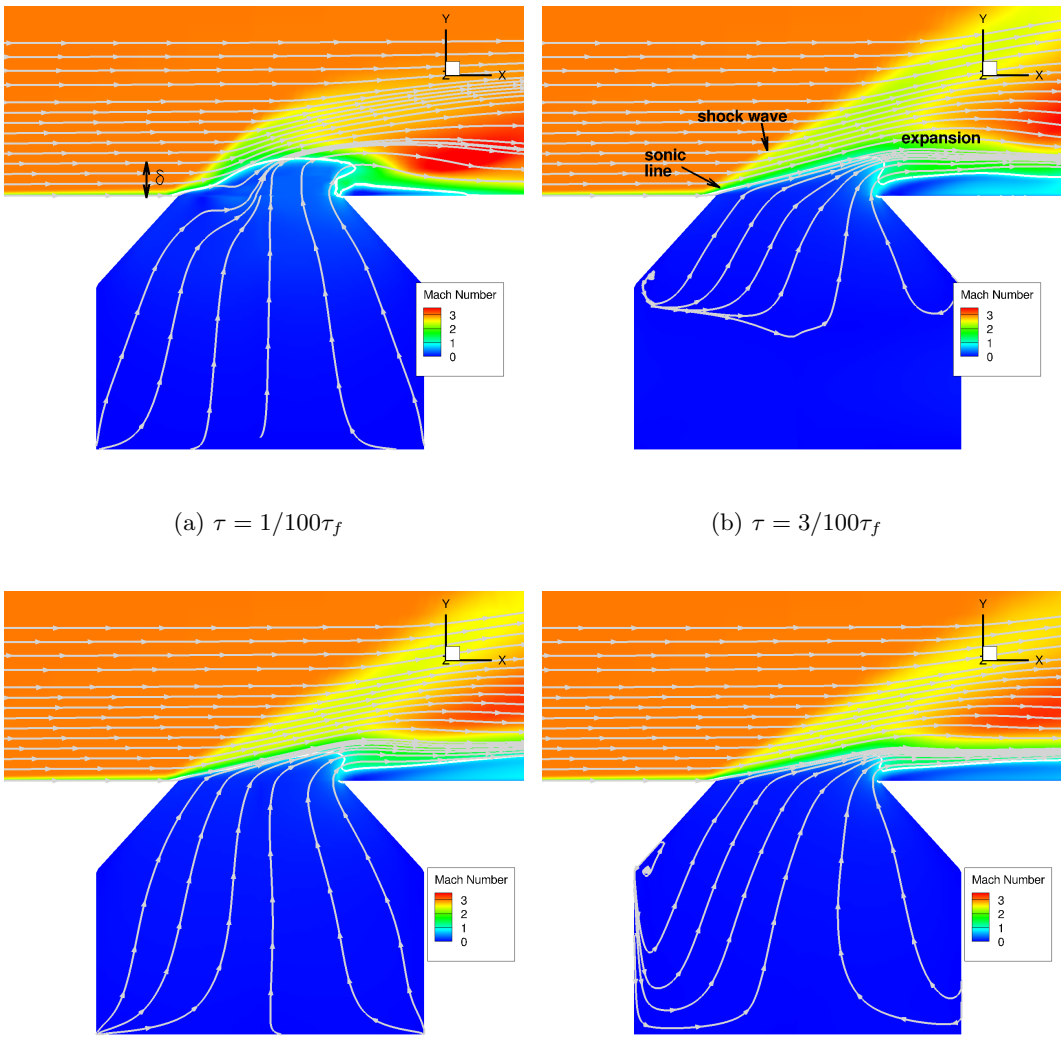

(a) $\tau = 1/100\tau_f$

(b) $\tau = 3/100\tau_f$

(c) $\tau = 5/100\tau_f$

(d) $\tau = 9/100\tau_f$

Figure 5.28: Mach Number Contours $d/\delta = 5$

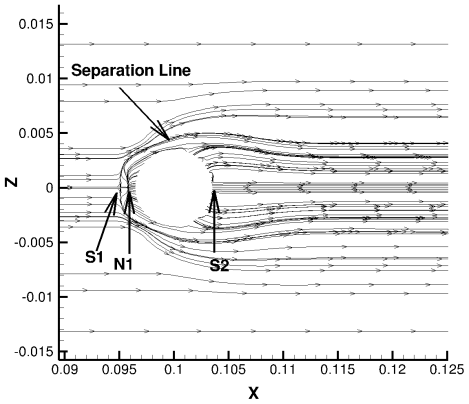

(a) $\tau = 1/100\tau_f$

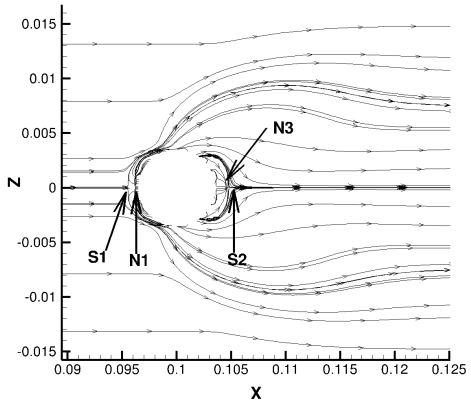

(b) $\tau = 3/100\tau_f$

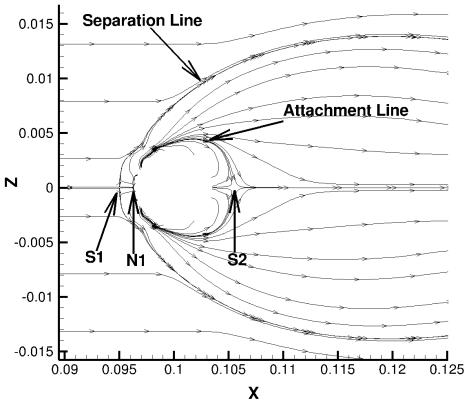

(c) $\tau = 5/100\tau_f$

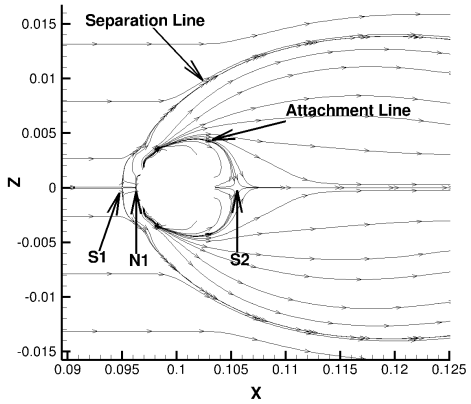

(d) $\tau = 9/100\tau_f$

Figure 5.29: Instantaneous Surface Streamlines $d/\delta = 1$

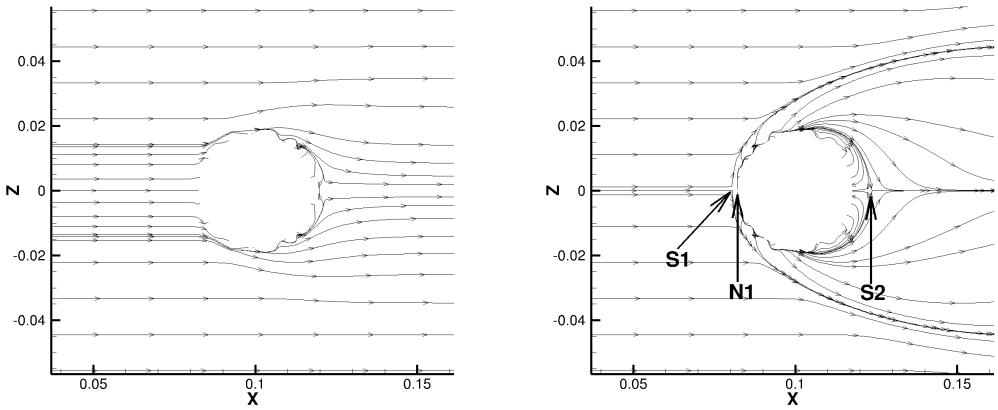

(a) $\tau = 1/100\tau_f$ (b) $\tau = 3/100\tau_f$

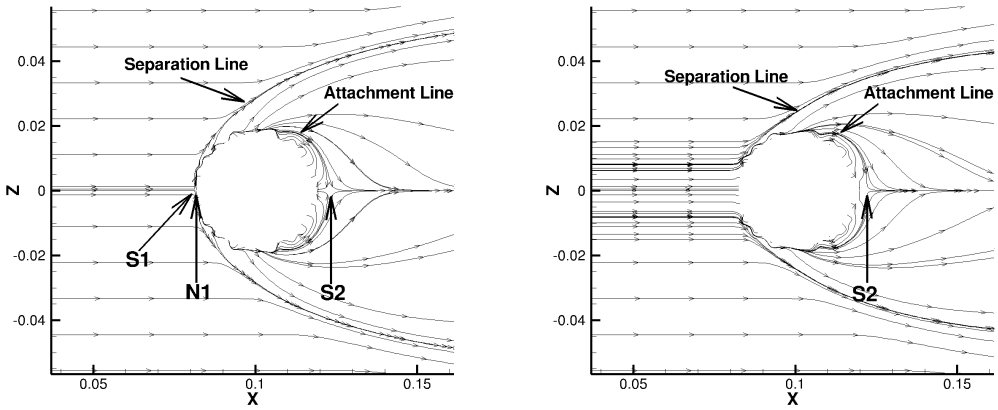

(c) $\tau = 5/100\tau_f$ (d) $\tau = 9/100\tau_f$

Figure 5.30: Instantaneous Surface Streamlines $d/\delta = 5$

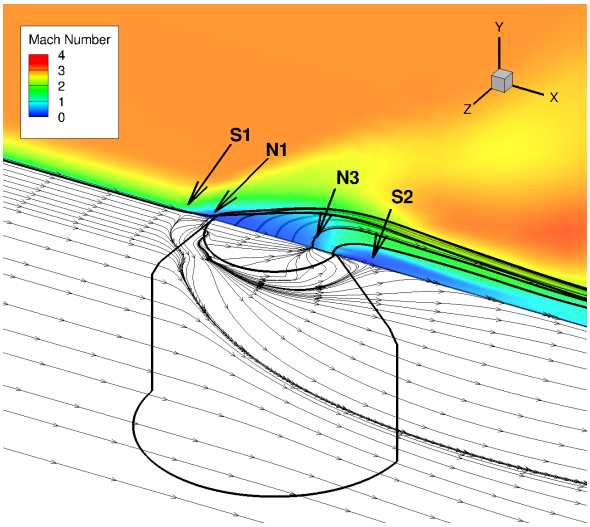

Figure 5.31: Image of Instantaneous Streamlines at $\tau = 0.05\tau_f$ $d/\delta = 1$

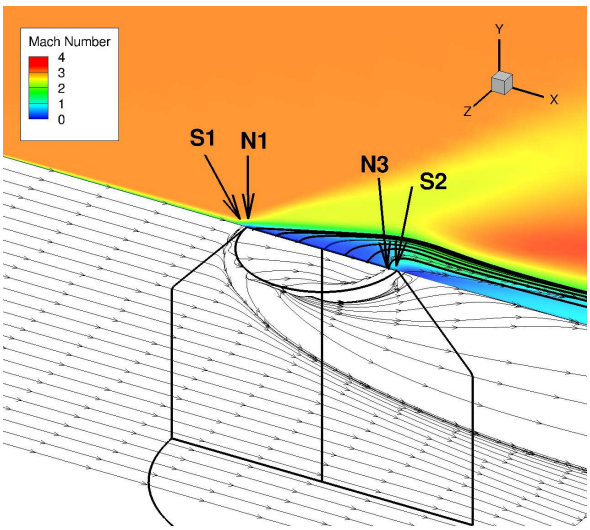

Figure 5.32: Image of Instantaneous Streamlines at $\tau = 0.05\tau_f$ $d/\delta = 5$

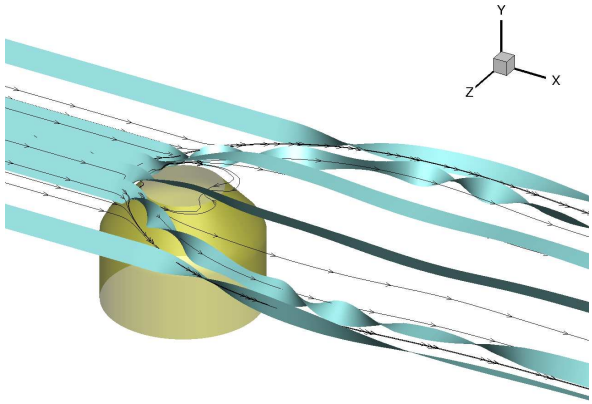

Figure 5.33: Instantaneous Stream Ribbons at $\tau = 0.05\tau_f$ $d/\delta = 1$

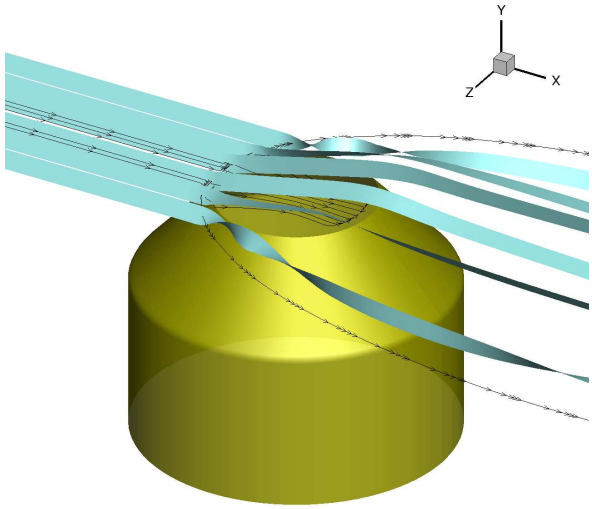

Figure 5.34: Instantaneous Stream Ribbons at $\tau = 0.05\tau_f$ $d/\delta = 5$

Chapter 6

Conclusions

An investigation of the single pulse of a SparkJet has been accomplished. A one-dimensional analytical study is in excellent agreement with a two-dimensional axisymmetric computational study in predicting both the dimensionless impulse and mass at the end of the discharge from the cavity. It is verified with a Monte-Carlo analysis that the dimensionless impulse is insensitive to the dimensionless cavity geometry parameters. Thus, the dimensionless impulse is solely a function of the dimensionless energy deposited to the cavity. The dimensionless discharge duration is, however, sensitive to geometry and, due to its highly transient nature, is not well predicted by the one-dimensional and quasi-steady analytical result. A comparison with experiments from University of Illinois of the SparkJet in a quiescent environment shows qualitatively similar flow structures for lower energy deposition values (where the jet flow remains laminar). However, further investigation is necessary to determine why the comparison seems to indicate very low heating efficiency of the Illinois SparkJet. The dimensionless impulse issuing into a turbulent supersonic cross flow was evaluated computationally. It was shown that the dimensionless impulse generated by the plasma jet into cross flow is significantly higher than the jet issuing into quiescent air. Additionally, the dimensionless impulse is only mildly sensitive to the relative size of the jet to the boundary layer for orifice diameters on the same order as the boundary layer height.

Chapter 7

Appendix

7.1 Dimensional Example

The preceding analysis has used dimensionless parameters which can be applied to many different dimensional scenarios. An example of applying this analysis to an experiment at atmospheric conditions is illustrated here, although the application of this model is not limited to atmospheric conditions. A generic cavity configuration is assumed which is similar in magnitude to published experiments. The cavity parameters and atmospheric conditions are given in Table 7.1.

The minimum energy for sonic flow at the cavity throat is calculated with Equation (4.5), for air

$$Q > 2.23 p_\infty V = 22.6 \text{ mJ} \tag{7.1}$$

Assuming 25% heating efficiency [59], the amount of discharge energy would have to be

$$\text{discharge energy} > \frac{22.6}{0.25} = 90.5 \text{ mJ} \tag{7.2}$$

To obtain $\epsilon = 5$, the energy required is $Q = 5 p_\infty V = 50.7$ mJ and, again assuming 25% heating efficiency, a discharge energy of 202.6 mJ is required. The impulse is calculated with Equations (4.1), (4.24) and (4.34).

Cavity Parameters	Ambient Air Conditions
volume=$1.0 \cdot 10^{-7}$ m^3	$p_\infty = 101325$ Pa
cavity diameter=1 cm	$T_\infty = 293$ K
orifice diameter=1 mm	
cavity height=1 cm	

Table 7.1: Example Cavity and Ambient Parameters

$$
\begin{aligned}
I \quad &= \sqrt{\rho_\infty V Q}\left\{\sqrt{\frac{8}{\gamma\left(\gamma+1\right)}\left(\frac{1}{\epsilon}+\left(\gamma-1\right)\right)}\left[1+\frac{\sigma}{\gamma-1}\frac{p_\infty}{p_{t_o}}-\frac{\gamma}{\gamma-1}\left(\frac{\sigma p_\infty}{p_{t_o}}\right)^{\frac{\gamma+1}{2\gamma}}\right]\right. \\
&+ \frac{5\sqrt{7}}{48}\left(\epsilon\right)^{-1/2}\left[1+\frac{2}{5}\epsilon\right]^{-5/14}\left[\sqrt{1.2}\sqrt{0.2}\left(8\cdot 1.2^2-2\cdot 1.2-3\right)\right. \\
&\left.\left.\qquad -3\log\left(\sqrt{0.2}+\sqrt{1.2}\right)\right]\right\} \qquad (7.3)
\end{aligned}
$$

The impulse is $3.2{\cdot}10^{-5}$ N·s.

The discharge time is found from Equations 4.47 and 4.48. The discharge time is 0.4 ms.

7.2 Assumptions in Quiescent Environment Study

The analytical and computational study of the SparkJet in a quiescent environment made several assumptions, primarily inviscid flow, no heat conduction and, in the analytical study, that the flow was instantaneously sonic at the throat. These assumptions are evaluated in the following subsections.

7.2.1 Estimation of Effect of Viscosity

The analytical and computational analyses assume inviscid flow. To quantify the effect of viscosity on the dimensionless impulse, the impulse from a computation of the Navier Stokes equations was obtained. For the computation, the dimensionless energy deposition parameter was $\epsilon = 5$ and the dimensionless geometry parameters were that of Table 5.1. The viscosity was computed with Sutherland's viscosity law and the walls of the cavity were assumed adiabatic and no-slip. The Reynolds number based on the cavity diameter and initial conditions in the cavity was $Re_d = \frac{d a_{to} \rho_{to}}{\mu(T_{to})} = 2 \cdot 10^4$. The dimensionless impulse from the viscous computation differs from the analytical impulse by 1.2%. The difference between the dimensionless impulse between the viscous and inviscid cases was 2.5%. The dimensionless impulse from the viscous and inviscid CFD computations differed by less than the computational accuracy, and thus, the viscosity effect on the dimensionless impulse is negligible.

7.2.2 Heat Transfer

The analyses in this paper assume that the walls of the cavity are adiabatic. To estimate the effect of heat transfer through the walls of the cavity a simple analysis is performed using the lumped capacitance model. Assuming that the walls have a uniform heat distribution, the lumped capacitance model for heat transfer can be used to estimate the heat lost to the cavity walls during the time of discharge.

$$Q_{lost} = (m_c c)(T_{to} - T_\infty)(1 - e^{-t_f/\iota}) \tag{7.4}$$

where m_c is the mass of the cavity walls, c is the heat capacity of the wall material, t_f is the discharge time and ι is thermal time constant in the lumped capacitance method, given by the following equation

$$\iota = \frac{m_c c}{h A_s} \tag{7.5}$$

where h is the convective heat coefficient of air, A_s is the surface area of the cavity walls. The ratio of heat lost to the heat added to the system is given by

$$\frac{Q_{lost}}{Q_{added}} = \frac{(m_c c)(T_{to} - T_\infty)(1 - e^{-t_f/\iota})}{\epsilon p_\infty V} \tag{7.6}$$

or, rearranging and using Equation (3.5),

$$\frac{Q_{lost}}{Q_{added}} = \left(\frac{m_c}{\rho_\infty V}\right)\left(\frac{c}{R_{air}}\right)(\gamma - 1)\left[1 - e^{-t_f/\iota}\right] \tag{7.7}$$

Using the dimensional values from subsection 7.1, assuming the cavity is made from stainless steel 304, and the wall thickness is 1/10 of the larger diameter of the cavity, the ratio of heat lost to heat added is 4%. The assumption that the walls are adiabatic should have no significant impact on the impulse results.

7.2.3 Time to Sonic Flow

The analytical model assumes that the throat is immediately sonic. Geometry effects are neglected in this assumption. The computational analysis shows that the SparkJet has an aerodynamic throat above the cavity exit. The dimensionless time for this aerodynamic throat to reach sonic conditions is compared to the dimensionless sonic and total discharge times in the analysis. The dimensionless times for the aerodynamic throat to reach sonic

Case	τ to reach $M = 1$
1	0.004
2	0.016
3	0.002
4	0.014
5	0.006
Dimensionless Duration of Sonic Discharge	0.588
Dimensionless Duration of Discharge	1.878

Table 7.2: Dimensionless Time for Aerodynamic Throat to Reach Sonic Conditions Compared to Total Dimensionless Sonic and Discharge Times

conditions are taken from the first five cases in the Monte Carlo study are shown in Table 7.2. The dimensionless sonic and total discharge times from the analysis are also shown in Table 7.2. The dimensionless time for the aerodynamic throat to become sonic is an order of magnitude shorter than the dimensionless sonic time and two orders of magnitude shorter than the total dimensionless discharge time. Thus, assuming the throat is immediately sonic does not introduce significant error.

7.3 Relevance to Flight Control

The following analysis determines the feasibility of using the SparkJet to control the pitching moment of an aircraft. The following assumptions are made :

1. The surface pressure on the control surface is symmetric except at the SparkJet orifice.
2. The axis of the SparkJet is perpendicular to the moment arm.
3. The flow is inviscid and heat transfer is negligible.
4. The distance from the center of gravity of the aircraft to the SparkJet is much larger than the diameter of the SparkJet.
5. The SparkJet and aerodynamic control surface are compared on the timescale on the order of the SparkJet discharge, *i.e.* for which the force from the full deflection of the flap is unaccounted.

Figure 7.1 shows the spatial relationship between the SparkJet and center of gravity of the flight vehicle.

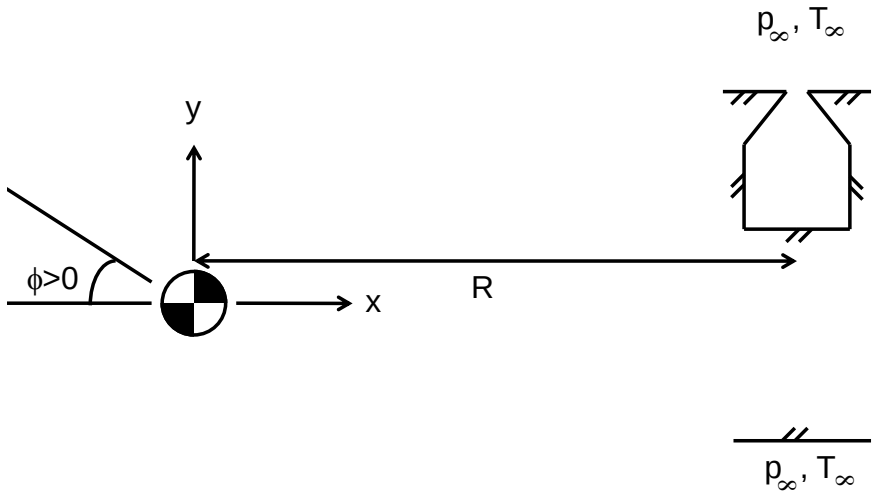

Figure 7.1: SparkJet Relation to Vehicle Center of Gravity

Consider an aerodynamic control surface at the same location as the SparkJet in relation to the vehicle center of gravity, as shown in Figure 7.2.

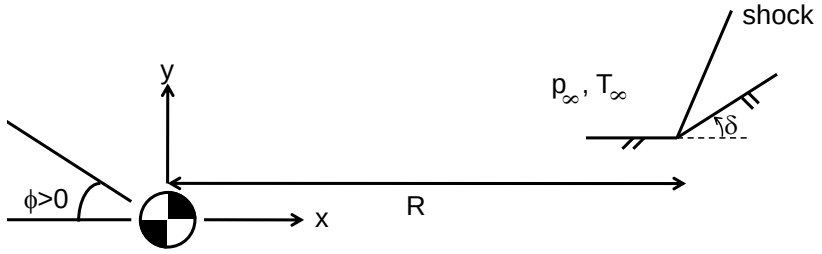

Figure 7.2: Aerodynamic Control Surface Relation to Vehicle Center of Gravity

To determine the efficacy of using an array of SparkJets (SJ) for pitching moment control as compared to an aerodynamic control surface, the effectiveness parameter is defined as the ratio of the pitching rates of each control mechanism, η

$$\eta = \frac{\left.\frac{d\phi}{dt}\right|_{\text{SJ}}}{\left.\frac{d\phi}{dt}\right|_{\text{aero. surface}}} \tag{7.8}$$

7.3.1 SparkJet Rate of Pitch

The rate of pitch from the SparkJet is found by the conservation of angular momentum about the center of gravity of the vehicle center of gravity.

$$M\frac{d^2\phi}{dt^2} = \mathcal{T} \tag{7.9}$$

where M is the moment of inertia about the center of gravity of the vehicle, ϕ is the angle of rotation (shown in Figure 7.1) and $\mathcal{T}$ is torque at the center of gravity.

The instantaneous torque due to the pressure distribution on the control surface is

$$\mathcal{T} = -R\int_{A_i}(p - p_\infty)n_y dA \tag{7.10}$$

where A_i is the interior surface of the cavity excluding the exit area A_e, as shown in Figure 7.3

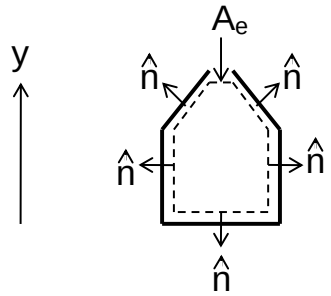

Figure 7.3: Control Volume of SparkJet

The conservation of momentum in the vertical y-direction for the cavity is

$$\frac{\partial}{\partial t}\int_V \rho v dV + \int_A \rho v\vec{v}\cdot\hat{n}dA = -\int_A pn_y dA = -\int_A (p - p_\infty)n_y dA \tag{7.11}$$

where A is the control volume shown by the dashed line in Figure 7.3. Thus,

$$\frac{\partial}{\partial t}\int_V \rho v dV + \int_{A_e}\rho v^2 dA = -\int_{A_i}(p - p_\infty)n_y dA - \int_{A_e}(p - p_\infty)n_y dA \tag{7.12}$$

where $A = A_i + A_e$. It follows that

$$\int_{A_i}(p - p_\infty)n_y dA = -\frac{\partial}{\partial t}\int_V \rho v dV - \int_{A_e}(p - p_\infty + \rho v^2)dA \tag{7.13}$$

and

$$M\frac{d^2\phi}{dt^2} = R\left[\frac{\partial}{\partial t}\int_V \rho v dV + \int_{A_e}(p - p_\infty + \rho v^2)dA\right] \tag{7.14}$$

Integrating from $t = 0$ $\left(\left.\frac{d\phi}{dt}\right|_{t=0} = 0\right)$ to t,

$$\left.\frac{d\phi}{dt}\right|_{\text{SparkJet}} = \frac{R}{M}I \tag{7.15}$$

where I is the dimensional impulse. It is assumed

$$\left.\int_V \rho v dV\right|_t \approx \left.\int_V \rho v dV\right|_{t=0} \tag{7.16}$$

For an array of N SparkJets located approximately at a distance R from the center of gravity,

$$\left.\frac{d\phi}{dt}\right|_{\text{SJ}} = \frac{NR}{M}I \tag{7.17}$$

From the definition of dimensionless impulse and dimensionless energy deposition, Table 3.1, the impulse can be expressed as,

$$I = \frac{p_\infty V}{a_\infty}\sqrt{\gamma\epsilon}\,\vartheta \tag{7.18}$$

Thus, the pitching rate for the SparkJet array is given by

$$\left.\frac{d\phi}{dt}\right|_{\text{SJ}} = \frac{NR}{M}\frac{p_\infty V}{a_\infty}\sqrt{\gamma\epsilon}\,\vartheta \tag{7.19}$$

7.3.2 Aerodynamic Control Surface Rate of Pitch

Consider the deflected aerodynamic control surface shown in Figure 7.2. The conservation of angular momentum is

$$M\frac{d^2\phi}{dt^2} = R(p(t) - p_\infty)A_f \tag{7.20}$$

where A_f is the aerodynamic control flap surface area. It follows that

$$M\frac{d\phi}{dt} = RA_f\int_0^t (p(t) - p_\infty)dt \tag{7.21}$$

Assume the pressure distribution in time on the aerodynamic surface is

$$p(t) - p_\infty = \Delta p \tanh(\zeta t) \tag{7.22}$$

where ζ^{-1} is the characteristic time scale for actuating the control surface and Δp is the maximum pressure rise (when the surface is fully deflected). Then

$$\left.\frac{d\phi}{dt}\right|_{\text{aero. surface}} = \frac{RA_f\Delta p}{M\zeta}\log\cosh\left(\zeta t\right) \tag{7.23}$$

7.3.3 Effectiveness Parameter

The effectiveness parameter, defined by Equation (7.8) becomes

$$\eta = \frac{NI}{\frac{A_f\Delta p}{\zeta}\log\cosh\left(\zeta t\right)} \tag{7.24}$$

Introducing

$$\varpi = \frac{V\zeta}{a_\infty A_e} \tag{7.25}$$

where A_e is the area of the exit of the cavity, the effectiveness parameter becomes

$$\eta = \varpi\frac{A_e}{A_c}\frac{NA_c}{A_f}\sqrt{\gamma\epsilon}\vartheta(\epsilon)\left\{\frac{\Delta p}{p_\infty}\log\left[\cosh\left(\hat{\varpi}\tau_2\right)\right]\right\}^{-1} \tag{7.26}$$

$$\hat{\varpi} = \varpi\left[1+(\gamma-1)\epsilon\right]^{-\frac{1}{2}} \tag{7.27}$$

where A_c is the cross-sectional area of largest part of the cavity. The ratio NA_c/A_f is the packing fraction of the energy deposition synthetic jet array. The maximum value of packing ratio is one for a SparkJet array with an equivalent surface of the aerodynamic control surface. The discharge duration of the jet is given by t_2, from Equation (4.48),

$$t_2 = \frac{V}{a_{t_o}A_e}\tau_2 \quad \text{and} \quad \tau_2 = \left[8.99\left(1+0.4\epsilon\right)^{\frac{1}{7}} - 8.64\right] \tag{7.28}$$

where it has been assumed that $\gamma = 1.4$.

The effectiveness parameter, η versus ambient Mach number and energy deposition ratio, ϵ is shown for a typical SparkJet in Figure 7.4. The effectiveness parameter shown in Figure 7.4 is for a cavity with diameter 5 mm, cavity height 10 mm, exit diameter 1 mm at ambient temperature and pressure, compared to an aerodynamic control surface with a deflection rate of $\zeta^{-1} = 0.1$ sec, $\varpi = 7.2\cdot10^{-3}$ and a packing ratio of 0.9. The effectiveness parameter is of order ten, indicating that the SparkJet achieves ten times the pitching rate of an aerodynamic flap of equivalent surface area at a given time.

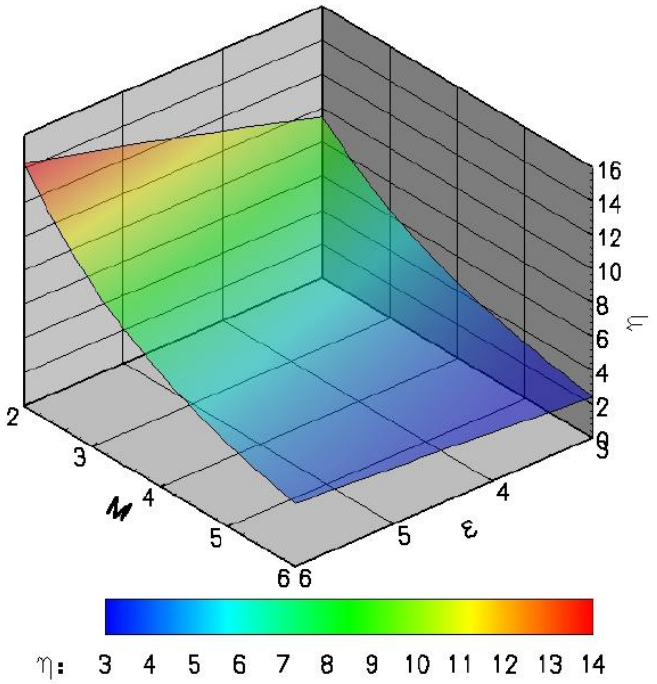

Figure 7.4: Effectiveness Parameter Versus Mach Number and Dimensionless Energy Deposition

7.4 List of Publications

7.4.1 Peer-Reviewed Journal Publications

1. Kellie Anderson, Doyle Knight, "Interaction of Heated Filaments with a Blunt Cylinder In Supersonic Flow," *Shock Waves*, Volume 21, Issue 2, 149-161 (2011).

2. Kellie Anderson, Doyle Knight, "Energy Deposition Induced Synthetic Jet for Flow Control," *AIAA Journal*, publication pending.

7.4.2 Reports

1. Kellie Anderson, Doyle Knight, "Energy Deposition Induced Synthetic Jet for Flow Control," *Center for Computational Design*, CCD Report 2011-02, March 2011.

2. Kellie Anderson, Doyle Knight, "Pendulum Swing from Pulsed Cavity Jet," *Center for Computational Design*, CCD Report 2011-06, April 2011.

3. Kellie Anderson, Doyle Knight, "Response Time for Plasma Jet," *Center for Computational Design*, CCD Report 2011-10, August 2011.

7.4.3 Conference Publications and Presentations

1. Kellie Anderson, Doyle Knight, "Characterization of an Energy Deposition Jet for High Speed Flight Control," 50^{th} *Annual AIAA Aerospace Sciences Meeting*, January 2012, Nashville, TN.

2. Kellie Anderson, Doyle Knight, "Thermal and Aerodynamic Effect of Energy Deposition on Blunt Body in Supersonic Flow," 49^{th} *Annual AIAA Aerospace Sciences Meeting*, January 2011, Orlando, FL.

3. Kellie Anderson, Doyle Knight, "Aerothermodynamic Streamlining of A Blunt Body in Supersonic Flow by Pulsed Energy Deposition," *Thermochemical Processes in Plasma Aerodynamics*, June 2010, Saint Petersburg, Russia.

4. Kellie Anderson, Doyle Knight, "Heat Transfer Effects Due to the Interaction of a Heated Filament with a Blunt Body in Supersonic Flow," 48^{th} *Annual AIAA Aerospace Sciences Meeting*, January 2010, Orlando, FL.

5. Kellie Norton, Doyle Knight, "Thermal Effects of Microwave Energy Deposition in Supersonic Flow," 47^{th} *Annual AIAA Aerospace Sciences Meeting*, January 2009, Orlando, FL.

6. Kellie Norton, Fred Moody, "A Simple Predictive Method of Steam Pipe Forces from Stop Valve Closure," *ASME/JSME Pressure Vessels and Piping Conference*, July 2004, San Diego, CA.

References

[1] Grossman, K., Cybyk, B., Rigling, M., and van Wie, D., "SparkJet Actuators for Flow Control," *AIAA Paper No. 2003-0057*, 2003.

[2] Grossman, K., Cybyk, B., Rigling, M., and van Wie, D., "Characterization of Sparkjet Actuators for Flow Control," *AIAA Paper No. 2004-0089*, 2004.

[3] Cybyk, B., Simon, D., Land, H., Chen, J., and Katz, J., "Experimental Characterization of a Supersonic Flow Control Actuator," *AIAA Paper No. 2006-0478*, 2006.

[4] Haack, S., Taylor, T., Emhoff, J., and Cybyk, B., "Development of an Analytical SparkJet Model," *AIAA Paper No. 2010-4979*, 2010.

[5] Narayanaswamy, V., Shin, J., Clemens, N., and Raja, L., "Investigation of Pulsed-Plasma Jet for Shock / Boundary Layer Control," *AIAA Paper No. 2010-1089*, 2010.

[6] Narayanaswamy, V., Raja, L., and Clemens, T., "Characterization of a High-Frequency Pulsed-Plasma Jet Actuator for Supersonic Flow Control," *AIAA Journal*, Vol. 48, No. 2, 2010, pp. 297–305.

[7] Reedy, T., Kale, N., Dutton, C., and Elliott, G., "Experimental Characterization of a Pulsed Plasma Jet," *AIAA Paper No. 2012-0904*, 2012.

[8] Schierman, J., Ward, D., Monaco, J., and Hull, J., "A Reconfigurable Guidance Approach for Reusable Launch Vehicles," *AIAA Paper No. 2001-4429*, 2001.

[9] Marshall, L., Bahm, C., Corpening, G., and Sherrill, R., "Overview with Results and Lessons Learned of the X-43A Mach 10 Flight," *AIAA Paper No. 2005-3336*, 2005.

[10] Defense Advanced Research Projects Agency, "DARPA Concludes Review of Falcon HTV-2 Flight Anomoly," Press Release, November 2010, *http* : $//www.darpa.mil/NewsEvents/Releases/Releases_2010.aspx$.

[11] Defense Advanced Research Projects Agency, "DARPA Hypersonic Vehicle Advances Technical Knowledge," Press Release, August 2011, *http* : $//www.darpa.mil/NewsEvents/Releases.aspx$.

[12] "Agile Sukhoi Su-27 Leads Strong Soviet Presentation," *Aviation Week and Space Technology*, Vol. 130, No. 25, 1989, pp. 28–30.

[13] Horie, K. and Conway, B., "Optimization for Fighter Aircraft Vertical-Plane Maneuvering Using Poststall Flight," *Journal of Aircraft*, Vol. 37, No. 6, 2000, pp. 1017–1021.

[14] "Failsafe Electrical Mechanical Actuator," Technical specification, Moog Incorporated, 2011.

[15] Schutze, A., Jeong, J., Babayan, S., Park, J., Selwyn, G., and Hicks, R., "The Atmospheric-Pressure Plasma Jet: A Review and Comparison to Other Plasma Sources," *IEEE Transactions on Plasma Science*, Vol. 26, No. 6, 1998, pp. 1685–1694.

[16] Knight, D., Kuchinskiy, V., Kuranov, A., and Sheikin, E., "Survey of Aerodynamic Flow Control at High Speed Using Energy Addition," *AIAA Paper No. 2003-0525*, 2003.

[17] Knight, D., "Survey of Magneto-Gasdynamic Local Flow Control at High Speeds," *AIAA Paper No. 2004-1191*, 2004.

[18] Bletzinger, P., Ganguly, B., Van Wie, D., and Garscadden, A., "Plasmas in High Speed Aerodoynamics," *Journal Physics D: Applied Physics*, Vol. 38, No. 4, 2005, pp. R33–57.

[19] Knight, D., "Survey of Aerodynamic Drag Reduction at High Speed by Energy Deposition," *Journal of Propulsion and Power*, Vol. 24, No. 6, 2008, pp. 1153–1167.

[20] Jayaraman, B. and Shyy, W., "Modeling of Dielectric Barrier Discharge-Induced Fluid Dynamics and Heat Transfer," *Progress in Aerospace Sciences*, Vol. 44, 2008, pp. 139–191.

[21] Kogelschatz, U., "Dielectric-barrier Discharges: Their History, Discharge Physics, and Industrial Applications," *Plasma Chemistry and Plasma Processing*, Vol. 23, No. 1, 2003, pp. 1–46.

[22] Little, J. and Samimy, M., "High-Lift Airfoil Separation with Dielectric Barrier Discharge Plasma Actuation," *AIAA Journal*, Vol. 48, No. 12, 2010, pp. 2884–2898.

[23] Font, G., "Boundary-Layer Control with Atmospheric Plasma Discharges," *AIAA Journal*, Vol. 44, No. 7, 2006, pp. 1572–1578.

[24] Schatzman, D. and Thomas, F., "Turbulent Boundary-Layer Separation Control with Single Dielectric Barrier Discharge Plasma Actuators," *AIAA Journal*, Vol. 48, No. 8, 2010, pp. 1620–1634.

[25] Thomas, F., Kozlov, A., and Corke, T., "Plasma Actuators for Cylinder Flow Control and Noise Reduction," *AIAA Journal*, Vol. 46, No. 8, 2008, pp. 1921–1931.

[26] Kozlov, A. and Thomas, F., "Bluff-Body Flow Control via Two Types of Dielectric Barrier Discharge Plasma Actuation," *AIAA Journal*, Vol. 49, No. 9, 2011, pp. 1919–1931.

[27] Porter, C., Baugh, J., McLaughlin, T., Enloe, C., and Font, G., "Plasma Actuator Force Measurements," *AIAA Journal*, Vol. 45, No. 7, 2007, pp. 1562–1570.

[28] Porter, C., Abbas, A., McLaughlin, T., and Enloe, C., "Spatially Distributed Forcing and Jet Vectoring with a Plasma Actuator," *AIAA Journal*, Vol. 47, No. 6, 2009, pp. 1368–1378.

[29] Zheltovodov, A., Pimonov, E., and Knight, D., "Energy Deposition Influence on Supersonic Flow Over Axisymmetric Bodies," *AIAA Paper No. 2007-1230*, 2007.

[30] Exton, R., Balla, R., Shirinzadeh, B., Brauckmann, G. J., Herring, G. C., Kelliher, W. C., Fugitt, J., Lazard, C. J., and Khodataev, K. V., "On-Board Projection of a Microwave Plasma Upstream of a Mach 6 Bow Shock," *Physics of Plasmas*, Vol. 8, No. 11, 2001, pp. 5013–5017.

[31] Adelgren, R., Elliott, G., Knight, D., Zheltovodov, A., and Beutner, T., "Energy Deposition in Supersonic Flows," *AIAA Paper No. 2001-0885*, 2001.

[32] Zaidi, S. H., Shneider, M. N., and Miles, R. B., "Shock-Wave Mitigation Through Off-Body Pulsed Energy Deposition," *AIAA Journal*, Vol. 42, No. 2, 2004, pp. 326–331.

[33] Kolesnichenko, Y., Khmara, D., Brovkin, V., and Afanas'ev, S., "Optimization of Laser-Pulse Controlled Microwave Energy Deposition," *AIAA Paper No. 1228*, 2007.

[34] Anderson, K. and Knight, D., "Interaction of Heated Filaments with a Blunt Cylinder in Supersonic Flow," *Shock Waves*, Vol. 21, No. 2, 2011, pp. 149–161.

[35] Adelgren, R., Yan, H., Elliott, G., Knight, D., Beutner, T., Zheltovodov, A., Ivanov, M., and Khotyanovsky, D., "Localized Flow Control by Laser Energy Deposition Applied to Edney IV Shock Impingement and Intersecting Shocks," *AIAA Paper No. 2003-0031*, 2003.

[36] Fomin, V., Tretyakov, P., and Taran, J. P., "Flow Control Using Various Plasma and Aerodynamic Approaches," *Aerospace Science and Technology*, Vol. 8, No. 5, 2004, pp. 411–421.

[37] Cambel, A., "Magneto-Gasdynamics: Its Science and Technology," *American Scientist*, Vol. 50, No. 3, 1962, pp. 375–408.

[38] Kalra, C., Shneider, M., and Miles, R., "Numerical Study of Boundary Layer Separation Control Using Magnetogasdynamic Plasma Actuators," *Physics of Fluids*, Vol. 21, No. 10, 2009, pp. 106101–106110.

[39] Park, C., Bodganoff, D., and Mehta, U., "Theoretical Performance of a Magnetohydrodynamic-Bypass Scramjet Engine with Nonequilibrium Ionization," *Journal of Propulsion and Power*, Vol. 19, No. 4, 2003, pp. 529–537.

[40] Macheret, S., Shneider, M., and Miles, R., "Optimum Performance of Electron Beam Driven Magnetodyrodynamic Generators for Scramjet Inlet Control," *AIAA Journal*, Vol. 45, No. 9, 2007, pp. 2157–2163.

[41] Kuranov, A. and Sheikin, E., "Magnetohydrodynamic Control on Hypersonic Aircraft Under "Ajax" Concept," *Journal of Spacecraft and Rockets*, Vol. 40, No. 2, 2003, pp. 174–182.

[42] Shang, J., Surzhikov, S., Kimmel, R., Gaitonde, D., Menart, J., and Hayes, J., "Mechanisms of Plasma Actuators for Hypersonic Flow Control," *Progress in Aerospace Sciences*, Vol. 41, 2005, pp. 642–668.

[43] Caruana, D., Barricau, P., Hardy, P., Cambronne, J., and Belinger, A., "The 'Plasma Synthetic Jet' Actuator. Aero-thermodynamic Characterization and First Flow Control Applications," *AIAA Paper No. 2009-1307*, 2009.

[44] Grossman, K., Cybyk, B., and VanWie, D., *SparkJet Actuator*, US Patent 0021041, February 2004.

[45] Cybyk, B., Grossman, K., Wilkerson, J., Chen, J., and Katz, J., "Single-Pulse Performance of the SparkJet Flow Control Actuator," *AIAA Paper No. 2005-0401*, 2005.

[46] Narayanaswamy, V., Shin, J., Clemens, N., and Raja, L., "Investigation of Plasma-Generated Jets for Supersonic Flow Control," *AIAA Paper No. 2008-0285*, 2008.

[47] Wilcox, D., *Turbulence Modeling for CFD*, DCW Industries, 1993.

[48] Dutton, C. and Coverdill, R., "Experiments to Study the Gaseous Discharge and Filling of Vessels," *International Journal of Engineering*, Vol. 13, No. 2, 1997, pp. 123–134.

[49] ANSYS Inc., *ANSYS CFX Reference Guide*, 2009.

[50] Knight, D., *Elements of Numerical Methods for Compressible Flows*, Cambridge University Press, New York, 2006.

[51] Anderson, W., Thomas, J., and Van Leer, B., "Comparison of Finite Volume Flux Vector Splittings for the Euler Equations," *AIAA Journal*, Vol. 24, No. 9, 1986, pp. 1453–1460.

[52] Favre, A., *The Mechanics of Turbulence*, Gordon and Breach, 1964.

[53] Smits, A. and Dussauge, J., *Turbulent Shear Layers in Supersonic Flow*, Springer Science+Business Media, New York, NY, 1996.

[54] Hopkins, E. and Inouye, M., "An Evaluation of Theories for Predicting Turbulent Skin Friction and Heat Transfer on Flat Plates at Supersonic and Hypersonic Mach Numbers," *AIAA Journal*, Vol. 9, No. 6, 1971, pp. 993–1003.

[55] van Driest, E., "Problem of Aerodynamic Heating," *Aeronautical Engineering Review*, Vol. 15, No. 10, 1956, pp. 26–41.

[56] Hirschel, E., *Basics of Aerothermodynamics*, Springer, New York, 2005.

[57] Dimotakis, P., "The mixing transition in turbulent flows," *Journal of Fluid Mechanics*, Vol. 409, 2000, pp. 69–98.

[58] Gribben, B., Badcock, K., and Richards, B., "Numerical Study of Shock-Reflection Hysteresis in an Underexpanded Jet," *AIAA Journal*, Vol. 38, No. 2, 2000.

[59] Haack, S., Taylor, T., Cybyk, B., Foster, C., and Alvi, F., "Experimental Estimation of SparkJet Efficiency," *AIAA Paper 2011-3997*, 2011.